

Mechanical Investigations: Experimental Fracture Techniques and Frozen Small-Molecule Organics

Thesis by
Bryce Walker Edwards

In Partial Fulfillment of the Requirements for the
Degree of
Doctor of Philosophy

The logo for the California Institute of Technology (Caltech), featuring the word "Caltech" in a bold, orange, sans-serif font.

CALIFORNIA INSTITUTE OF TECHNOLOGY
Pasadena, California

2021
Defended December 17, 2020

© 2021

Bryce Walker Edwards
ORCID: 0000-0002-2393-5488

All rights reserved

ACKNOWLEDGEMENTS

My thinking when coming to Caltech was that the knowledge I would gain could be mostly contained within the umbrella of my eventual thesis title. My quantitative skills only incrementally improved within the areas you will read about in the rest of this document, but my world-view has shifted through my experiences over the last five years.

Writing this dissertation was made possible from the community of people I met during my time here, and what follows is my gratitude.

Foremost, Daryl. Thanks for everything. From introducing me to ultimate frisbee, to bringing your animated joyous presence into many areas of my life here at Caltech, you have always given me useful advice when feeling down. Thank you for being a good teammate, roommate, labmate, and all around one of the best mates I've had.

Amy, thank you for helping me through all the times I was frustrated by the way things were going. Could not have asked for a better quarantine buddy.

Ottman, you're the man! Thank you for your mentorship when I joined the Greer group, and for introducing me to the world of small-scale fracture. It took a while to get back around to it, but much of the compact tension work was driven by what you taught me. Appreciate the way you approach problems, and aspire to one-day match your literature recall ability.

Jane, I hope that your future TEM exploits are of crystals of higher symmetry. Thank you for being a good friend, labmate, RA-mate, and always have confidence in yourself. You are an incredibly talented scientist.

Thank you Carol Garland for showing me how exciting TEM can be and exemplifying the importance of the correlation between time spent with students and their understanding of a subject. You taught me many life lessons between the multitude of TA sessions we shared. I hope that you are enjoying retirement and a renewed German Shepherd companionship.

Thank you to the main players during visiting days that convinced me to come to Caltech. Prof. Brent Fultz for your scholarly approach to every conversation and taking me into your group. Christy Jenstad for your enthusiasm and (over)selling of all the pro's of studying at Caltech compared to any other university (even if I still sometimes daydream about how that might have gone differently). Kelly Mauser

and Andrew Hoff for answering all of my questions during visiting days and helping introduce me to the department once I got here.

Julia, thank you for taking me into your group when I was searching for a new research home at Caltech.

Thank you to the rest of the amazing labmates that I have interacted with over the years. I am sure that I am forgetting a few, but to Widi and Carlos – thank you for the countless hours talking through research plans, offering advice in the office, convincing me to work on lattices, and for help in answering my mechanics questions. Thank you to Ivan and Sophie for working with me in the summer, it is a shame that it went by so quickly, but I enjoyed working with both of y'all.

Thank you to all of my past research advisors. Prof. Juan C. Nino for giving me my first research opportunity and showing how to work in a research environment. Thank you to Chris, Calvin, Robert, Mehrad, Soumitra, and all the other graduate students I got the chance to look up to while at UF. Prof. O. Thompson Mefford for letting me join as a part of your group, and Prof. Susan T. Lepri for letting me join on a project in a totally new field for me.

Thank you to all of the people I have met through the sport of frisbee. You provided me a tether to the world outside of the insular Caltech bubble. This past year has been an interesting one, so also a big thank you to Reason for providing me a place of community when community was hard to find.

Thank you Dad for consistently stressing the importance of schooling while I was growing up. I often think back to these times and do not think that I would have gone to grad school without your push. Thank you Mom for always being there to support whatever, within reason, decisions I make. I love you both and appreciate the guiding principles that have been instilled in me through my upbringing. Also, Lauren, it has been amazing to watch you grow up so much over the last few years. I wished that I did not have to experience this from so far away, but look forward to more sibling time in the coming years.

ABSTRACT

Fracture of architected lattices: Three-dimensional diamond, kagome, and octet lattices were prepared for validation of a standard compact tension fracture experiment at two different length scales. Solid polymer lattices were written via two-photon lithography at the microscale, and solid polymer lattices are printed via digital light processing at the macroscale. Several of the macrolattices were pyrolyzed into carbon lattices to yield a brittle material for testing. The scaling laws of fracture toughness with relative density are explored, and this offers one of the first experimental studies of a fully 3D kagome lattice.

Mechanical properties of solid benzene: We explore the mechanical properties and deformation of 10 μm -sized cuboid-shaped solid benzene crystals made by freezing directly onto a liquid-nitrogen-cooled sample stage and compressed quasi-statically to 10% strain at 125 K with an in-situ nanomechanical instrument inside a Scanning Electron Microscope (SEM). Cryo-Transmission Electron Microscopy (cryo-TEM) and diffraction of frozen benzene confirms the orthorhombic crystal structure of benzene. Compressive contact pressure-strain response generated from load-displacement data suggests the deformation mechanism to occur via densification, with a loading modulus of 9 GPa, slightly larger than that of other small molecules composed of aromatic rings, such as naphthalene and biphenyl. Molecular dynamics (MD) simulations of experimentally equivalent compressions of 10-30 nm benzene samples of the same crystal structure and geometry along the principal lattice directions at 10-30 K suggest densification could, initially, occur by local amorphization of the compressed region. The discovered deformation mechanism, stiffness, and strength of benzene at 125 K can inform our understanding of geological processes on cold planetary bodies. For example, the surface of Saturn's moon Titan is teeming with solid organics at an ambient temperature of 95 K; this work will have significant impact on designing in-situ sampling tools for future missions to Titan and to substantiate speculative surface compositions.

PUBLISHED CONTENT

Chapters 1 and 2 adapted from:

- B. W. Edwards, M. Maurizi, I. Grega, W. P. Moestopo, F. Berto, J. R. Greer, Compact Tension Fracture Specimen for Microarchitected Polymer Lattices, in-preparation.
 - Contributions: Lead this project.

Chapters 3 and 4 adapted from:

- B. W. Edwards, L. Zhong, A. Malyutin, M. J. Malaska, R. Hodyss, H. Gao, J. R. Greer, Deformation and mechanical properties of benzene microcrystals at cryogenic temperatures, in-preparation.
 - Contributions: Lead this project.

Not directly adapted in thesis:

- H. Yang, N. J. Weadock, B. T. Fultz, B. W. Edwards, High capacity corrosion resistant V-based metal hydride electrodes for rechargeable metal hydride batteries (2020), (available at <https://www.osti.gov/biblio/1632593>).
 - Contributions: Design of experimental set-up and data collection.
- National Review of hydrogen storage study. K. E. Hurst, T. Gennett, J. Adams, M. D. Allendorf, R. Balderas-Xicohtécatl, M. Bielewski, B. Edwards, L. Espinal, B. Fultz, M. Hirscher, M. S. L. Hudson, Z. Hulvey, M. Latroche, D. J. Liu, M. Kapelewski, E. Napolitano, Z. T. Perry, J. Purewal, V. Stavila, M. Veenstra, J. L. White, Y. Yuan, H. C. Zhou, C. Zlotea, P. Parilla, An International Laboratory Comparison Study of Volumetric and Gravimetric Hydrogen Adsorption Measurements. *ChemPhysChem* (2019), doi:10.1002/cphc.201900166.
 - Contributions: Sample characterization, data collection and reporting of results to main author.
- A. Vyatskikh, R. C. Ng, B. Edwards, R. M. Briggs, J. R. Greer, Additive Manufacturing of High-Refractive-Index, Nanoarchitected Titanium Dioxide for 3D Dielectric Photonic Crystals. *Nano Lett.* (2020), doi:10.1021/acs.nanolett.0c00454.

- Contributions: TEM sample preparation and analysis, and grain size measurement.
- D. W. Yee, M. L. Lifson, B. W. Edwards, J. R. Greer, Additive Manufacturing of 3D-Architected Multifunctional Metal Oxides. *Adv. Mater.* (2019), doi:10.1002/adma.201901345.
 - Contributions: Data collection and processing.
- O. A. Tertuliano, B. W. Edwards, L. Meza, V. Deshpande, J. R. Greer, Nanofibril-mediated Fracture Resistance of Bone, under review in *Bioinspiration and Biomimetics*.
 - Contributions: Experimental design, data collection, and data analysis.
- C. M. Portela, B. W. Edwards, D. Veysset, Y. Sun, K. Nelson, D. Kochmann, J. R. Greer, Supersonic Impact on Carbon Nano-architected Materials, in-preparation.
 - Contributions: Sample fabrication, data collection and processing.

TABLE OF CONTENTS

Acknowledgements	iii
Abstract	v
Published Content	vii
Table of Contents	viii
List of Illustrations	xi
List of Tables	xv
I Fracture of Microarchitected Lattices	1
Chapter I: Small-scale fracture and architecture	3
1.1 Levels of architecture	3
Natural materials	3
Lattices	4
1.2 Small-scale fracture techniques	6
1.3 Ideation of compact tension lattice specimen	8
Small-scale fracture of homogeneous materials	8
Lattices	11
Mechanical properties of IPDIP	21
1.4 Experimental Methodologies	26
Sample fabrication	26
Chapter II: Compact tension for lattices	35
2.1 Development of the testing method	35
2.2 Compliance correction	36
2.3 Troubleshooting the compact tension specimen for lattices	38
2.4 Parameters studied	40
2.5 Loading data	45
2.6 Crack propagation angle	51
2.7 Crack tip tracking algorithm	53
Loading angle	54
Measures of crack extension	55
2.8 Toughness	58
J-integral	59
2.9 Unresolved observations	60
Broken surface beams	60
Fractography	60
2.10 Conclusion	62

II Compression of Solid Benzene	67
Chapter III: Titan and small-molecule organics	69
3.1 Motivation to study mechanical properties of small-molecule organics	69
3.2 Determining a proxy material system to investigate	71
Chapter IV: Compression of solid benzene	81
4.1 Experimental methodology	81
Sample preparation for micromechanical experiments	81
In-situ compressions	81
Filtering the raw data	85
4.2 Calculating contact pressure	86
Compression onto a cube corner	86
Maximum contact pressure	88
4.3 Calculating yield stress	88
4.4 Results of compression experiments	90
Determining stiffness	91
Elastic recovery	94
Identifying and describing strain bursts	95
4.5 Deformation mechanism	99
4.6 Molecular Dynamic (MD) simulations	99
4.7 Extrapolating to other temperatures	102
4.8 Theoretical mountain height	104
4.9 Transmission Electron Microscopy (TEM)	105
4.10 Conclusions	106
III Concluding Remarks	111
Chapter V: Summary and Outlook	113
5.1 Standardize fracture testing for lattices	113
Alternative testing geometries	113
5.2 Grayscale polymers for rapid prototyping of composites	114
5.3 Cryogenic properties of IPDIP	114
5.4 Mechanical properties of small molecule organics	114

LIST OF ILLUSTRATIONS

<i>Number</i>	<i>Page</i>
1.1 Computer aided drawings (CAD) of the unit cells used throughout this dissertation shown in various renderings.	5
1.2 Brief overview of the process used to study lattices with LIPIT.	7
1.3 Silicon testing fixture with representative samples.	10
1.4 As-printed PR-48 SENB sample.	12
1.5 Pyrolysis temperature profile.	12
1.6 Carbon SENB sample after pyrolysis.	13
1.7 Macroarchitected lattices in a 4-point bend Instron setup before and after failure.	15
1.8 Typical load-displacement signatures from macroarchitected lattices loaded to failure in a 4-point bend Instron test fixture.	16
1.9 Fracture surface of a node in a kagome carbon lattice.	17
1.10 Example frame showing linear fits of the bottom of the lattice as well as the edges of the notch. CTOD and the crack tip are defined by the intersection of these lines.	18
1.11 Printed and etched IPDIP SENB lattice loaded in 3-point flexure.	19
1.12 SEM micrograph of a partially printed IPDIP lattice SENB specimen before and after attempting to increase separation from the substrate by FIB milling.	20
1.13 SEM micrograph of a cylindrical IPDIP pillar.	21
1.14 Compressive stress-strain curves of cylindrical IPDIP pillars of varying laser power.	22
1.15 Plots showing the quasi-static compressive mechanical properties of a series of cylindrical IPDIP pillars printed with varying laser power.	23
1.16 A testing fixture and SENB IPDIP lattice printed together.	24
1.17 Two vertical stitching lines are visible. One is four unit cells to the left of the notch and the other is four unit cells to the right of the notch.	25
1.18 Compact tension lattice sample with shown dimensions and 3 lattice architectures.	27
1.19 Optical image of the inside of the SEMentor chamber.	30

2.1	SEM micrograph showing the indenter tip approaching a silicon chip full of CT samples.	35
2.2	SEM micrographs of loaded specimen used for compliance controls.	36
2.3	(a) Shows a SEM micrograph of fractured top-half specimen used for compliance controls. (b) Shows a load versus displacement curve for each of the two types of compliance control specimen tested. The average loading stiffness is shown.	37
2.4	CAD drawing of the upper loading pin and its head, and the lower loading pin with its base.	39
2.5	Progression of the versions of pin attachment to the CT lattice specimen.	39
2.6	Box-and-whisker plot showing the progression of maximal load and loading stiffness measured for iterations v0 to v2 of the pin attachments. Labeled are the lattice type (kagome is kagome _x of one density, and octet is all of one density), pin version, and the number of experiments (N).	40
2.7	Example of the support beams holding the loading pin to the lattice for a v0.5 type sample.	41
2.8	SEM micrographs of V1 Octet half-CT specimen before and toward the end of loading showing rotation of the sample about the loading pins.	41
2.9	SEM micrograph of a sample printed with insufficient support for the top loading head.	42
2.10	CAD drawings of the 5 different lattice architectures considered.	43
2.11	Parameter space presented. The larger the marker, the more experiments done at those conditions.	44
2.12	Relationship between relative density and slenderness ratio for each of the tested architectures.	44
2.13	Plots showing the relationship between the print-file relative density and the measured relative density. Jitter is added to the print-file RD in part (a) to aid in visualization.	46
2.14	Plots showing the average loading displacement curves for groupings of measured relative density values. The faint lines are individual experiments, the thick line is the average, and the shaded portion is one standard deviation.	47

2.15	Plots showing the average loading displacement curves grouped by print-file relative density. The faint lines are individual experiments, the thick line is the average, and the shaded portion is one standard deviation.	48
2.16	Power-law relationship between the maximum load achieved and the print-file/measured relative density for each of the tested architectures.	48
2.17	Power-law relationship between the loading stiffness and the print-file/measured relative density for each of the tested architectures.	50
2.18	Power-law relationship between the critical stress intensity factor (K_{IC}) and the print-file/measured relative density for each of the tested architectures.	50
2.19	Categorized crack trajectory plotted as a function of relative density and lattice architecture.	52
2.20	Swarmplot of relative density versus lattice architecture showing experiments that did and did not show the formation of a secondary crack.	53
2.21	A representative frame of an in-situ test showing the points of the lattice to be tracked.	54
2.22	Plots showing progression of loading angle throughout two experiments plotted as a function of video frame number.	56
2.23	A representative trend of the unbroken ligament length, crack tip opening displacement, and loading pin separation. These data are from the same experiment as in Figure 2.22a.	57
2.24	A representative frame of the in-situ tests being analyzed to locate the crack tip.	58
2.25	Representative J-curves for each lattice geometry as calculated by Equation 2.8.	59
2.26	Octet sample with visible broken surface beams (circled in orange) after fracture testing.	60
2.27	Plots showing the measured critical stress intensity factor in response to changes in lattice architecture and relative density.	61
2.28	Octet sample with visible broken surface beams (circled in orange) after fracture testing.	62
2.29	SEM micrograph showing the top-half fracture surface of an octet and kagome lattice.	63
3.1	Paraffin wax stuck to two indenter tips.	72

3.2	SEM micrograph of carbon sample loaded under the indenter tip, and the resulting data gathered.	72
3.3	Indentation into water-ice cooled either slowly or quickly.	73
3.4	SEM micrographs showing the surface morphology of IPA, and the issue of dealing with water condensing on these samples.	75
3.5	SEM micrographs showing the relaxation of IPA 0, 1, 2, 6 minutes after pulling the indenter out of contact.	75
3.6	SEM micrograph with an indenter tip compressing the shell of a sublimated piece of naphthalene.	76
3.8	SEM micrographs showing the morphology of frozen benzene.	78
4.1	Images showing the outside and inside of the SEMentor used for these experiments.	82
4.2	Schematic of the chamber during and after sample loading.	83
4.3	SEM micrograph of a typical benzene sample with the indenter tip above.	83
4.4	SEM micrographs of various benzene crystals.	84
4.5	Highlighted (111) plane in a cube. This plane is assumed normal to the direction of indenter loading.	87
4.6	SEM micrographs showing before (left) and after (right) images as a result of the flat-punch compression shown schematically (middle).	90
4.7	Example of typical mechanical signatures observed.	92
4.8	Violin plot showing a comparison of stiffness evolution throughout and between loading and unloading segments.	93
4.9	Violin plots showing the recovery per segment.	95
4.10	Histogram showing distribution of burst sizes.	98
4.11	Scatterplot showing the evolution of stiffness of unbursted benzene.	99
4.12	Comparison between experimental and MD simulated compressions of benzene crystals before and after compression.	100
4.13	Relationships between stress and stiffness with loading direction colored by temperature and particle size represented by data point size.	101
4.14	Relationships between stress and stiffness with loading direction colored by temperature and particle size represented by data point size.	103
4.15	Visualization of the structure of benzene created with Vesta.	106
4.16	TEM micrographs and a diffraction pattern showing the structure of benzene crystals.	107

LIST OF TABLES

<i>Number</i>		<i>Page</i>
2.1	Power-law fit parameters for the relationship between the maximum load and measured relative density.	49
2.2	Power-law fit parameters for the relationship between the loading stiffness and measured relative density.	49
2.3	Power-law fit parameters for the relationship between K_{IC} and measured relative density.	51
2.4	Power-law fit parameters for the relationship between the maximum load and measured relative density.	51
4.1	Parameters used for low-pass Butterworth filtering of noisy data channels.	86
4.2	Summary of results from the three yield stress definitions.	89

Part I

Fracture of Microarchitected Lattices

*Chapter 1***SMALL-SCALE FRACTURE AND ARCHITECTURE****1.1 Levels of architecture****Natural materials**

Environmental forces produce evolutionary changes to living organisms in much the same way that human desire for material progress has led to changes in our built environment. Perhaps the main departure came from the human development of the scientific method [1], which brought about great changes to our world throughout the Age of Reason. This paradigm shift allowed for the explicit discretization of problems into their component parts, which enables rapid progress on larger and more complex projects. The acceleration of technological progress has demonstrated the effectiveness of such methods [2]. Contrarily, evolutionary changes are not based on compartmentalization. These changes are only able to be tested in-vivo and in real time, so cross-correlations are always present.

It seems to me that one could recover the difference between these two manners of conceptualization of a problem and implementation of a solution by focusing solely on the final product. Materials and systems that are engineered by humans tend to be more specialized and perform better at their intended task than those made naturally. However, these same innovations are not nearly as versatile and adaptable to new situations as the naturally derived solutions. For instance, our legs permit us to traverse open land, climb trees, swim in the ocean, etc., while each of these tasks requires a separate innovation. Cars permit us to quickly and effortlessly traverse open land, cranes can transport us to the top of a tree, and boats have allowed humans to spread across the entire globe. Breaking these tasks into independent problems is more resource intensive, but problem specificity leads to efficient optimization of each of those problems that is then limited by the performance of the best material for that specific job, not the performance of a material that requires great multifunctionality.

Historically, the discovery and usage of a new material, like stone to bronze to iron, etc., coincides with a rapid development of tools and technologies, and has been occurring more rapidly. However, as technologies reach the performance limit of all known materials, then an approach other than material discovery and development

must be used. Famous examples such as the impending end of Moore's Law show this shift to alternate improvement methodologies nicely. These shifts to a more systems-centric design space blur the lines between an engineered material and one derived from incremental natural changes.

Ashby plots provide a great tool for the classification of materials, and within that classification there are noticeable trends about the correlations between certain material parameters. Overcoming competition between negatively correlated material properties such as elastic modulus and ductility require the design of new materials that perhaps are composites of different materials that individually perform well along different axes of the design parameter space in which one is concerned. The most pressing correlation to be discussed in this dissertation is that of density with modulus, strength, and toughness. Ashby [3] and others [4] have detailed the benefits of using cellular solids to access the coveted space of low density and high mechanical performance, which noted that many natural materials like trees and bone have already realized the utility of such attributes.

Improving our characterization techniques for experimentally studying architected lattices will enable a new suite of problems that can effectively be discretized. Improvements in additive manufacturing techniques allow the fabrication of lattices that can act as [5] a fertile testing ground for modeling other complex hierarchical systems and making improvements in their own right.

Lattices

Much effort to model these structures has been done in the literature [6]–[8], and for sufficiently low relative densities there are a variety of models that predict the mechanical response satisfactorily. Timoshenko and Euler-Bernoulli beam models are predominately utilized, and both show good agreement with finite element simulations when the relative density is very low. Analytical descriptions of some architectures have been described for a lattice consisting of beams held together by pin joints [7], and again these match modeling efforts at low relative density. This trend suggests that the lattices of higher relative density no longer behave as if the nodes are pin joints. Intuitively, this departure makes sense as the nodes become much thicker, and therefore stiffer, than the beams as the relative density is increased.

Broad differences in the mechanical response of lattice architectures can be describe by the connectivity of their beams. Maxwell offered a rule to determine the rigidity of a structure made out of beams and pin joints [9], which can be written generally

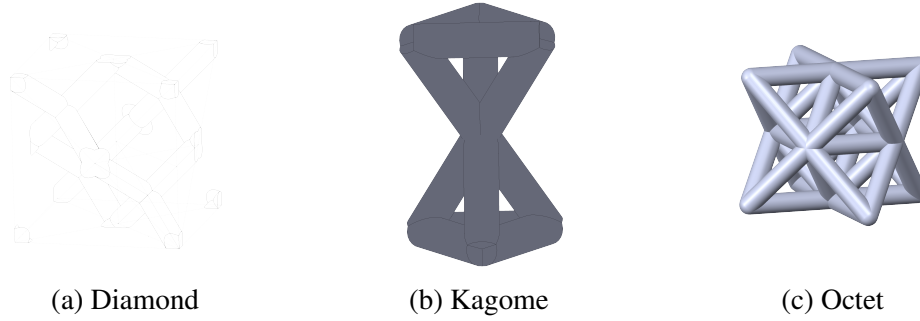


Figure 1.1: Computer aided drawings (CAD) of the unit cells used throughout this dissertation shown in various renderings.

for 3-Dimensions (3D) as [10]:

$$b - 3j + 6 = s - m, \quad (1.1)$$

with b representing the number of beams, j the number of frictionless pin joints, s the number of states of self stress, and m the number of mechanisms of self stress. This necessary, but insufficient rule for determining the rigidity of a given architecture suggests that there might be some transition in behavior across this threshold. Considering the connectivity of a lattice (Z), the number of beams and joints can be related by Equation 1.2.

$$b = j \left(\frac{Z}{2} \right) \quad (1.2)$$

Showing that a 3D lattice with $Z \geq 6$ is periodically rigid, and a lattice with $Z < 6$ is bending-dominated. Interestingly, it seems that in 3D space-filling polyhedra, which are typically used for modeling the behavior of foams, do not form periodically rigid architectures [6].

Using the Maxwell condition, three lattice architectures were chosen for investigation. The diamond ($Z = 4$), kagome ($Z = 6$), and octet ($Z = 12$) architectures are shown below in Figure 1.1. The octet and diamond architectures were chosen to represent the familiar stretching and bending dominated, respectively, cases for lattices. Kagome is of particular interest as both the 2D and 3D lattices are right on the edge of these two regimes. Very little has been done with this architecture in 3D [11], but it has been predicted to have a very high fracture toughness for low relative densities in 2D due to inherent crack blunting mechanisms [12].

Responses to various mechanical stimuli

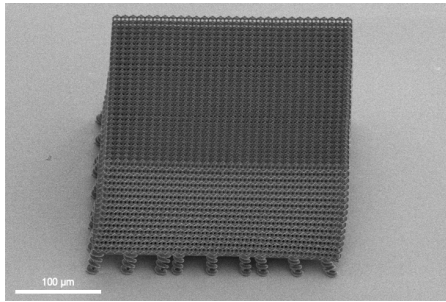
Many mechanical properties are dependent upon the strain rate at which they were measured. Architected materials are no different as has been observed in bone [13], and occupation of the otherwise void-space of the low-density and high-strength Ashby plot makes these lattice materials strong candidates for applications in aerospace. Shielding for satellites and other space vehicles has been considered as these materials provide the opportunity to break up incoming particles, thus redistributing the load imparted by these impacts over a larger surface area. The micrometeorite impacts have been simulated by laser-induced particle impact tests (LIPIT) at the Nelson group in MIT. Large IPDIP (IP-DIP is a proprietary negative-tone resin from Nanoscribe developed for Dip-in Laser Lithography (DiLL).) lattices were made out of 9 piezo-stitched blocks on top of printed springs. These samples were then pyrolyzed, and then we traveled to MIT to impact these lattices with 14- μm silica particles. The springs allow the sample to shrink during the pyrolysis with minimal shear strains coming from attachment to the substrate. Figure 1.2 shows these samples as-printed, impacted, and FIB milled to show the cross-section of the impact site.

Unlike material properties, mathematical models do scale with the size of the system, so the same descriptions used for planetary impacts describe the behavior of these microscopic particle impacts on the lattices. The energy from the impact can be correlated with the zone of accumulated damage observed in the lattice to understand how the lattice responds to this type of mechanical stimulus. A full description of this work is in preparation under the lead of my colleague Prof. C. M. Portela.

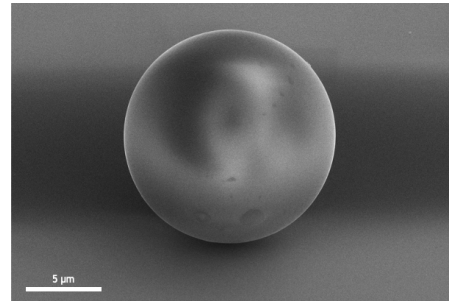
1.2 Small-scale fracture techniques

Experimentally, fracture mechanics is guided by standard testing frameworks to ensure validity and comparability across laboratories and material systems. Many of these standards are kept by ASTM International¹. These standards provide useful values for many situations, but there is always a minimum sample size. With the advent of smaller and smaller technologies, many of the devices that are designed are now requiring feature sizes below these minimum testable sample sizes. It is known that bulk properties do not always scale proportionally with sample size (e.g. "smaller is stronger" [14] and the Hall-Petch relationship [15]).

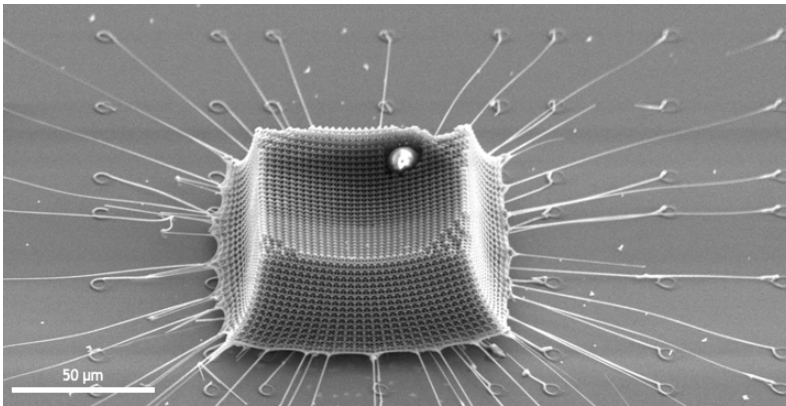
¹ASTM used to be an acronym for American Society for Testing and Materials, but is now an international organization, so that acronym is no longer used.



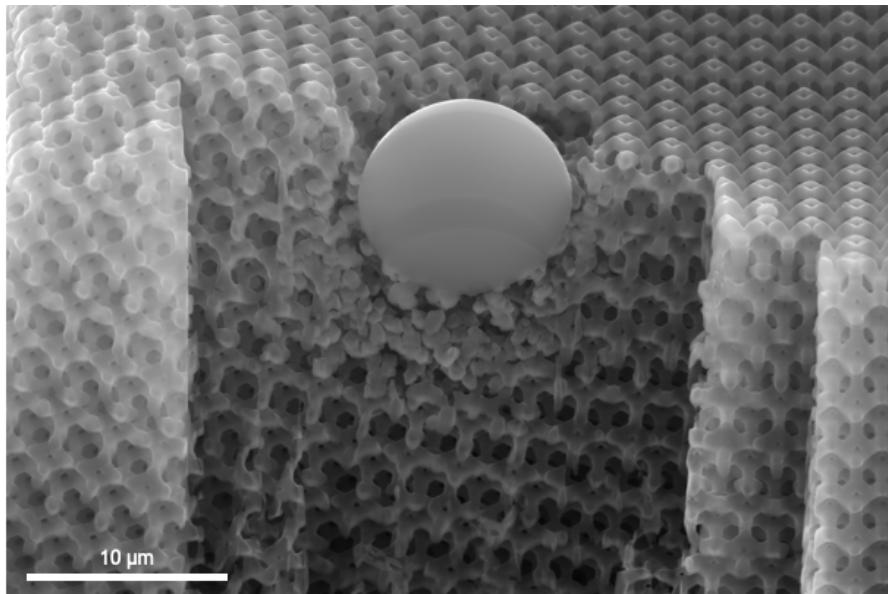
(a) IPDIP tetrakaidecahedron lattice



(b) Silica particle for impact



(c) Pyrolyzed and impacted lattice



(d) Cross-section of impact site and embedded particle

Figure 1.2: Brief overview of the process used to study lattices with LIPIT.

Indentation techniques have been proposed and gained some traction based on their ease of sample preparation and conduction [16], [17], but the accuracy typically reported is very low as it is difficult to ensure that the underlying assumptions are held [18]. Several other methods based on some sort of cantilever geometry have also found widespread use [19]–[22], again due to relative ease of sample preparation, but again there are concerns, albeit smaller, about the validity of such tests. Studying fracture as the size of the samples become on the order of, and smaller than, the plastic zone is difficult as the problem becomes nonlinear. When the samples become so small such that there are only a few thousand atoms in total, then atomistic simulations are able to provide insight to behavior demonstrated experimentally. However, there are not yet well-accepted solutions to characterizing materials in this mesoscale. The need for ever-shrinking devices has pushed many design parameters into this regime, so it is important to characterize materials appropriately. Overcoming the analytical understanding is its own issue, but experimentally the field should be doing everything possible to minimize confounding variables in these new testing configurations. The three-point SENB design (detailed in the following section) is more cumbersome in terms of sample preparation, but it was developed to create a symmetric stress field and allows for the testing of samples produced by a variety of techniques. There could certainly be more work done to enable this technique for lattices, but our motion to an alternative geometry was encouraged by the ease of increasing the separation of scales we can produce with our current laboratory fabrication techniques.

1.3 Ideation of compact tension lattice specimen

Much of the inspiration and guidance for sample geometry came from [23].

Small-scale fracture of homogeneous materials

Part 1 is focused on my efforts to progress the understanding of the fracture behavior of lattices. Chronologically the beginning of my work in the Greer group began with understanding fracture of homogeneous materials in the 3-point bending geometry. This undertaking was done as a proof of concept that an ASTM standard testing procedure could successfully be scaled down to the micron scale. This would both improve upon the various cantilever geometries that dominate the field of small-scale fracture to further the understanding of materials with microstructural features that can only be isolated at these scales.

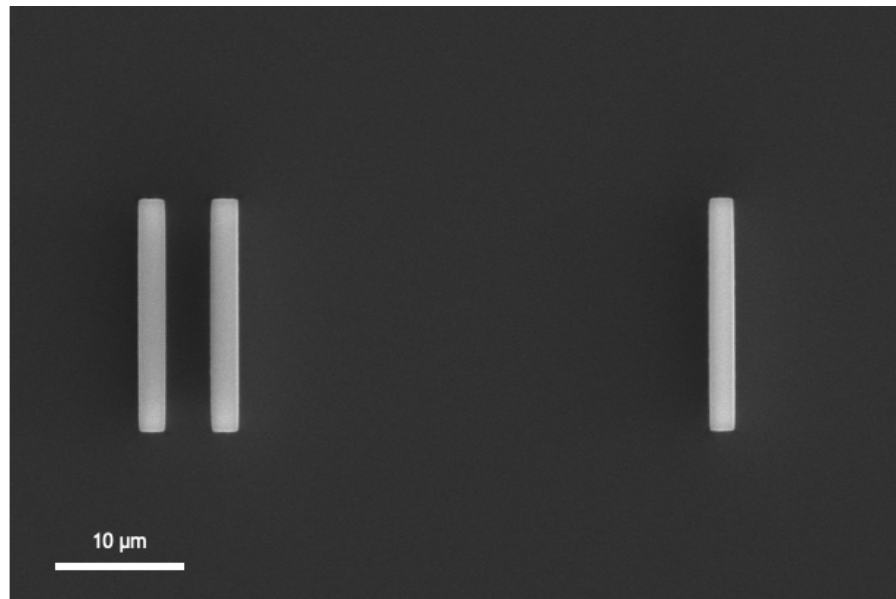
These experiments were done by making a testing stage out of a chip from a silicon

wafer. A mask is patterned onto the silicon chip, as seen in Figure 1.7a, with alumina or IPDIP, and then etched to remove several microns of the unprotected silicon. The masks are then developing away, and the testing fixture is ready for use.

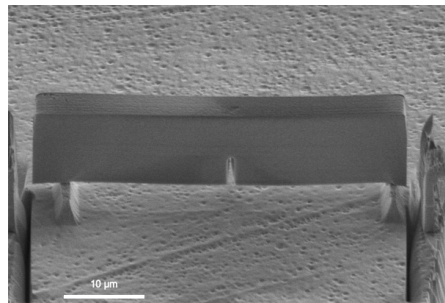
Single-edge notched beams (SENB) specimen of a variety of material classes were then fabricated and placed upon these testing fixtures before loading to failure in an in-situ indenter fixed with a diamond wedge-tip. Silicon beams were used to represent ceramics, and were made by a similar masking and etching process that was used to make the stage followed by a liftout with the assistance of gallium-ion focused ion beam (FIB) milling. Liftout involves placing a sharp tungsten needle onto the surface of the sample to be lifted out, attaching the needle to the sample by deposition of a layer of platinum, milling away the remaining portion of the specimen still connected to the larger bulk sample of material, and then moving the stage of the microscope such that the desired location to set the sample down is now underneath the needle. The sample is then carefully lowered until coming into contact with this new location, in this case the testing fixture in Figure 1.7a consisting of three raised silicon beams, and platinum is deposited on a spot where the sample is contacting the outermost silicon beam. The FIB is then used to mill away the platinum and a portion of the needle until the needle is no longer in contact with the the SENB sample. The needle is then moved to hold the sample down by lightly making contact with the middle of the SENB sample. This is necessary to prevent the movement of the SENB sample while milling away the portion of the sample in contact with, and hosting a shared layer of deposited platinum, with the outermost silicon beam. The FIB is then used to mill away this described region, and the tungsten needle is retracted. Now a SENB sample of arbitrary material that is resting on a testing stage of two silicon beams that will act as the lower loading rollers. The SENB sample is held in place by electrostatic forces that dominate at such length scales, so complications of contact between the SENB sample and testing fixture are minimized.

Fused silica SENB samples were also made as a glassy ceramic representative, and these samples were made by FIB milling and performing liftout from a bulk piece of fused silica.

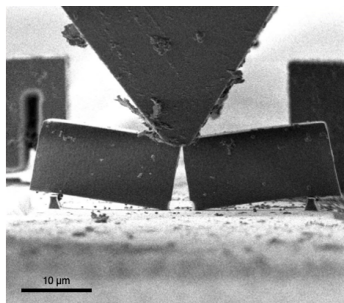
IPDIP beams were used to represent polymer materials, and these were made by writing directly in place by aligning etched silicon testing fixtures as the substrate for writing in the Nanoscribe. Large anchors were printed on either side of the SENB IPDIP specimen to minimize drift in the resin while printing this relatively long



(a) Masked silicon chip



(b) IPDIP SENB specimen



(c) Fractured silicon SENB specimen

Figure 1.3: Silicon testing fixture with representative samples.

overhang. These must be FIB milled away, and the resulting trenches are visible in Figure 1.7b.

Copper SENB specimens were made by electroplating into a mask patterned on a silicon substrate with rectangular holes, developing the mask off of the substrate, and then performing liftout on each sample.

These test materials allowed for the vetting of this experimental process for further understanding of the hierarchical strengthening mechanisms present in human bone. The results of this study lead by Dr. O. A. Tertuliano, which ended up mainly being about bone, are under review for publication in *Bioinspiration and Biomimetics*.

Lattices

Lattices are another interesting material that have much to be studied and characterized in terms of their fracture mechanics, especially experimentally. A constant challenge with these materials is finding a manufacturing technique that permits sufficient separation of scales between minimum feature size and feasible printable volume. The larger this separation, the more unit cells that can be made per feature size of a sample, which allows more flexibility in terms of parameters to be studied. There are many parameters to change in these systems, which allows the mimicry of many other systems such as hierarchical toughening mechanics as seen in natural materials, and microstructural features of crystals [5].

Knowing that material properties are at times dependent upon sample size, we thought that studying lattices of varying dimension would be a good demonstration of the SENB bending technique. Two-photon lithography and digital light processing (DLP) were chosen as manufacturing techniques to produce microscale and macroscale samples of architected lattices.

Macrolattices ²

The larger lattices were produced via DLP in an Ember 3D printer from Autodesk. Their commercial PR-48 resin was used for the polymer samples, and carbon samples were made by pyrolysis of these lattices in a tube furnace from MTI Corporation. The polymers were printed three at a time to 12.5 cm in length (shown in Figure 1.4), the maximal build length. Some of these were pyrolyzed under a vacuum better than 50 mTorr up to 1200°C in an alumina tube for one hour with a ramp rate of 10 per minute and 90 minute holds at 300°C and 500°C. This resulted in a linear shrinkage of around 38%, and a representative resulting carbon sample is visible in Figure 1.6. Each of these types of lattices were loaded to failure using 4-point self-articulating flextural setup in an Instron while being recorded with an optical camera.

²The macrolattice work was done with the help of Sophie Howell, a S.U.R.F. student from Caltech.

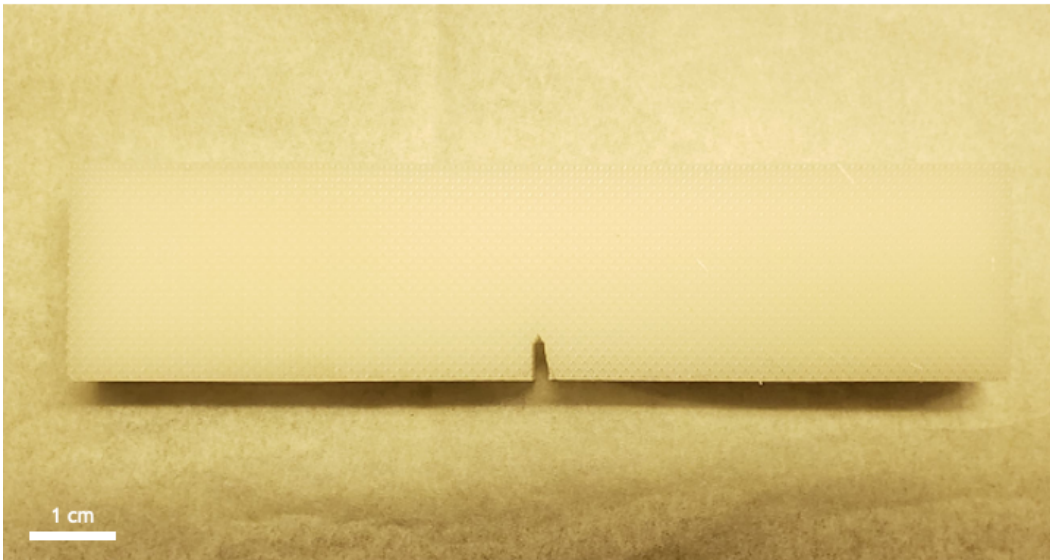


Figure 1.4: As-printed PR-48 SENB sample.

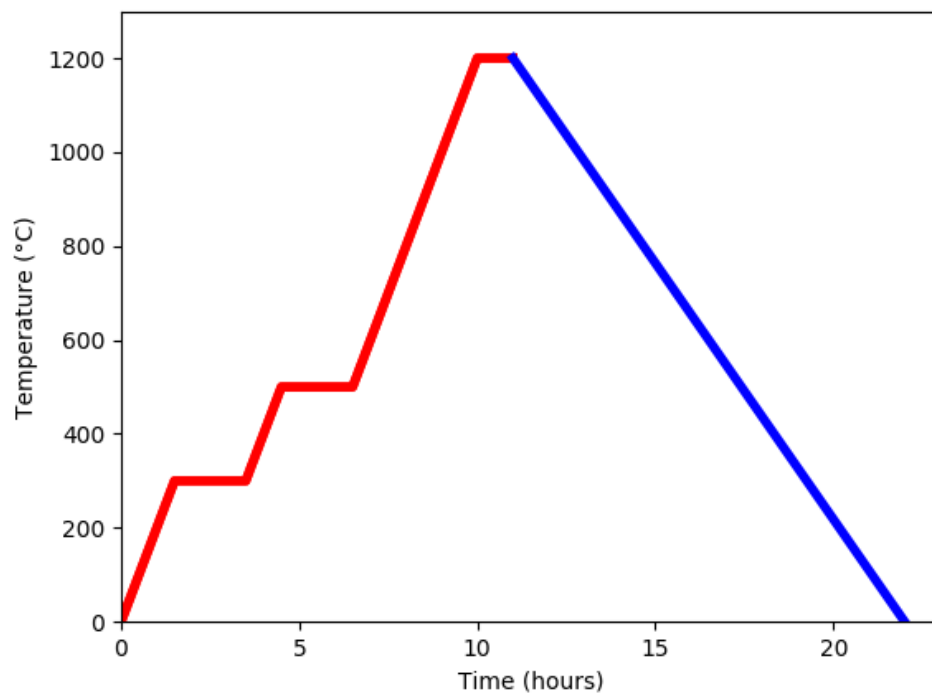


Figure 1.5: Pyrolysis temperature profile.

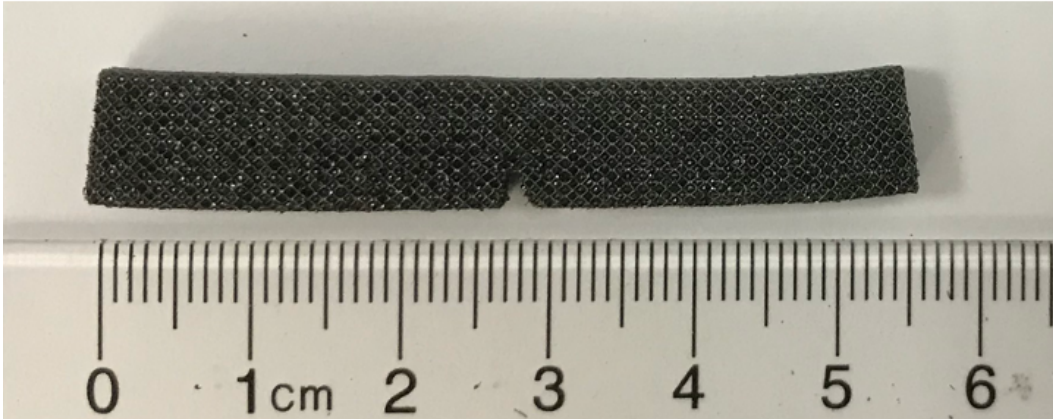


Figure 1.6: Carbon SENB sample after pyrolysis.

The properties of the printed polymer were found to vary within each lattice. The printed window degrades over repeated exposure, and was totally unusable after printing only 3 lattices in one part of the window. This meant that a variable exposure time has to be added in hopes of keeping the polymerization extent consistent throughout one sample, but the degradation also leads to a reduction in lateral resolution, so this is an outstanding problem for this sample fabrication process. A post printing UV-curing was attempted in hopes of equalizing the extent of reaction throughout each sample, but this seemed to have little effect on the final samples.

The notch tends to not be symmetric in these samples as the printing orientation would require a significant overhang to print one side of this notch. The more angled side of the notch comes from the latter half of the sample printed for the octet samples. For the kagome samples, this asymmetry was introduced intentionally along the angle of the beams in hopes of eliminating overhangs entirely. This worked pretty well. There was no observed trend of crack propagation favoring deflection to either side of the lattice, so the impact of these notch shapes is assumed to be negligible.

The pyrolysis proved to be far from consistent. Samples frequently were severely warped after removing from the furnace. Perhaps this warping occurred as a result of some states of self-stress, or a gradient of material properties through the sample due to the changing of light intensity during the printing process. The pressure level

is not monitored throughout each pyrolysis, so a curve of the outgassing is not known. Although, pressure on the order of tens of Torr was observed on multiple occasions during the ramping, and the flow through the tube is not mapped, so perhaps this variability came from atmospheric conditions.

Despite the low processing yield, there were some samples that seemed suitable for bending, so they were quasi-statically loaded to failure. Before and after images of two of these samples are shown in Figure 1.11.

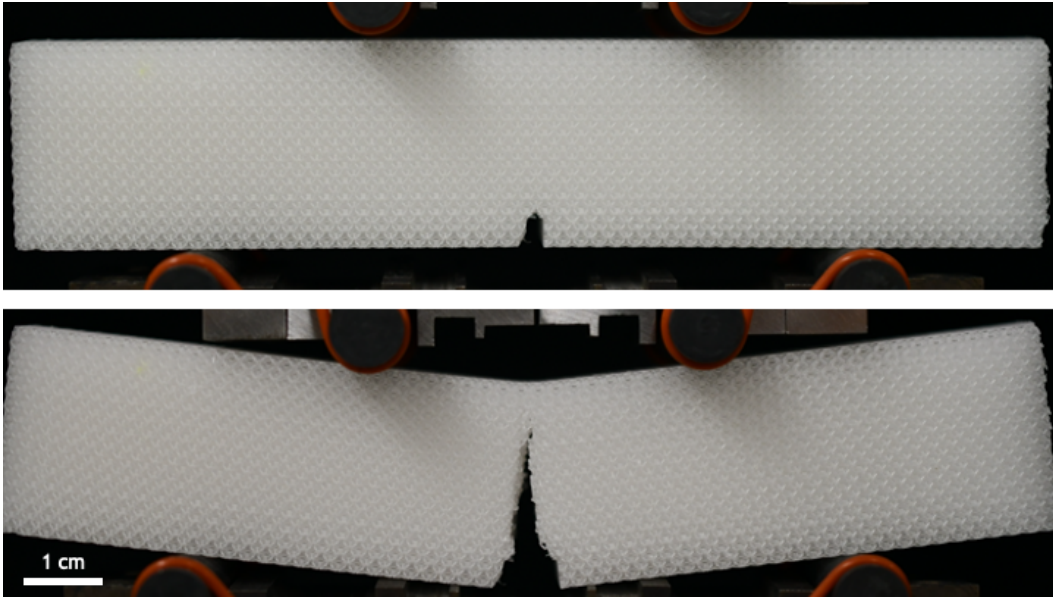
It was found that a 4-point, as opposed to a 3-point, flexural stage was necessary to reduce the contact stresses enough to avoid excessive local failure of the beams at these contact points. The polymer lattices displayed stable crack growth during testing. The carbon lattices let out high-pitched pinging noises and visible debris during their loading. Some of them broke in a catastrophic brittle manner, and some displayed stable crack extension before brittle failure. Shown in Figure 1.8 are characteristic load-displacement signatures of these samples.

The polymer samples displayed a smooth linear loading region up until crack extension and failure. The stiffness was relatively consistent across samples. The loading frame does not have a ton of room for deflection clearance, so the lower relative density samples tended to make contact before failure.

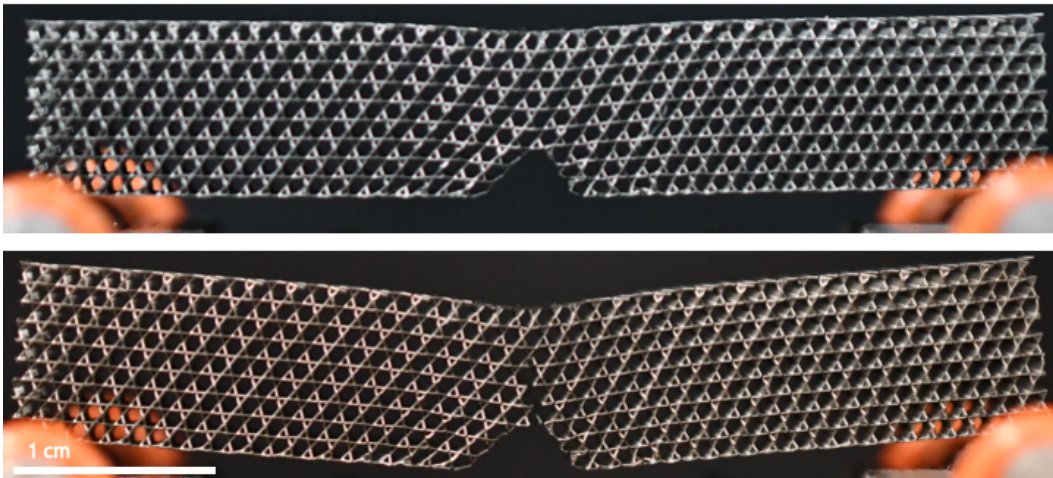
The large toe-region in the carbon data is characteristic of a problem coming from the settling of the samples into the loading pins. These samples are a few millimeters under the required width for this size testing geometry, and the beams are quite brittle, so these factors tended to lead to poor contact at the beginning of loading. The subsequent linear loading region occurs until the first beam failure around the notch tip, and then there were typically a few of these linear regions split between drops in load occurring due to beam failures until the rest of the sample broke in a brittle manner.

Fracture surfaces were inspected with SEM imaging, and some interesting disruptions of brittle fracture were observed within individual beams and nodes of these carbon samples. Figure 1.9 shows the fracture surface of a node right at the crack tip of a kagome lattice. It is hard to draw any conclusions about these data without a clearer picture of the mechanical characteristics of these materials.

Insufficient data was collected for a meaningful analysis of materials tested in this manner. Preliminary results suggest that the critical stress intensity factor for ~15% relative density carbon lattices to be around $411 \text{ kN}\sqrt{m}$ for an octet architecture or

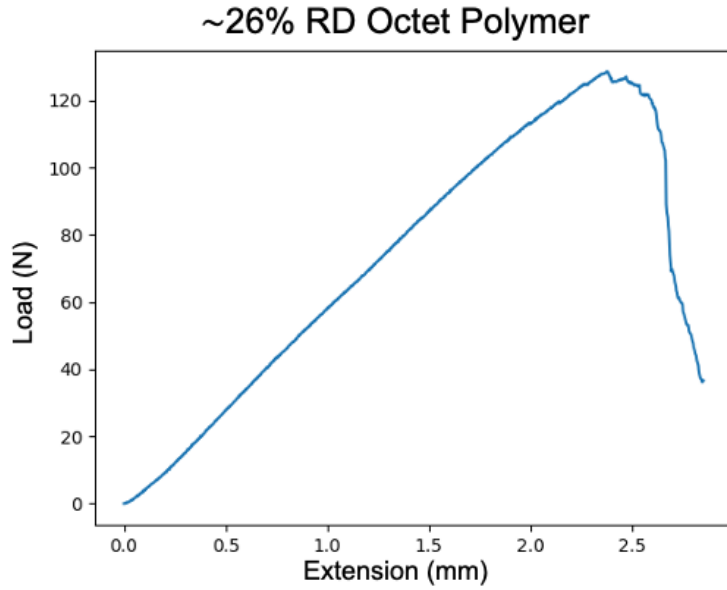


(a) PR-48 SENB specimen.

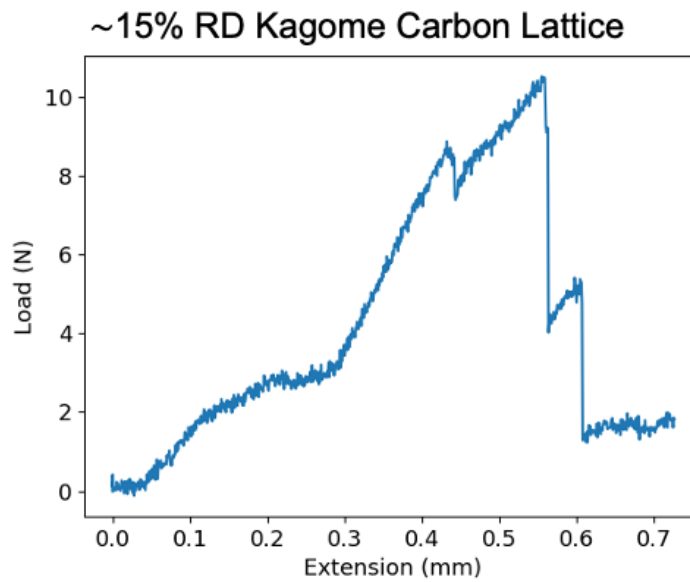


(b) Carbon SENB specimen.

Figure 1.7: Macroarchitected lattices in a 4-point bend Instron setup before and after failure.



(a) PR-48



(b) Carbon

Figure 1.8: Typical load-displacement signatures from macroarchitected lattices loaded to failure in a 4-point bend Instron test fixture.

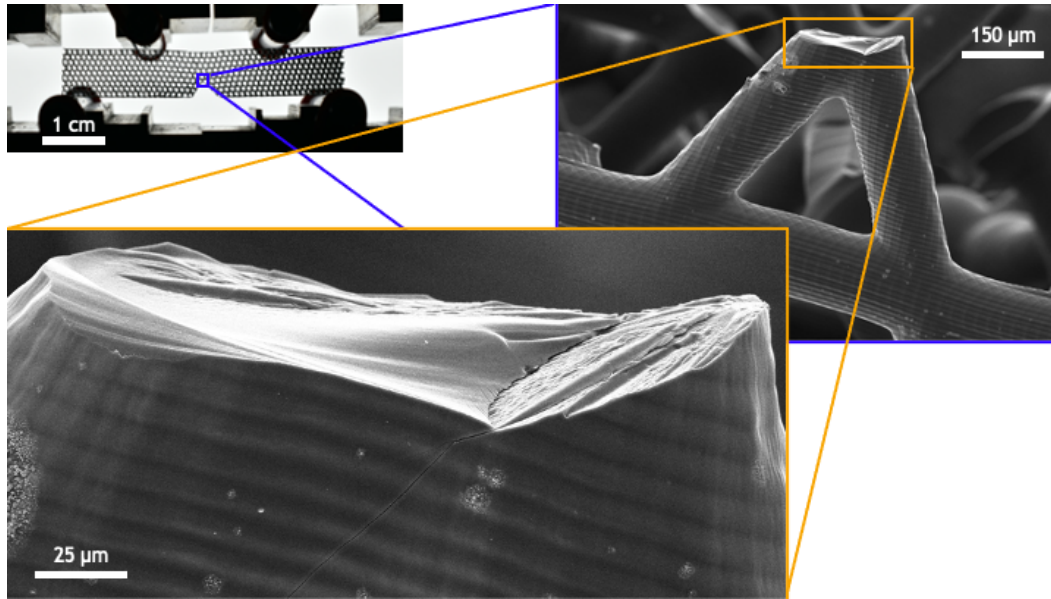


Figure 1.9: Fracture surface of a node in a kagome carbon lattice.

266 $\text{kN}\sqrt{m}$ for a kagome architecture, and around 190 $\text{kN}\sqrt{m}$ for an octet polymer lattice of $\sim 26\%$ relative density or 822 $\text{kN}\sqrt{m}$ for an octet carbon lattice of $\sim 26\%$ relative density.

The imaging algorithm to be used later was first started in an attempt to track the progress of the crack optically. The notch was first found by taking horizontal averages of pixel values and detecting the change at the notch (became brighter for the carbon samples and darker for the polymer samples). This region was then cropped from the image and a standard edge detection package was called upon in Python. The peak of edges detected toward the bottom of the sample was split in half vertically and each side was linearly fit. These linear fits represent the bottom edge of the lattice. The image is then cropped again to focus on just one edge of the notch, and any current crack extension. This cropped portion is converted to grayscale and progressively larger areas of pixel averages are taken to remove focus from any beams dangling within the cracked region. Now, looping across the vertical lines of the image, the lowest point with change from lattice to background brightness intensity is recorded. These points are linearly fit and used as the notch/crack edges. The same is done for the other side of the notch. Now, using these linear fits, the crack tip opening displacement (CTOD) and crack tip are recorded as the intersection of these lines. A samples frame is shown in Figure 1.10. This method seems to work relatively well, but is too manually intensive to be useful for a large number of samples, so improvements are necessary.

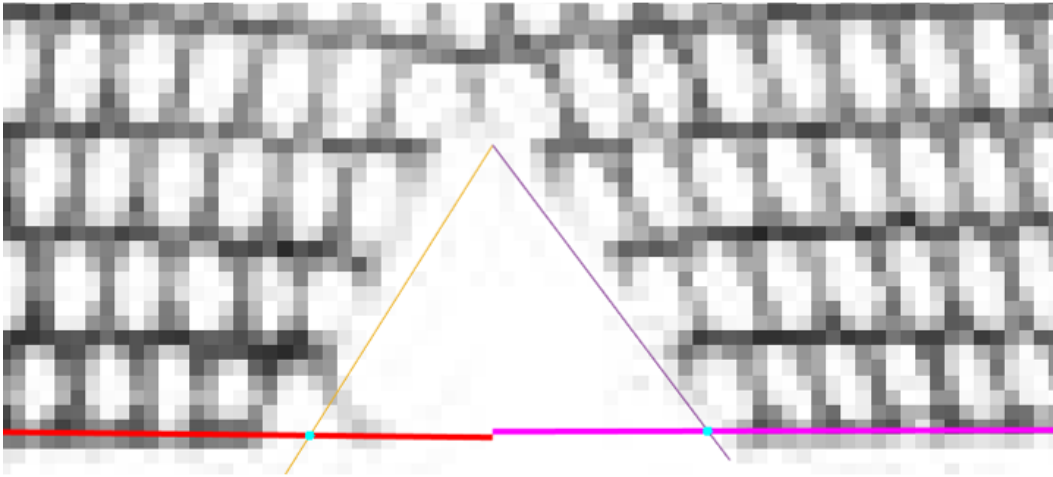


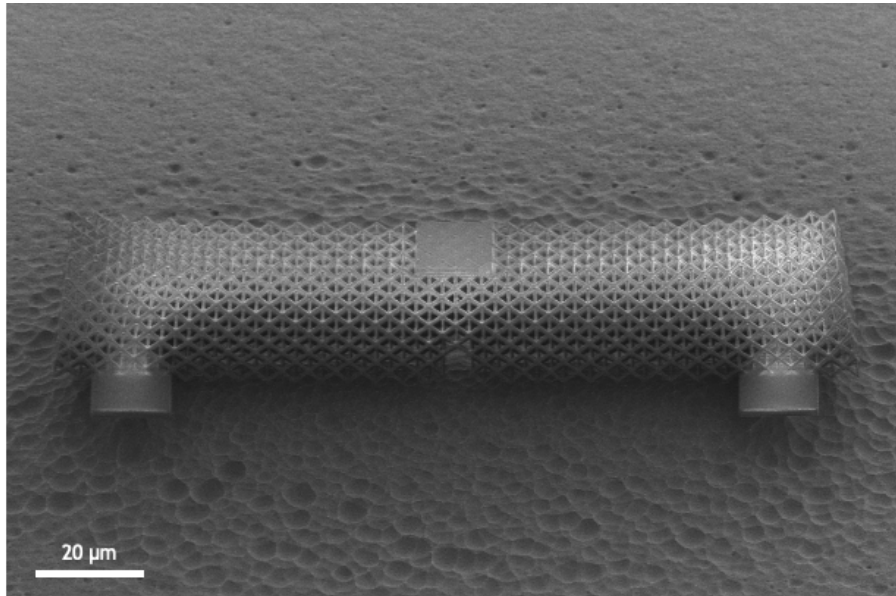
Figure 1.10: Example frame showing linear fits of the bottom of the lattice as well as the edges of the notch. CTOD and the crack tip are defined by the intersection of these lines.

These lattices were just large enough for a valid Charpy impact test, but minimal progress was made in this regard to understand their response to loading at a different strain rate.

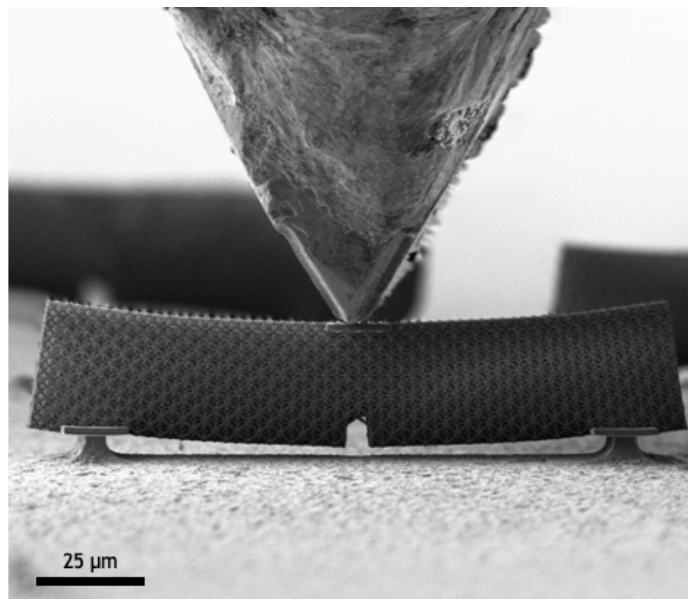
Microlattices

The most natural progression of this work would be to study microlattices via SENB fracture experiments, so this is what was attempted. IPDIP lattice SENB specimens with pads for the lower supports were printed and developed on chips of silicon wafers. These wafers were then etched with xenon difluoride, due to its high selectivity for silicon, to undercut the lattice to provide clearance for flexion, and to undercut the pads until just a thin beam of silicon was left to act as the lower supports. The result of this is shown in Figure 1.11. This process reduces sample preparation to just two steps, which are both automated, so they do not require a large number of working hours as the other techniques that have been explored which involve FIB milling and liftout between separate chips.

The sample fabrication process for these printed and etched SENB experiments is quite rapid with a high throughput, which is desirable for acquiring a high number of experimental data points, as is usually necessary for fracture experiments. However, it proved quite challenging to increase etch depth of the silicon chip without delam-



(a) Printed IPDIP octet lattice on an etched silicon wafer.



(b) In-situ loading for printed SENB lattice.

Figure 1.11: Printed and etched IPDIP SENB lattice loaded in 3-point flexure.

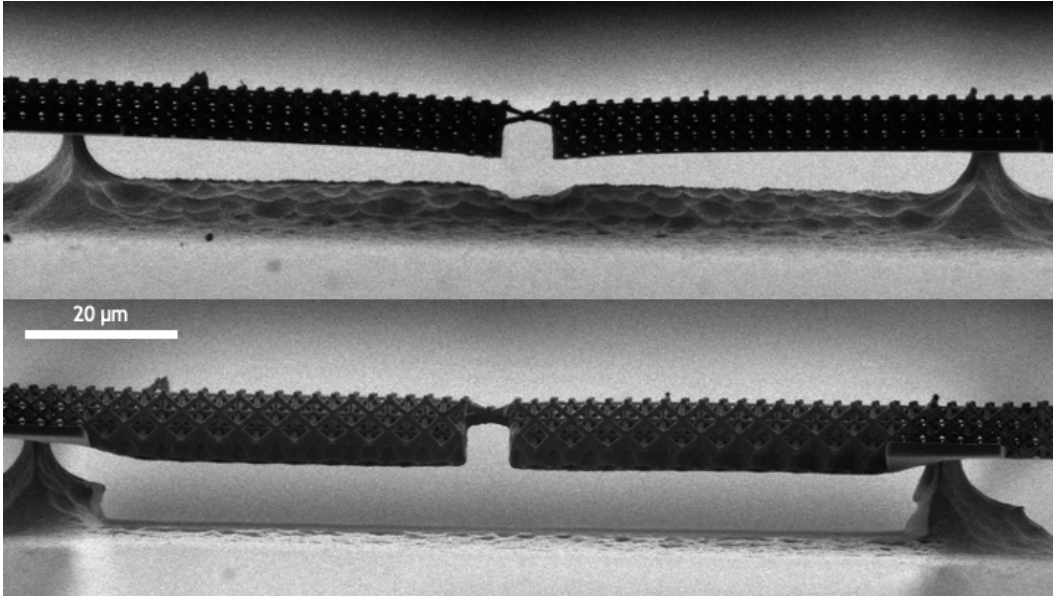


Figure 1.12: SEM micrograph of a partially printed IPDIP lattice SENB specimen before and after attempting to increase separation from the substrate by FIB milling.

ination of the SENB samples. Without taller beams to use as lower test fixtures, the beam makes contact with the substrate before crack extension is observed.

Attempts were made to overcome this issue of insufficient clearance under the SENB specimen by changing etching conditions to make a more directional etch that still had high selectivity for silicon over IPDIP. These two requirements are in conflict with each other and did not provide sufficient improvement to allow the lattice to fully bend and break. Methods to stiffen the SENB specimen were also considered. The addition of a coated material was deemed as adding too many complexities to be studied for the vetting of this new technique for lattices. A post-printed bake has been shown to stiffen similar materials in the literature [24], but only moderate stiffening was achieved, and the lattice still made contact with the substrate before any crack extension was observed.

FIB milling was considered as a workaround for the inability to etch to sufficient depths. Shown in Figure 1.12 is a partially printed SENB lattice that was printed to observe if the lattice thickness had an appreciable impact on the resulting etch depth. It did not produce a terribly different result. As shown in the figure, FIB milling did indeed leave room for further deflection of the beam, but the redeposition of the milled silicon onto the lattice was deemed too significant to continue this method of trench creation.

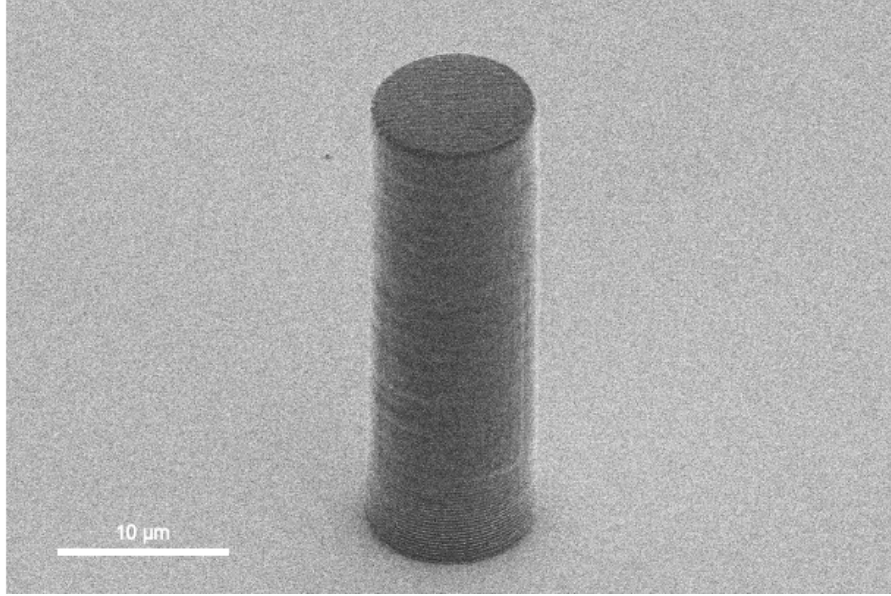


Figure 1.13: SEM micrograph of a cylindrical IPDIP pillar.

Mechanical properties of IPDIP

Properties of a polymer depend on the crosslinking density of a particular sample, and the amount of a resin that has been crosslinked while being produced is commonly referred to as the degree of conversion [25]. The amount of resin reactants that undergo polymerization is dependent on several factors, but mainly the dose of activation energy given during a given manufacturing process. This dose is modulated in two-photon lithography by altering the power of the laser, the speed at which the laser is rastered across the sample, the spacing between rastering layers (slicing), and the spacing between the 3D pixels, known as voxels, that the laser pulses on (hatching) [26]. The laser power that is referred to in this section represents a percentage of the maximal power, 50 mW, achievable with the Nanoscribe.

To characterize the extent to which the degree of conversion alters the properties of IPDIP, cylindrical pillars (diameter = 10 μm , height = 25 μm) were written using the Nanoscribe in a similar fashion as will be employed throughout this dissertation, Figure 1.13.

These pillars were quasi-statically loaded in compression by a diamond flat punch, and the resulting stress-strain response is shown in Figure 1.14.

The IPDIP pillars were loaded to 20% compressive strain before being unloaded and then reloaded again up to 40% compressive strain, as is seen in Figure 1.14. The lowest laser power pillar was loaded to a much higher strain to observe the

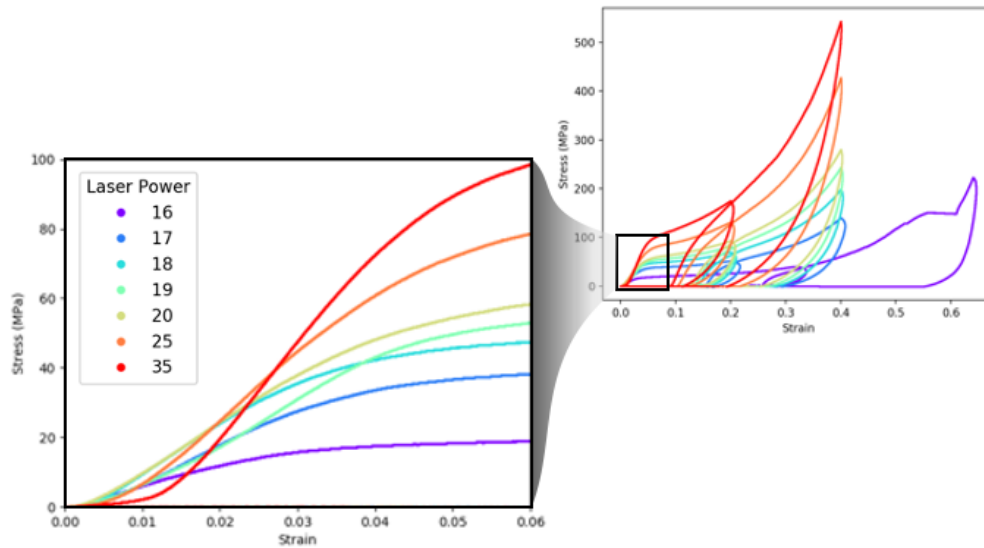
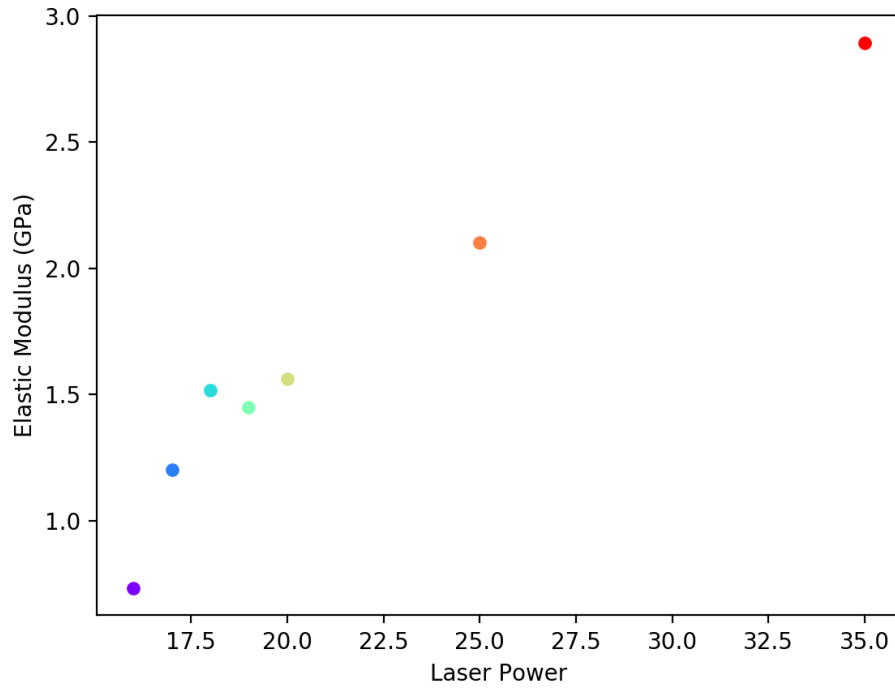


Figure 1.14: Compressive stress-strain curves of cylindrical IPDIP pillars of varying laser power.

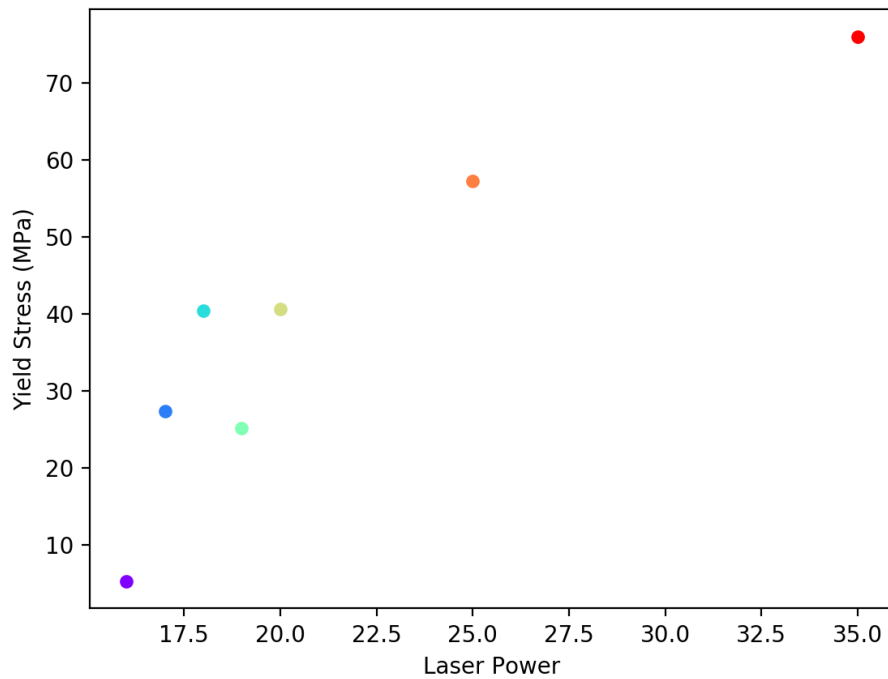
deformation behavior qualitatively. This pillar was observed to barrel and was left with significant plastic deformation once the load was removed. Due to this being a proprietary resin, we do not know all of the components, and the microstructure is not characterized fully, so we cannot describe its behavior fully, but we know that it is essentially some sort of polymethyl methacrylate that has a variety of additives like photoinitiators to enable photopolymerization. So, we expect behavior resembling that of a fairly brittle polymer.

The elastic modulus was found by taking the slope of the steepest part of the first loading region of the stress versus strain plot. The yield stress was then found by using this slope with the 0.2% strain offset method. These parameters are shown, respectively, in Figures 1.15a and 1.15b.

Knowing that an appreciable difference in mechanical properties is achievable based on printing parameters, an alternative method to overcome the issue of insufficient clearance for the SENB lattice specimen was explored. A testing fixture and SENB lattice are written in one step, as shown in Figure 1.16. The fixture is written with a high laser power, and then the lattice is printed at a lower laser power. This allows another benefit of being able to shape the loading fixture more finely since it is produced via additive manufacturing. The lower supports can be made with a varying radius of curvature depending on the geometry and properties of SENB to be printed. This difference in mechanical properties based on degree of conversion



(a) Correlation of elastic modulus with laser power.



(b) Correlation of yield stress with laser power.

Figure 1.15: Plots showing the quasi-static compressive mechanical properties of a series of cylindrical IPDIP pillars printed with varying laser power.

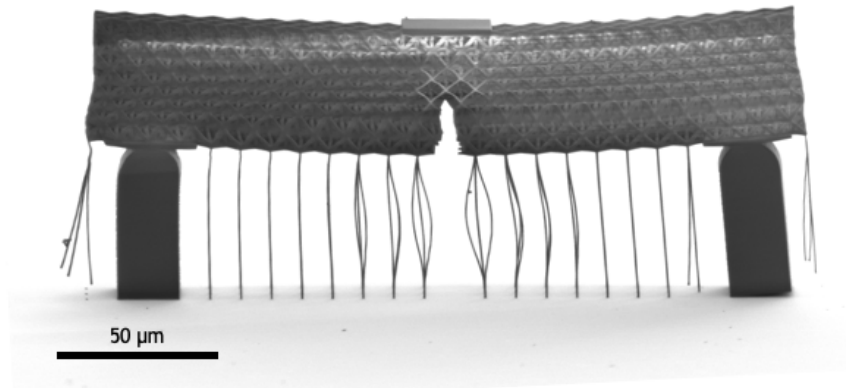


Figure 1.16: A testing fixture and SENB IPDIP lattice printed together.

is much more pronounced for a class of resins known as grayscale polymers, and these are able to be fabricated with moduli that vary by three orders of magnitude [27]. Such drastic separation of properties would make this technique more in line with the standard assumptions.

The supporting beams are necessary to aid in writing the large overhang necessary to make these beams, and there is a balance to be drawn between writing these too thinly such that they are not rigid enough to stand during the writing process to shorten the overhang distance, but not too thick such that FIB milling them away before bending does not take too long, as this is a relatively large footprint area to mill. The pads above the two lower support fixtures and on the top middle act to redistribute the point-loads that are applied from these contact regions. Without them the lattice locally fails at the nodes around these contact regions quite readily.

This setup allowed for crack propagation in these SENB IPDIP specimen, but only small (width = $140\ \mu\text{m}$) beams are able to be produced without stitching. The laser is rastered over the sample in three primary methods of locomotion. The fastest, but smallest range of motion (around $200\ \mu\text{m}$ diameter – for an inscribe square section of around $140\ \mu\text{m}$, and only in the XY plane) is achieved by moving a mirror and is referred to as galvo scan mode. The slowest and largest range of motion (centimeters) is achieved by moving the entire stage with a stepper motor, which has the largest issues of backlash. The third option is to use a piezoelectric

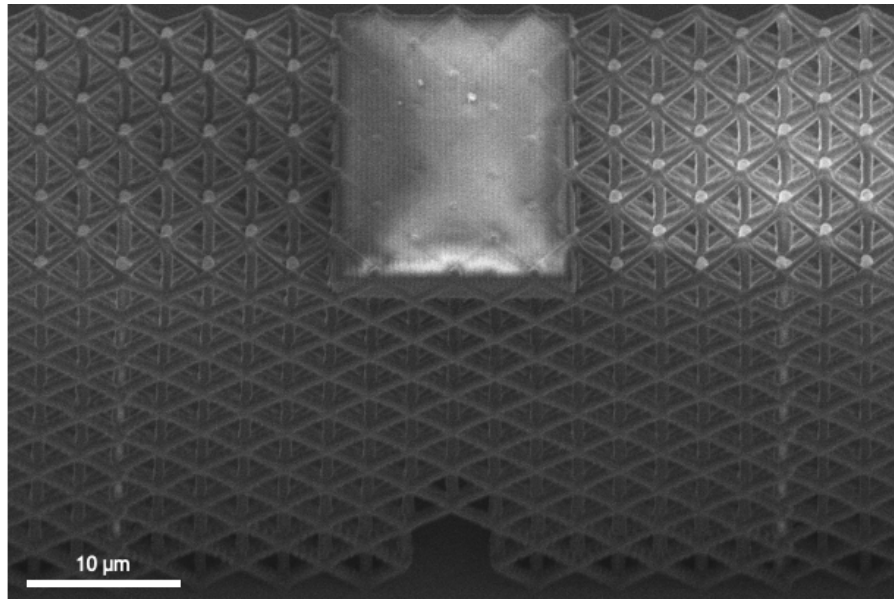


Figure 1.17: Two vertical stitching lines are visible. One is four unit cells to the left of the notch and the other is four unit cells to the right of the notch.

controller, which is between the other in terms of both speed and range ($300\ \mu\text{m}$). Using solely the piezoelectric controller is plausible, but only once all of the design parameters of the testing fixture are resolved as it would produce samples at a rate on the order of one sample per day. Typical samples are made by producing each layer by rastering with the galvo controller, and then using the piezo controller to move between layers. However, if a sample is to be made with lateral features greater than around $140\ \mu\text{m}$, or vertical features greater than $300\ \mu\text{m}$, then stitching is required. Stitching refers to the process by which multiple modes of locomotion are combined for the production of features in a particular direction. Lateral features between $140\ \mu\text{m}$ and $300\ \mu\text{m}$ are made more precisely by scanning over an about $140\text{-}\mu\text{m}$ square section with the galvo section, and then moving with the piezo controller to an adjacent $140\text{-}\mu\text{m}$ square section to write again with the galvo, and features larger than $300\ \mu\text{m}$ go through a similar process with stage motion. The border between each of these galvo sections (can be seen in Figure 1.17) that are stitched together tend to have a higher concentration of defects, which, especially when parallel to the direction of crack propagation, produces a mechanical response that departs significantly from that of the material itself.

So essentially these testing fixtures are maximally-sized constrained by the largest printable feature in a direction consistent with crack propagation.

Being unable to satisfactorily overcome these challenges, and with the desire to

produce the largest separation of scales within a single sample as possible, an alternative geometry was considered as a way to bypass these issues. Also in the ASTM 1820 documentation was a description of a compact specimen [23]. Below, in Figure 1.18, is a geometric description of this specimen. The samples consist of a lattice in the classic compact tension shape, to be tested, supports to hold up the sample to prevent drooping from long overhangs, which have been FIB milled away, and two solid polymer pins held by a base, to attach to the substrate, and to a tensile head, to enable loading. All measurements are governed by the parameter W , which was kept at $100\ \mu\text{m}$ for these experiments. The width, height, and depth of the sample are $1.25W$, $1.2W$, and $0.5W$, respectively. There is a range of options for the initial notch depth (a_0), but $0.4W$ was kept consistent throughout. The sleeve for the pins has an inner diameter of $0.25W$, and the pins have an outer diameter of $0.24W$. The beams are measured for their length (L) and radius for a calculation of the slenderness ratio and actual relative density. There are two parameters listed for the beam diameter, d and D . Due to the shape of the probability distribution of two-photon absorption during printing, the voxel is elliptical. For small beam diameters, it is difficult to arrange voxels such that the resulting beams are cylindrical, which is made worse with larger spacing and hatching distances. Due to this elliptical beam with which the samples are written, the more horizontally oriented beams (D) tend to be thicker than the more vertically oriented beams (d). An average of these two diameter measurements was taken for the relative density and slenderness ratio values presented. It is demonstrated on the diamond inset that the beams for this lattice are of consistent cross-sectional area and shape, which is a consequence of all of these beams being at the same angle relative to the laser during writing.

The following section will outline the sample fabrication required, and the following chapter will discuss the progress made by fracturing lattices in this configuration.

1.4 Experimental Methodologies

Sample fabrication

The first step in making these samples is drawing the desired geometry on a computer-aided drafting software. The samples presented here were designed and drawn in SolidWorks. The part files are then converted to Standard Tessellation Language (STL³) files that can be parsed by DeScribe into layer-by-layer coordinates that a printer is able to read. The samples are then printed from the proprietary "IP-

³Interestingly this is a backronym, the letters STL were assigned to the file type before the words Standard Tessellation (or Triangle) Language.

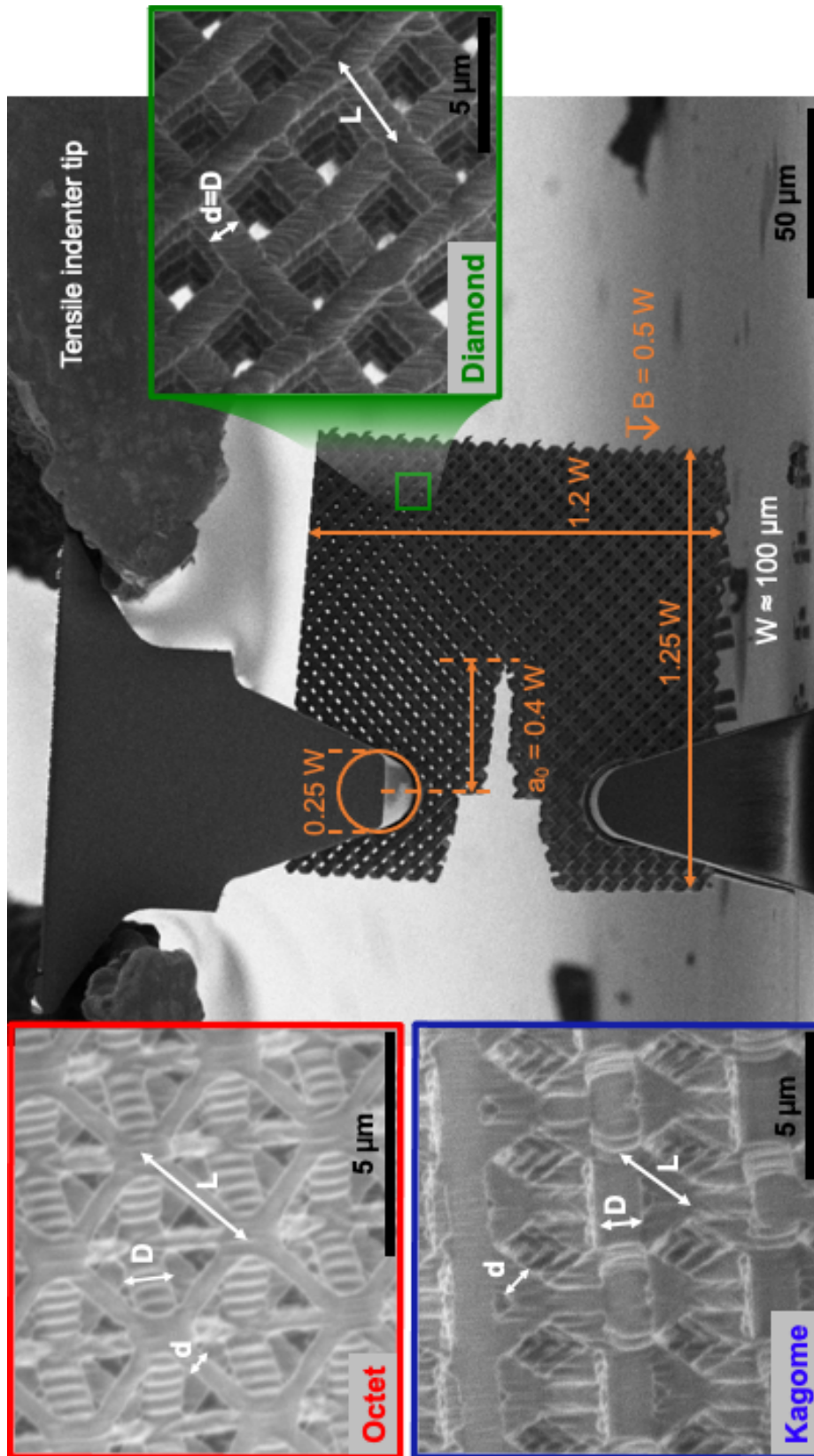


Figure 1.18: Compact tension lattice sample with shown dimensions and 3 lattice architectures.

Dip" photoresist, from Nanoscribe GmbH, via a Dip-in Laser Lithography (DiLL) method of two-photon lithography with a Photonic Professional GT, from Nanoscribe GmbH, 3D printer. The samples are printed with a slicing of 250 nm, hatching of 200 nm, laser scan speed of 20 cm/s, and laser power of 30% (15 mW). These parameters represent a dose lower than that used for the above pillars. The coarsening of the slicing and hatching were necessary to ease the computational burden of handling the massive part, STL, and printer files. This dose produces IPDIP structures with a tensile yield stress (σ_{ys}) of 26.8 MPa, ultimate tensile strength (σ_{ts}) of 84.2 MPa, and elastic modulus (E) of 1.49 GPa, as shown by my colleague W. Moestopo [28].

To improve the adhesion of the printed structure to the substrate used during printing, a necessary step for tensile testing, the pool of resin is placed onto a cut piece of a (100) silicon wafer functionalized with silane that is then loaded into the 3D printer.

The materials required for functionalization are: ethanol, isopropyl alcohol, deionized water, acetic acid, silane (we use 3-(Trimethyloxysilyl) propyl methacrylate), glass vial, glass petri dishes, glass beaker, pipette, syringe, hot plate, sonicator, nitrogen gun, and silicon chips. To functionalize the silicon chips, they are sonicated in isopropyl alcohol for 15 minutes. Preheat a glass petri dish on a hot plate set to 110 . Mix and shake solution A (9.3 mL ethanol, 0.5 mL deionized water, and 0.1 mL acetic acid) in a glass vial. When 5 minutes of sonication are left, add 0.2 mL of silane to solution A and shake well. When sonication is done, pour solution A into a glass petri dish, and pour an excess of ethanol (50 mL) in a separate beaker. Grab silicon chips one at a time and dry with a nitrogen gun before placing into the petri dish filled with solution A. Gently swirl the petri dish for two minutes to ensure proper coverage of the silicon chips. Remove the silicon chips one at a time, in the reverse order in which they were added, and place on the petri dish on the hot plate. After 15 minutes, remove the silicon chips and store for printing.

Once printed, a sample (silicon chip and pool of resin) is developed in 10 mL of propylene glycol methyl ether acetate (PGMEA) for 1 hour to rid the structure of excess monomers, initiator, and any other reactants that were not converted during the photopolymerization printing process. Samples are then transferred into a beaker containing an excess of isopropyl alcohol for 3 minutes to remove a majority of the PGMEA. The sample is then transferred to a beaker containing filtered isopropyl alcohol before being loaded into a Tousimis Autosamdri-931 critical point

dryer (CPD). The CPD is used to dry the sample by heating and pressurizing the surrounding fluid above the critical point in the pressure-temperature phase diagram such that the fluid can be converted from liquid to gas without crossing through the gaseous line. Evaporation stresses are avoided when drying in this manner, which would otherwise warp and pre-stress the sample structures.

The sample is then attached to a SEM stub with colloidal graphite paste. This paste dries into a stiff adhesion layer between the stub and back of the silicon wafer, and we assume the compliance of this layer to have a negligible impact on our tensile experiments.

The support beams of the structure are removed with a focused gallium ion beam (FIB). Samples are loaded into a Versa 3D DualBeam (Thermo Fisher Scientific, formerly FEI Company) SEM and angled such that the gallium ions can pass underneath the architected portion of the sample to give room for milling of the supporting beams.

At this point, a sample is ready to be tensed. A sample is loaded into a Quanta 200 (Thermo Fisher Scientific, formerly FEI Company) SEM that has been custom-built into an in-situ mechanical testing fixture. A silicon chip sample is mounted on an SEM stub with colloidal graphite, and this SEM stub is mounted on a hexagonal block with a set screw. This hexagonal block holds the sample perpendicularly to the XY plane of the sample stage that is moved via screw control. The XY sample stage is 4° off of the plane normal to the direction of the incoming electrons from the SEM column. The indenter tip is mounted in an actuator such that it is perpendicular to the sample, and is digitally controlled by a signal through the wires visible in Figure 4.1b. The Everhart-Thornley Detector (ETD) is biased to attract secondary electrons coming off of the interaction of the electrons from the SEM column with the sample, thus giving an in-situ SEM micrograph to view.

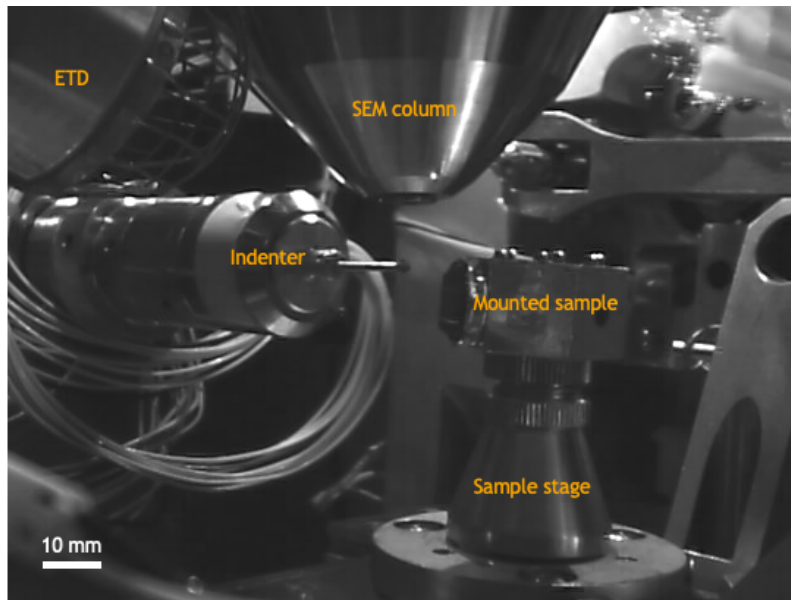


Figure 1.19: Optical image of the inside of the SEMentor chamber.

BIBLIOGRAPHY

- [1] F. Betz, “Origin of Scientific Method,” in *Managing Science. Innovation, Technology, and Knowledge Management*, New York: Springer, 2011, ch. Origin of, pp. 21–41, ISBN: 9781441974884. DOI: 10.1007/978-1-4419-7488-4{_}2.
- [2] M. Buchanan, “Generalizing Moore,” *Nature Physics*, vol. 12, no. 3, p. 200, 2016, ISSN: 17452481. DOI: 10.1038/nphys3685.
- [3] M. F. Ashby, “The mechanical properties of cellular solids,” *Metallurgical Transactions A*, vol. 14, no. 9, pp. 1755–1769, 1983, ISSN: 0360-2133, 1543-1940. DOI: 10.1007/BF02645546. [Online]. Available: <http://link.springer.com/article/10.1007/BF02645546>.
- [4] U. G. K. Wegst, H. Bai, E. Saiz, A. P. Tomsia, and R. O. Ritchie, “Bioinspired structural materials,” *Nature Materials*, vol. 14, no. 1, pp. 23–36, Jan. 2015, ISSN: 1476-1122. DOI: 10.1038/nmat4089. [Online]. Available: <http://www.nature.com/articles/nmat4089>.
- [5] M. S. Pham, C. Liu, I. Todd, and J. Lertthanasarn, “Damage-tolerant architected materials inspired by crystal microstructure,” *Nature*, vol. 565, no. 7739, pp. 305–311, 2019, ISSN: 14764687. DOI: 10.1038/s41586-018-0850-3. [Online]. Available: <http://dx.doi.org/10.1038/s41586-018-0850-3>.
- [6] V. S. Deshpande, M. F. Ashby, and N. A. Fleck, “Foam topology: Bending versus stretching dominated architectures,” *Acta Materialia*, vol. 49, no. 6, pp. 1035–1040, 2001, ISSN: 13596454. DOI: 10.1016/S1359-6454(00)00379-7.
- [7] V. S. Deshpande, N. A. Fleck, and M. F. Ashby, “Effective properties of the octet-truss lattice material,” *Journal of the Mechanics and Physics of Solids*, vol. 49, no. 8, pp. 1747–1769, Aug. 2001, ISSN: 00225096. DOI: 10.1016/S0022-5096(01)00010-2. [Online]. Available: <https://linkinghub.elsevier.com/retrieve/pii/S0022509601000102>.
- [8] H. C. Tankasala, V. S. Deshpande, and N. A. Fleck, “2013 Koiter Medal Paper: Crack-Tip Fields and Toughness of Two-Dimensional Elastoplastic Lattices,” *Journal of Applied Mechanics*, vol. 82, no. 9, p. 091004, 2015, ISSN: 0021-8936. DOI: 10.1115/1.4030666. [Online]. Available: <http://appliedmechanics.asmedigitalcollection.asme.org/article.aspx?doi=10.1115/1.4030666>.
- [9] J. C. F. Maxwell, “On the calculation of the equilibrium and stiffness of frames.,” *Philosophical Magazine Serie 4*, vol. 27, no. 182, pp. 294–299, 1864.

- [10] C. R. Calladine, "Buckminster Fuller's "Tensegrity" structures and Clerk Maxwell's rules for the construction of stiff frames," *International Journal of Solids and Structures*, vol. 14, no. 2, pp. 161–172, 1978, ISSN: 00207683. DOI: 10.1016/0020-7683(78)90052-5.
- [11] J. Wang, A. G. Evans, K. Dharmasena, and H. N. G. Wadley, "On the performance of truss panels with Kagome cores," *International Journal of Solids and Structures*, vol. 40, pp. 6981–6988, 2003. DOI: 10.1016/S0020-7683(03)00349-4. [Online]. Available: www.elsevier.com/locate/ijsolstr.
- [12] N. A. Fleck and X. Qiu, "The damage tolerance of elastic-brittle, two-dimensional isotropic lattices," *Journal of the Mechanics and Physics of Solids*, vol. 55, pp. 562–588, 2007. DOI: 10.1016/j.jmps.2006.08.004. [Online]. Available: www.elsevier.com/locate/jmps.
- [13] U. Hansen, P. Zioupos, R. Simpson, J. D. Currey, and D. Hynd, "The effect of strain rate on the mechanical properties of human cortical bone," *Journal of Biomechanical Engineering*, vol. 130, no. 1, pp. 1–8, 2008, ISSN: 01480731. DOI: 10.1115/1.2838032.
- [14] G. Ouyang, G. Yang, C. Sun, and W. Zhu, "Nanoporous structures; smaller is stronger," *Small*, vol. 4, no. 9, pp. 1359–1362, 2008, ISSN: 16136810. DOI: 10.1002/smll.200800129.
- [15] E. O. Hall, "The deformation and ageing of mild steel: II Characteristics of the Lüders deformation," *Proceedings of the Physical Society. Section B*, vol. 64, no. 9, pp. 742–747, 1951, ISSN: 03701301. DOI: 10.1088/0370-1301/64/9/302.
- [16] F.-C. AC, "A review of analysis methods for submicron indentation testing," *Vacuum*, vol. 58, pp. 569–585, 2000.
- [17] D. B. Marshall, R. F. Cook, N. P. Padture, M. L. Oyen, A. Pajares, J. E. Bradby, I. E. Reimanis, R. Tandon, T. F. Page, G. M. Pharr, and B. R. Lawn, "The Compelling Case for Indentation as a Functional Exploratory and Characterization Tool," *Journal of the American Ceramic Society*, vol. 98, no. 9, pp. 2671–2680, 2015, ISSN: 15512916. DOI: 10.1111/jace.13729.
- [18] J. J. Kruzic, D. K. Kim, K. J. Koester, and R. O. Ritchie, "Indentation techniques for evaluating the fracture toughness of biomaterials and hard tissues," *Journal of the Mechanical Behavior of Biomedical Materials*, vol. 2, no. 4, pp. 384–395, 2009, ISSN: 17516161. DOI: 10.1016/j.jmbbm.2008.10.008. [Online]. Available: <http://dx.doi.org/10.1016/j.jmbbm.2008.10.008>.
- [19] G. Žagar, V. Pejchal, M. G. Mueller, L. Michelet, and A. Mortensen, "Fracture toughness measurement in fused quartz using triangular chevron-notched micro-cantilevers," *Scripta Materialia*, vol. 112, pp. 132–135, 2016, ISSN: 13596462. DOI: 10.1016/j.scriptamat.2015.09.032.

- [20] C. Chen, S. Nagao, K. Suganuma, J. Jiu, T. Sugahara, H. Zhang, T. Iwashige, K. Sugiura, and K. Tsuruta, "Macroscale and microscale fracture toughness of microporous sintered Ag for applications in power electronic devices," 2017. DOI: 10.1016/j.actamat.2017.02.065. [Online]. Available: http://ac.els-cdn.com/S1359645417301660/1-s2.0-S1359645417301660-main.pdf?_tid=b961bd0a-4ba2-11e7-b4e8-00000aab0f26&acdnat=1496854972_ab912298226870af8dfd3511c075c726.
- [21] J. Ast and V. Maier, "Microcantilever bending experiments in NiAl – Evaluation, size effects, and crack tip plasticity," 2014. DOI: 10.1557/jmr.2014.240.
- [22] B. N. Jaya, C. Kirchlechner, and G. Dehm, "Can microscale fracture tests provide reliable fracture toughness values? A case study in silicon," *Journal of Materials Research*, vol. 30, no. 05, pp. 686–698, 2015, ISSN: 0884-2914. DOI: 10.1557/jmr.2015.2. [Online]. Available: http://www.journals.cambridge.org/abstract_S0884291415000023.
- [23] ASTM, "Standard Test Method for Measurement of Fracture Toughness E1820-15a," *ASTM Book of Standards*, vol. N/A, no. 2000, pp. 1–56, 2015. DOI: 10.1520/E1820-15.
- [24] A. Schroer, J. Bauer, R. Schwaiger, and O. Kraft, "Optimizing the mechanical properties of polymer resists for strong and light-weight micro-truss structures," *Extreme Mechanics Letters*, vol. 8, pp. 283–291, 2016, ISSN: 23524316. DOI: 10.1016/j.eml.2016.04.014. [Online]. Available: <http://dx.doi.org/10.1016/j.eml.2016.04.014>.
- [25] S. X. Costa, M. R. Galvão, D. P. Jacomassi, M. I. Bernardi, A. C. Hernandez, A. N. De Souza Rastelli, and M. F. Andrade, "Continuous and gradual photo-activation methods: Influence on degree of conversion and crosslink density of composite resins," *Journal of Thermal Analysis and Calorimetry*, vol. 103, no. 1, pp. 219–227, 2011, ISSN: 13886150. DOI: 10.1007/s10973-010-1018-z.
- [26] J. Bauer, A. Guell Izard, Y. Zhang, T. Baldacchini, and L. Valdevit, "Programmable Mechanical Properties of Two-Photon Polymerized Materials: From Nanowires to Bulk," *Advanced Materials Technologies*, vol. 4, no. 9, pp. 1–11, 2019, ISSN: 2365709X. DOI: 10.1002/admt.201900146.
- [27] X. Kuang, J. Wu, K. Chen, Z. Zhao, Z. Ding, F. Hu, D. Fang, and H. J. Qi, "Grayscale digital light processing 3D printing for highly functionally graded materials," *Science Advances*, vol. 5, no. 5, pp. 1–9, 2019, ISSN: 23752548. DOI: 10.1126/sciadv.aav5790.
- [28] W. P. Moestopo, A. J. Mateos, R. M. Fuller, J. R. Greer, and C. M. Portela, "Pushing and Pulling on Ropes: Hierarchical Woven Materials," *Advanced Science*, vol. 7, no. 20, pp. 1–8, 2020, ISSN: 21983844. DOI: 10.1002/advs.202001271.

*Chapter 2***COMPACT TENSION FOR LATTICES****2.1 Development of the testing method**

My investigation of the fracture properties of lattices is a continuation of work previously started by other students in the research group. A single edge notched beam (SENB) geometry was tested in a 3-point bending configuration (CITE), and a center notch tension (CNT) specimen [1] was studied using similar methods to those used here. The compact tension (CT) geometry was chosen for this study as it allows for the greatest number of unit cells to be printed without any stitching interfaces parallel to the expected direction of crack propagation, potentially leaving a line of defects that would greatly alter sample properties, and the compact tension geometry inherently promotes stable crack growth.

Throughout this chapter we will be working up to the analysis of microarchitected compact tension lattices fractured in an in-situ SEM, as shown in Figure 2.1. A video of a typical experiment is available in the supplementary documents.

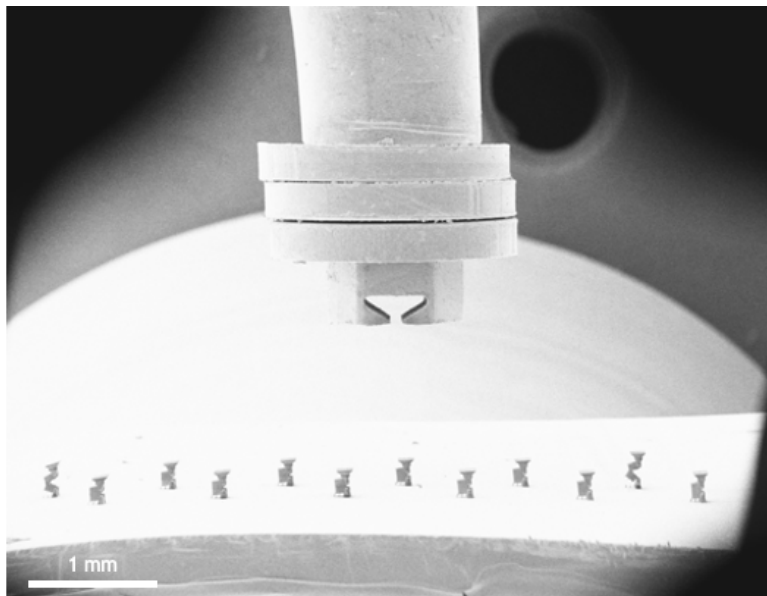


Figure 2.1: SEM micrograph showing the indenter tip approaching a silicon chip full of CT samples.

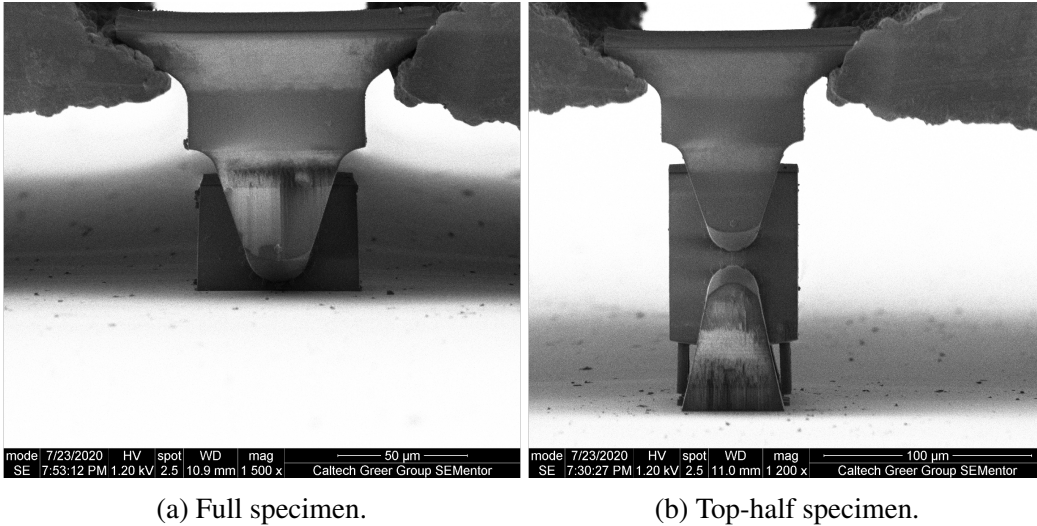
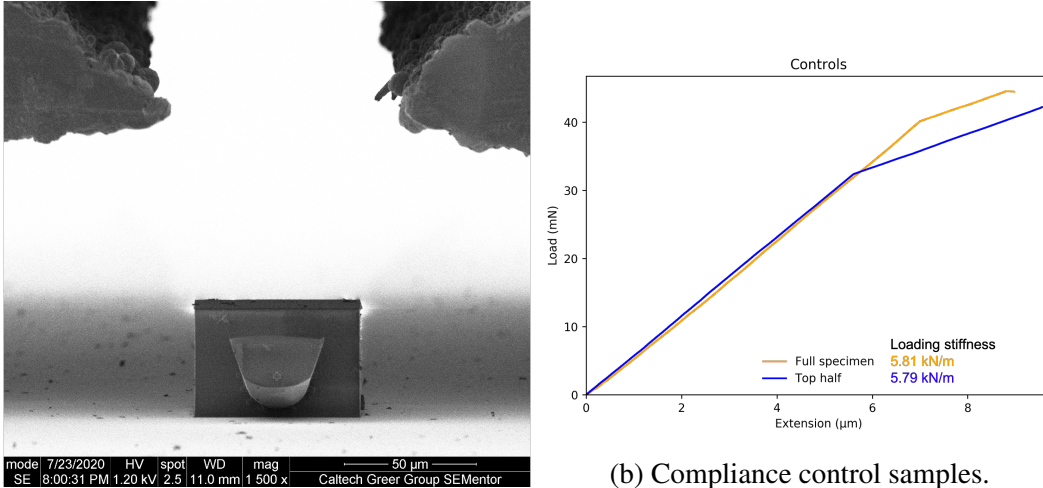


Figure 2.2: SEM micrographs of loaded specimen used for compliance controls.

2.2 Compliance correction

Typically the loading frame is a couple orders of magnitude stiffer than the material to be tested, so the compliance coming from the loading frame can be considered negligible. Since the compliance of the loading pins and material to be tested are printed of the same material, and only different by virtue of their relative density, we cannot make the same assumption and must consider this additional compliance. Essentially the loading frame is now pulling on two springs in series (one being our sample that is tested, and the other being the loading pins and head themselves), and our measured values of load and extension will be the combined signature of these two pieces. Shown in Figure 2.2 are the two specimen geometries that we will consider for making this compliance correction. These specimen are essentially lattices of 100% relative density. These specimen have the same loading pins and attachments (loading head for the top pin and base for the bottom pin) as are used with the lattice samples, but are instead affixed to a solid block of IPDIP of the same dimensions and printing parameters as the lattices.

These specimen were loaded until failure under the same conditions (same indenter and displacement rate) as the rest of the experiments. Figure 2.3 shows the load-displacement response of these specimen and a typical post-fracture micrograph. In all of the control experiments, the loading head was observed to brittlely shear off of the top pin. None of the bases for the bottom loading pin were observed to delaminate from the silicon substrate, thus implying that the surface functionalization is sufficiently strong enough to enable these tensile experiments.



(a) Fractured top-half specimen.

(b) Compliance control samples.

Figure 2.3: (a) Shows a SEM micrograph of fractured top-half specimen used for compliance controls. (b) Shows a load versus displacement curve for each of the two types of compliance control specimen tested. The average loading stiffness is shown.

The load-displacement curves shown in Figure 2.3b are characterized by two linear regimes before failure as shown as a strain burst at the top of the loading curves. There is not a definitive feature from the in-situ videos to explain the sharp transition between the first and subsequently more compliant second loading region. There is slight bending noticeable at the top of the loading head, but it is just my speculation that this is responsible for such a dramatic slope change. However, since this transition was only ever observed at loads around an order of magnitude higher than those experienced during the tensile experiments, it was not seen as a hindrance or point to further investigate in order to carry out the present investigation. Therefore the slope of the initial linear region is used for the compliance correction.

Two of each of these specimen types were tested and showed virtually identical curves, so more experiments were not completed. Interestingly, the stiffness of each of these types of specimen are virtually identical (5.81 kN/m and 5.79 kN/m for the full and top-half specimen respectively). This implies that the bottom loading pin and base are not significant contributors to the compliance response. If introducing the bottom loading pin to the system shows no increase in compliance, then it stands to reason that the top loading pin is not a major contributing factor either, and that the top loading head itself is the source of most of the compliance. Future investigations might find value in attempts to minimize this compliance, perhaps from increasing the footprint of the top of the loading head, but the opportunity

cost of further improvements was not deemed worthwhile for the present study. A majority of the print-time of these samples already comes from making the loading head, and this head is already at the maximum size printable in one viewing window of the 3D printer used. Increasing the size of this head would require stitching via stage motion, which would further increase print time, and increase the possibility of defects.

Once we have this loading stiffness value found above ($K_{correction}$), we will use this to describe the response from everything other than lattice specimen being loaded. The correction to the measured stiffness ($K_{measured}$) of these two parts of the system loaded in series is then made using Equation 2.1 to calculate the stiffness from the sample itself (K_{sample}).

$$\frac{1}{K_{measured}} = \frac{1}{K_{sample}} + \frac{1}{K_{correction}} \quad (2.1)$$

2.3 Troubleshooting the compact tension specimen for lattices

The loading pins and head are printed at the same time as the sample. These loading pins with their fixtures are shown in Figure 2.4. It would be interesting to utilize another resin with a wider mechanical property space based on printing parameters to make these pins much stiffer than the material being tested. I wrote a script to make samples in this manner in the NanoScribe, but have not printed enough to comment on how much this would improve the current loading fixture.

The interface of the pins with the lattice itself proved to be quite troublesome. When rigidly integrated as being fixed directly onto the lattice, these pins caused much torque in the surrounding unit cells, which could not be properly accounted for in the analysis. A progression of alternative designs were considered and are shown in Figure 2.5.

Sleeves were added in the sample around the loading pins to overcome any stress concentrations causing local beam failure. A similar approach proved useful for testing the fracture of macro-scale metallic lattices manufactured with selective laser melting [2]. Nearly an order of magnitude reduction in both maximum load and loading stiffness was observed upon switching from V0 to V3 connections of the pin to the lattice. These small support beams for the pin typically break and allow, relatively, free rotation of the pin within the sleeve. There is still some friction that we are unable to account for in the analysis, but this has been greatly reduced, and is assumed to be negligible. Small beams fixing the pin to the lattice for a V0.5 type

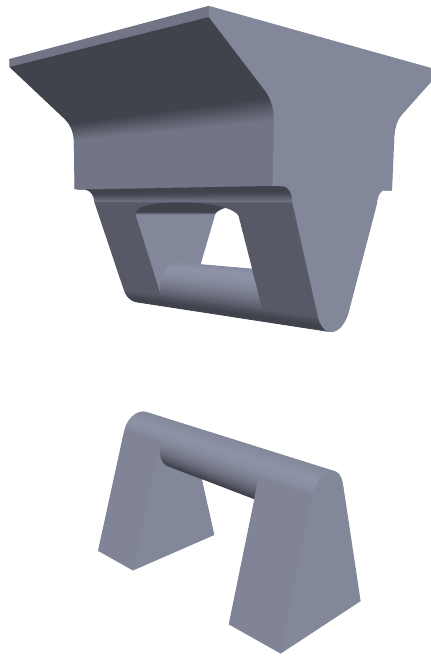


Figure 2.4: CAD drawing of the upper loading pin and its head, and the lower loading pin with its base.

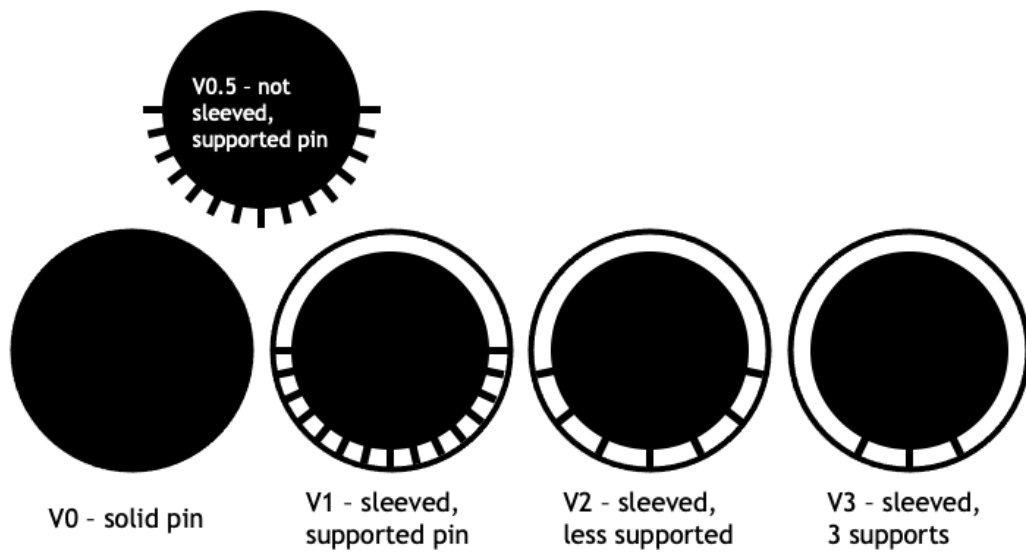


Figure 2.5: Progression of the versions of pin attachment to the CT lattice specimen.

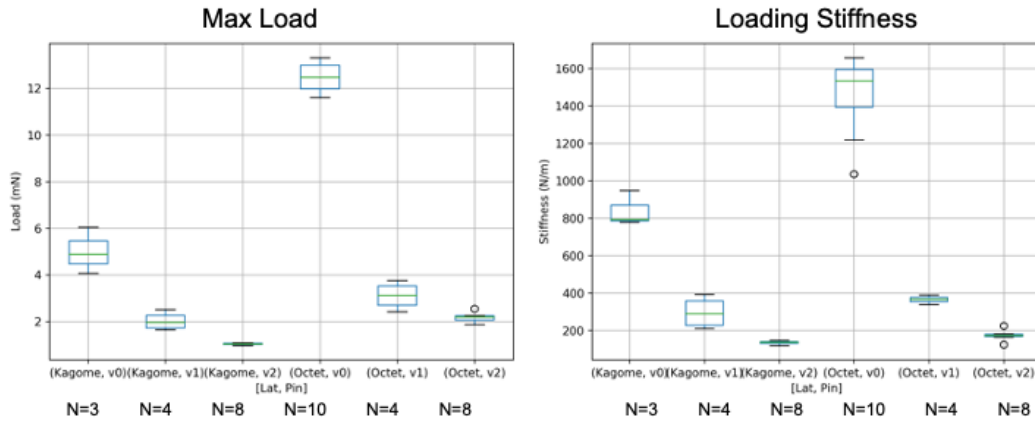


Figure 2.6: Box-and-whisker plot showing the progression of maximal load and loading stiffness measured for iterations v0 to v2 of the pin attachments. Labeled are the lattice type (kagome is kagome_x of one density, and octet is all of one density), pin version, and the number of experiments (N).

sample are visible in Figure 2.7. The reduction in maximum load and the loading stiffness for progression from v0 to v2 sleeves is shown in Figure 2.6. A relatively small decrease was observed from moving from v2 to v3, and the rest of the results presented are on lattices tested with v3 sleeves.

Half samples were made by writing half samples (cut in half with a slice parallel to the substrate) to observe the behavior of these supporting pin beams within the sleeve. A V1 type sample is shown in Figure 2.8.

For full samples, it was observed that this number of support beams for the pin did not always break upon loading, especially for the lower relative density samples, so pins were progressively removed until the loading head for the top pin is no longer sufficiently supported. As shown in Figure 2.9, this is the result of too weak of pin supports, leaving a sample that is not testable as the top loading head is inaccessible to the indenter tip.

2.4 Parameters studied

CAD drawings of the lattice architectures tested are shown in Figures 1.1 and 2.10.

The lattice architecture and relative density were the main variables altered during these experiments, and the explored parameter space can be visualized in Figure

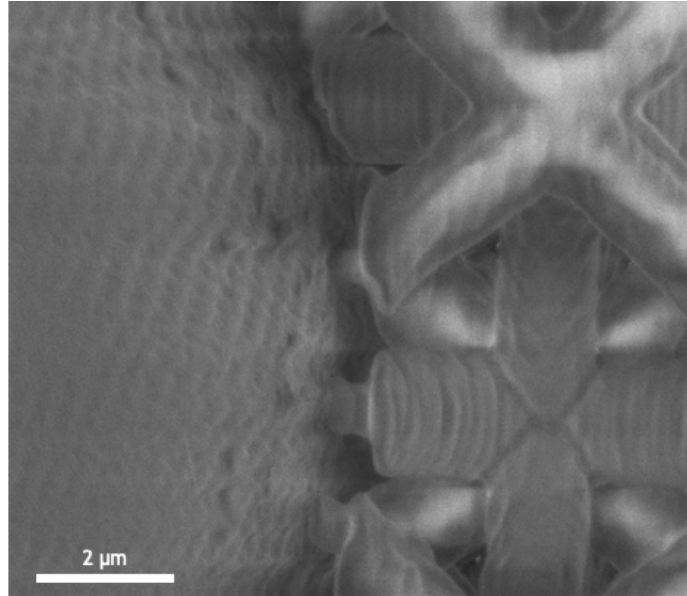
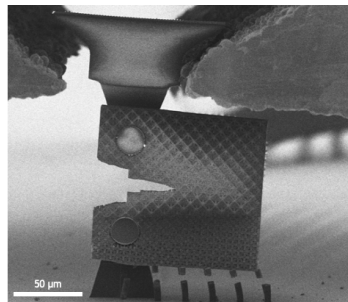
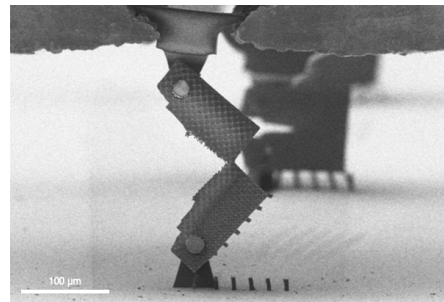


Figure 2.7: Example of the support beams holding the loading pin to the lattice for a v0.5 type sample.



(a) V1 Octet half-CT specimen



(b) Loaded V1 Octet half-CT specimen

Figure 2.8: SEM micrographs of V1 Octet half-CT specimen before and toward the end of loading showing rotation of the sample about the loading pins.

2.11. Much of the computational literature on lattices focuses on very low relative density, as these materials are more well characterized as a collections of beams and pin joints, but at higher relative densities the geometry and volume of the nodes starts to have a strong impact on the behavior of the lattice as a whole [1], [3]. The stretching-dominant octet unit cells were constrained to being printed at higher relative densities in order to avoid deterioration of the print quality of the sample, especially around the notch. Samples of too low relative density are unable to support the tension head, and tend to have a less pronounced notch as the overhanging features are not printed as well. This can be seen as a result of too low of a beam slenderness ratio, as shown in Figure 2.12. The relative density of an

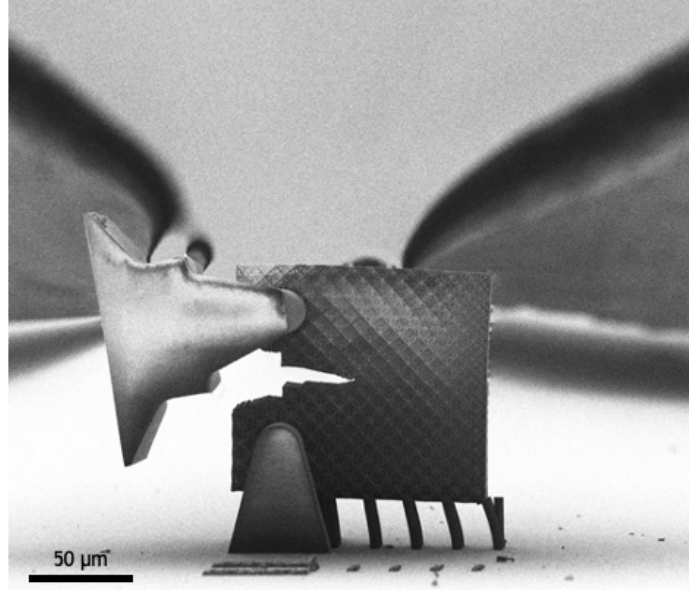


Figure 2.9: SEM micrograph of a sample printed with insufficient support for the top loading head.

octet unit cell has a much higher dependence on slenderness ratio, which explains its larger minimum printable relative density. The bending-dominant diamond unit cell is on the opposite side of this issue and is able to be printed down to a slightly lower relative density. These were more limited by the ability of these slender beams to avoid drooping of the tensile head as it rotates into an inaccessible orientation.

The typical scaling laws describing the properties of lattices are based on the relative density, but anecdotally it seems that printability is more closely related to the slenderness ratio of the beams printed. For the current project, these problems manifested in the form of poor notch integrity due to the worsened ability to print overhangs at lower slenderness ratio, and an inability to hold the top loading pin and head in place as the support beams grew more slender. As is typical, relative density will refer to the weight of the printed lattice divided by the weight of a block of the same material occupying the same footprint volume. As these lattices are microscopic, it is not feasible to weigh them, so we image the printed beams and then recreate this geometry unit cell on SolidWorks. Once we have the representative geometry, which tended to be about 3.4% more dense than the intended, we can calculate the model volume and divide by the volume of a solid enclosing the footprint of that unit cell. The slenderness ratio is defined as the radius of the beam divided by the length of the beam. Relative density is related to the square of the

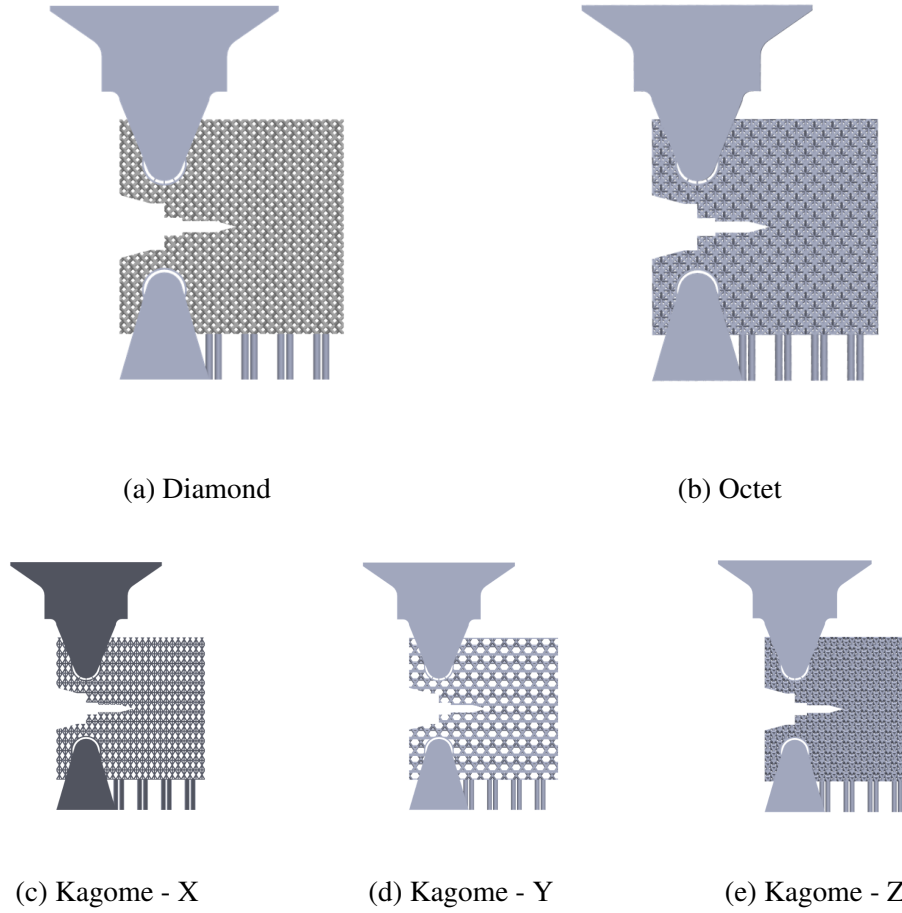


Figure 2.10: CAD drawings of the 5 different lattice architectures considered.

slenderness ratio, as shown by Deshpande, Fleck, and Ashby [4].

$$\rho = 6\sqrt{2}\pi \left(\frac{R}{L}\right)^2 \quad (2.2)$$

For sufficiently thick beams, there is a cubic correction that is added to negate the double-counting encountered at the nodes, which would be the site of overlapping beams should they each be considered independently. The magnitude of this correction was found by fitting CAD models of various unit cell drawings [5].

$$\rho = 6\sqrt{2}\pi \left(\frac{R}{L}\right)^2 - 54.6 \left(\frac{R}{L}\right)^3 \quad (2.3)$$

Shown in Figure 2.12 is the relationship between the relative density and the slenderness ratio for the different lattice geometries considered here. The theoretical relationship as described in Equation 2.2 for the octet lattice geometry is shown as

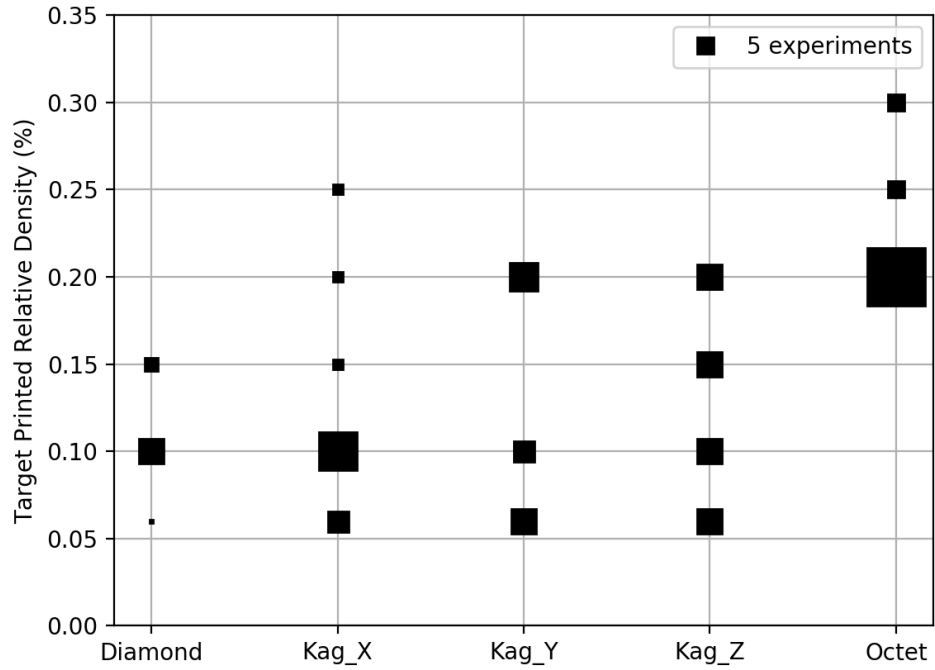


Figure 2.11: Parameter space presented. The larger the marker, the more experiments done at those conditions.

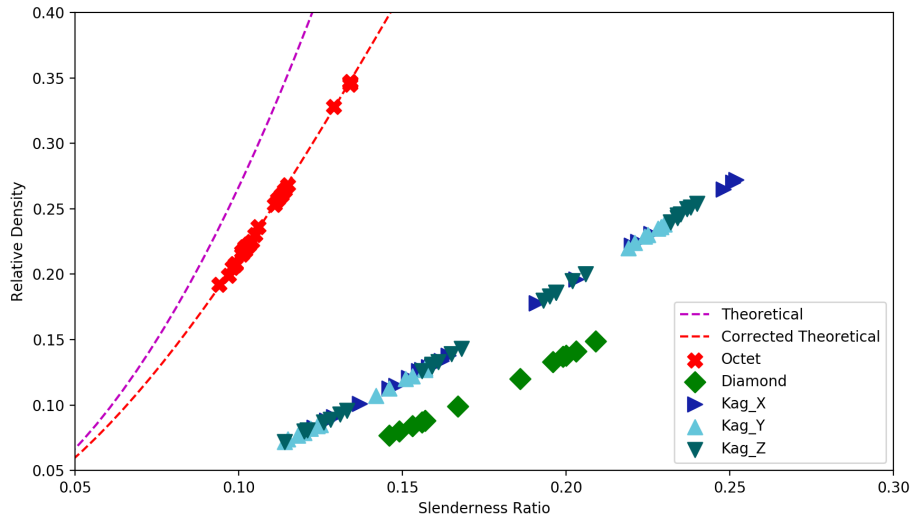


Figure 2.12: Relationship between relative density and slenderness ratio for each of the tested architectures.

the dashed magenta line, and that of Equation 2.3 in red. The drastically different slope of the octet relationship in this parameter space versus that for the diamond unit cell shows why the octet unit cells were mostly toward the higher end of relative density considered, and the diamond were toward the lower end.

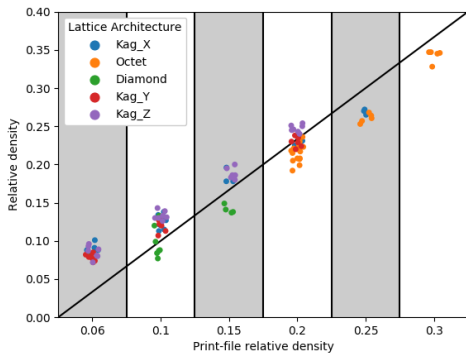
The actual relative density of a sample does not always match the relative density prescribed by the print file. The prescribed relative density comes from the Solid-Works file that is created and prepared for print with DeScribe, and the measured relative density is found by imaging the resultant lattice in the SEM, measuring several beam lengths and diameters, then redrawing and calculating from these measured dimensions. Print-file relative density will refer to that prescribed by the drawings, and relative density will refer to the measured value from imaging of the lattices.

Printing parameters such as layering, hatching, and laser power influence the size and spacing of the voxel used for printing. Depending on the geometry of the structure to be printed, and the desired feature sizes, there is a different relationship between the prescribed and measured relative density. This relationship is shown in Figure 2.13a. It seems that there is a trend toward a higher positive percent error for lower relative density lattices that decreases and perhaps changes signs around 22% relative density. This could be a result in difficulty resolving the nodes for smaller beam at these low relative densities. At higher relative densities, the node volume should be larger, and therefore the separation between beams will be more distinct, which should be an easier configuration for the printer to produce.

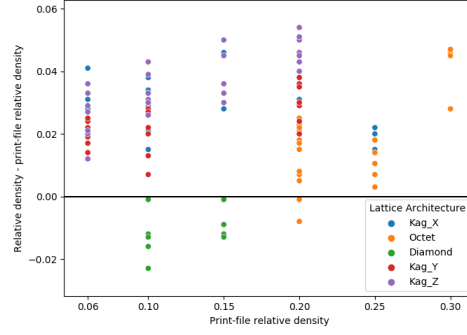
Looking at the absolute difference between relative density measured versus print-file relative density in Figure 2.13b, it seems that the diamond architected lattices tend to have a slightly lower relative density than prescribed, while the other architectures tend to be slightly higher than anticipated. This could be in part due to the consistent beam-to-laser angle during printing giving rise to constant beam diameters in the diamond architecture as opposed to the two distinct groupings of beam diameters observed for octet and kagome architectures.

2.5 Loading data

Average loading curves separated by print-file relative density and by the groupings of measured relative density that emerged are shown in Figures 2.14 and 2.15. All of the structures show a smooth linear loading until the point of crack initiation at the maximum load. For diamond, the load is decreased most slowly with continued crack



(a) Actual RD versus prescribed RD.



(b) Difference in RD as a function of print-file RD.

Figure 2.13: Plots showing the relationship between the print-file relative density and the measured relative density. Jitter is added to the print-file RD in part (a) to aid in visualization.

extension, perhaps partially due to its propensity to deflect, but also the inherent bending mechanisms would make for a more sustained load during crack extension. The octet lattices reached the highest maximal loads and decreases relatively linearly as the crack extends. Kagome has the most interesting post crack initiation features. These curves show sharp drops of load, which seem to correspond to the progressive breaking nodes. As the crack extends, there is a slowing in the decrease in load, which suggests that the local stress state in front of the crack tip is not the same throughout these experiments. There was an unsuccessful attempt to correlate each peak to a plane of nodes breaking, but it was not successful. Especially for the kagome_x samples due to the preferential viewing angle, it should be possible to correlate the step-wise increase in fracture area with the energy of each of these segments past the peak load phase.

In the typical fashion of lattice work, we will calculate the exponents of the scaling law of yielding stress, stiffness, and critical stress intensity factor (K_{IC}) of these lattices with relative density ($\bar{\rho} = \frac{\rho_{lattice}}{\rho_{material}}$).

$$\sigma_y \propto \sigma_{ma} \bar{\rho}^l \quad (2.4)$$

$$S \propto S_{ma} \bar{\rho}^m \quad (2.5)$$

$$K_{IC} \propto K_{IC\ ma} \bar{\rho}^n \quad (2.6)$$

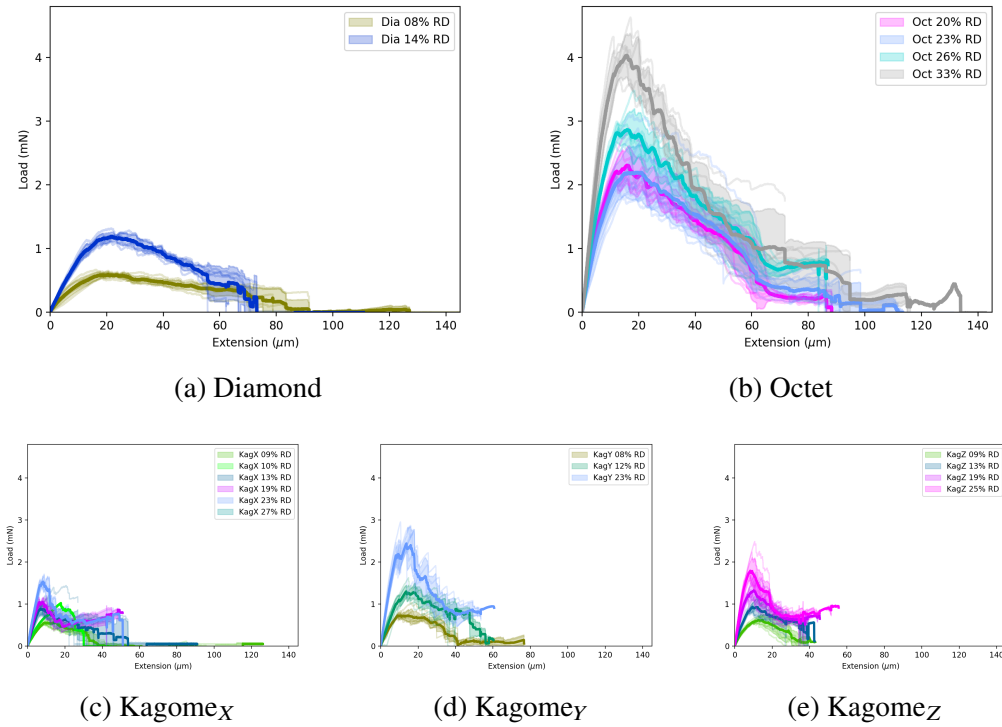


Figure 2.14: Plots showing the average loading displacement curves for groupings of measured relative density values. The faint lines are individual experiments, the thick line is the average, and the shaded portion is one standard deviation.

These power-law relationships of the form $y = Ax^B$ give insight into how sensitive (b) the measured property (y) changes as a function of the relevant material property (A) as a function of an independent variable (x), which is relative density ($\bar{\rho}$) here.

Elastic loading stiffness was found by taking the slope of the load-extension curve from $0.2 \mu\text{m}$ to $1.5 \mu\text{m}$ of extension.

Summarizing these power-law relations with the measured relative density values in Table 2.4 it can be seen that critical stress intensity factor for kagome does not scale as strongly with relative density as it does for the other architectures, as is predicted from 2D simulation literature [6], and the characteristic value seems lower, other than for the Y-oriented samples. It could be that these samples are at a relative density high enough such that the low scaling law has overtaken the inherent toughening mechanisms suggested from these beam-pin joint models.

Upon changing orientation, there are a few features that might be responsible for these anisotropic behaviors. Most notably is the different plane of nodes with closest alignment to the crack tip. Crack extension will occur along the plane

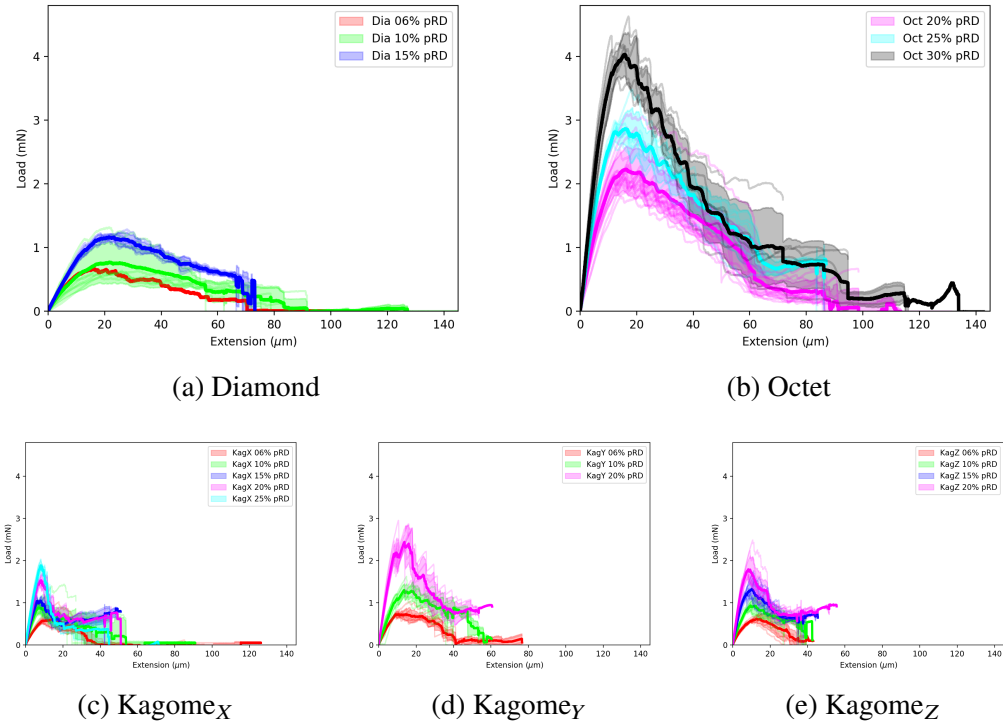


Figure 2.15: Plots showing the average loading displacement curves grouped by print-file relative density. The faint lines are individual experiments, the thick line is the average, and the shaded portion is one standard deviation.

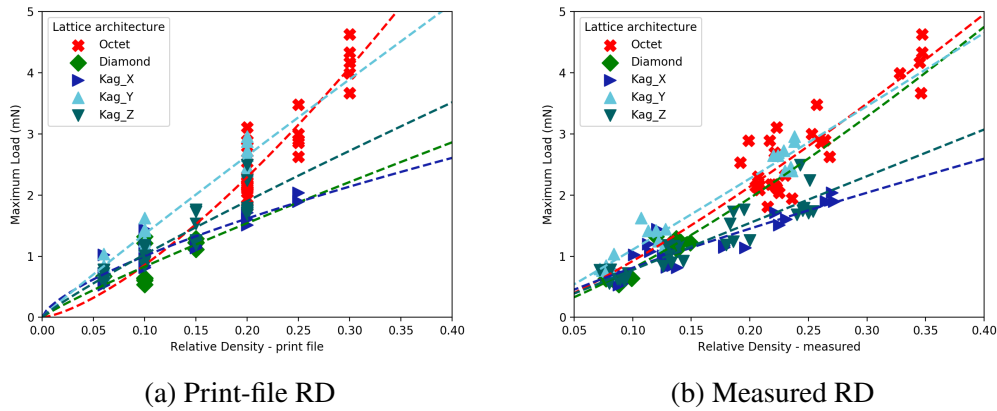


Figure 2.16: Power-law relationship between the maximum load achieved and the print-file/measured relative density for each of the tested architectures.

Power-law fit parameters - Maximum load				
	Print-file RD		Measured RD	
Lattice architecture	A_p	B_p	A_m	B_m
Diamond	6.49 ± 4.70	0.89 ± 0.34	15.4 ± 6.37	1.28 ± 0.20
Kagome _X	4.91 ± 0.58	0.69 ± 0.06	5.60 ± 0.85	0.84 ± 0.09
Kagome _Y	12.32 ± 1.20	0.96 ± 0.05	12.02 ± 1.34	1.04 ± 0.07
Kagome _Z	7.93 ± 1.33	0.89 ± 0.09	7.63 ± 1.28	0.99 ± 0.10
Octet	22.63 ± 4.36	1.42 ± 0.14	15.1 ± 2.58	1.21 ± 0.13

Table 2.1: Power-law fit parameters for the relationship between the maximum load and measured relative density.

Power-law fit parameters - Loading stiffness				
	Print-file RD		Measured RD	
Lattice architecture	A_p	B_p	A_m	B_m
Diamond	188 ± 163	0.39 ± 0.39	467 ± 365	0.80 ± 0.36
Kagome _X	872 ± 159	0.75 ± 0.10	1031 ± 224	0.93 ± 0.13
Kagome _Y	1536 ± 337	0.99 ± 0.12	1533 ± 318	1.08 ± 0.12
Kagome _Z	1678 ± 270	1.03 ± 0.09	1630 ± 245	1.16 ± 0.09
Octet	1841 ± 507	1.21 ± 0.19	1215 ± 304	0.98 ± 0.18

Table 2.2: Power-law fit parameters for the relationship between the loading stiffness and measured relative density.

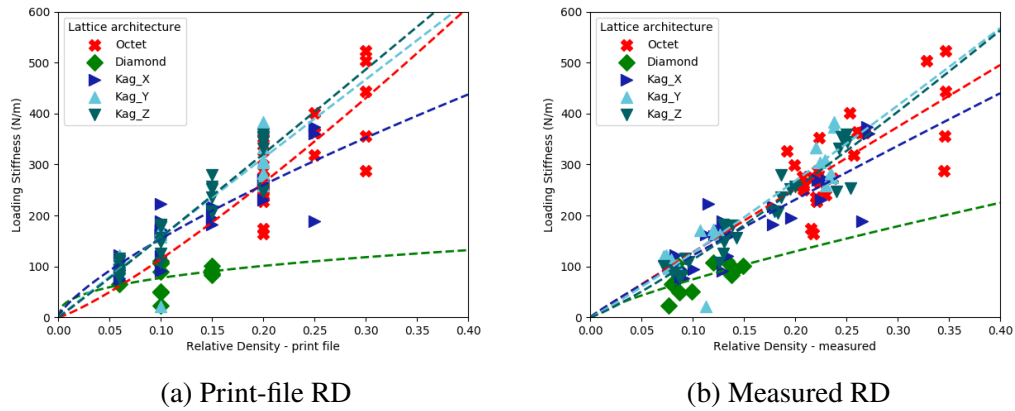


Figure 2.17: Power-law relationship between the loading stiffness and the print-file/measured relative density for each of the tested architectures.

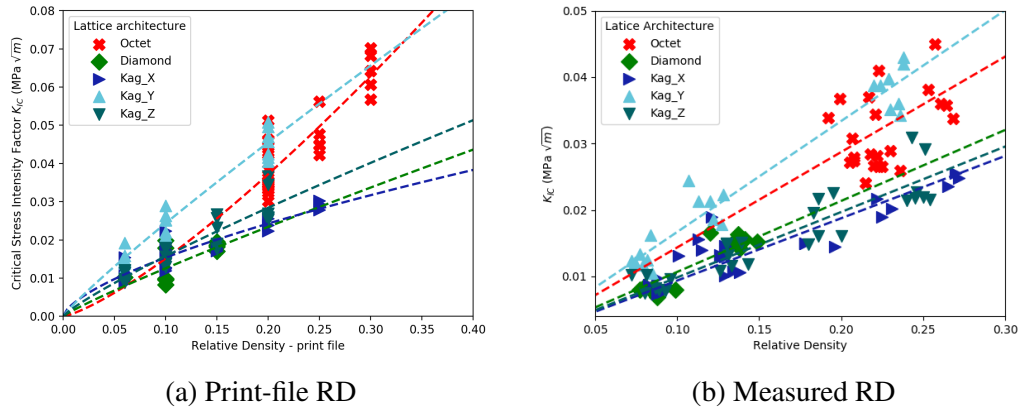


Figure 2.18: Power-law relationship between the critical stress intensity factor (K_{IC}) and the print-file/measured relative density for each of the tested architectures.

of least resistance, which is often produced via stress concentrators. It has been shown that cracks prefer extension along a plane of nodes in lattices [1], but the local stress state is drastically altered when a crack extends non-orthogonally to the loading direction. These changes make it difficult to confidently calculate a reliable toughness value at different points of crack extension.

The diamond lattices have a softer loading stiffness, as expected from their bending-dominant nature. Interestingly, the kagome lattices, other than the X-orientation appear to be the stiffest lattices. Knowledge of the full elastic surface for a kagome lattice was not found in the literature, but it would be useful for comparison between these other lattices. The scaling between all of these architectures is about the same, other than diamond, which is slightly lower.

Power-law fit parameters - K_{IC}				
	Print-file RD		Measured RD	
Lattice architecture	A_p	B_p	A_m	B_m
Diamond	0.10 ± 0.07	0.90 ± 0.33	0.22 ± 0.09	1.26 ± 0.19
Kagome _X	0.07 ± 0.01	0.66 ± 0.06	0.08 ± 0.01	0.80 ± 0.09
Kagome _Y	0.20 ± 0.02	0.90 ± 0.05	0.19 ± 0.02	0.98 ± 0.07
Kagome _Z	0.11 ± 0.02	0.85 ± 0.09	0.11 ± 0.02	0.96 ± 0.10
Octet	0.30 ± 0.06	1.30 ± 0.14	0.21 ± 0.04	1.11 ± 0.13

Table 2.3: Power-law fit parameters for the relationship between K_{IC} and measured relative density.

Power-law fits			
Lattice architecture	Maximum load (mN)	Loading stiffness (N/m)	K_{IC} ($MPa\sqrt{m}$)
Diamond	$15.4 \bar{\rho}^{1.28}$	$467 \bar{\rho}^{0.80}$	$0.22 \bar{\rho}^{1.26}$
Kagome _X	$5.60 \bar{\rho}^{0.84}$	$1031 \bar{\rho}^{0.93}$	$0.08 \bar{\rho}^{0.80}$
Kagome _Y	$12.02 \bar{\rho}^{1.04}$	$1533 \bar{\rho}^{1.08}$	$0.19 \bar{\rho}^{0.98}$
Kagome _Z	$7.63 \bar{\rho}^{0.99}$	$1630 \bar{\rho}^{1.16}$	$0.11 \bar{\rho}^{0.96}$
Octet	$15.1 \bar{\rho}^{1.21}$	$1215 \bar{\rho}^{0.98}$	$0.21 \bar{\rho}^{1.11}$

Table 2.4: Power-law fit parameters for the relationship between the maximum load and measured relative density.

Surprisingly the octet and diamond lattices are nearly identical in terms of their maximal load scaling law. These two structures have both a stronger characteristic value and dependence on relative density than the kagome lattices.

2.6 Crack propagation angle

The angle at which the crack extended has been categorically classified in relation to the loading axis as orthogonal, off-orthogonal, or angled. Orthogonally labelled crack trajectories represent cracks that extend perpendicularly to the loading axis, as expected. Off-orthogonal experiments are those that had minor crack deflections, and angled experiments are those in which the crack deviated significantly from

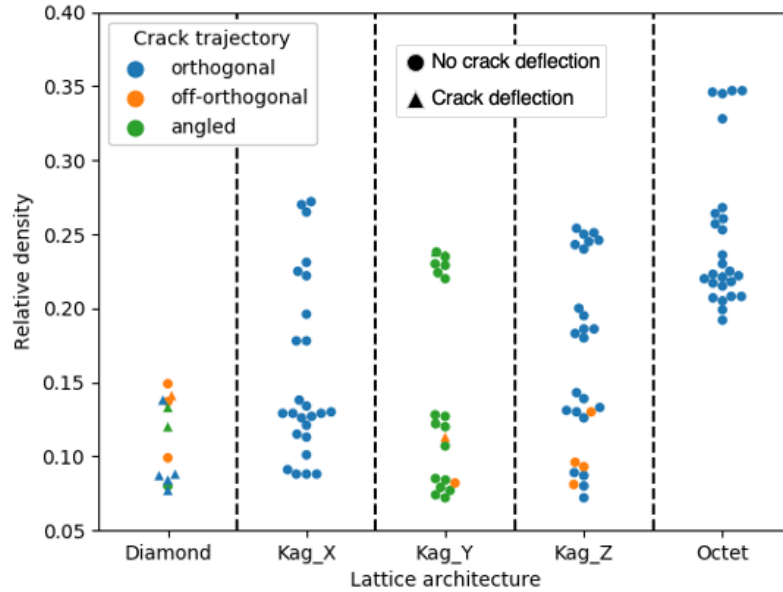


Figure 2.19: Categorized crack trajectory plotted as a function of relative density and lattice architecture.

the orthogonal plane. The crack trajectories have also been labelled for deflection. Round data points signify no crack deflection, and triangular data points signify experiments in which the crack significantly changes direction during extension. Figure 2.19 shows that most of these undesirable features occurred in the diamond and Y-orientation kagome lattices, especially at lower relative densities. The angled crack growth in this Y-orientation kagome is most likely due to the readily accessible plane of nodes being in an angled orientation. The reason for this behavior is less clear for the diamond lattices. Perhaps there is a difference in boundary conditions between the top and bottom loading pins as the crack deflection happened away from the substrate. The uniformity of the beams throughout this architecture couple with the lack of as clean a plane of nodes for the crack to potentially propagate might suggest that this lattice is not behaving in a similar manner to the other architectures. The octet lattices typically fractured half of a unit cell above the initial notch due to the more favorable plane of nodes being located as such, thus showing the expected fracture behavior. Again, the octet lattices tending to favor fracturing half a unit cell above versus below the notch suggest asymmetric loading conditions.

Appearance of a secondary crack arose toward the end of the loading as the CTOD was relatively high for some of the samples. However, this crack does not appear to be a function of CTOD as some of the samples showed what appeared to be close to free rotation around the loading pins. Figure 2.20 highlights which of the

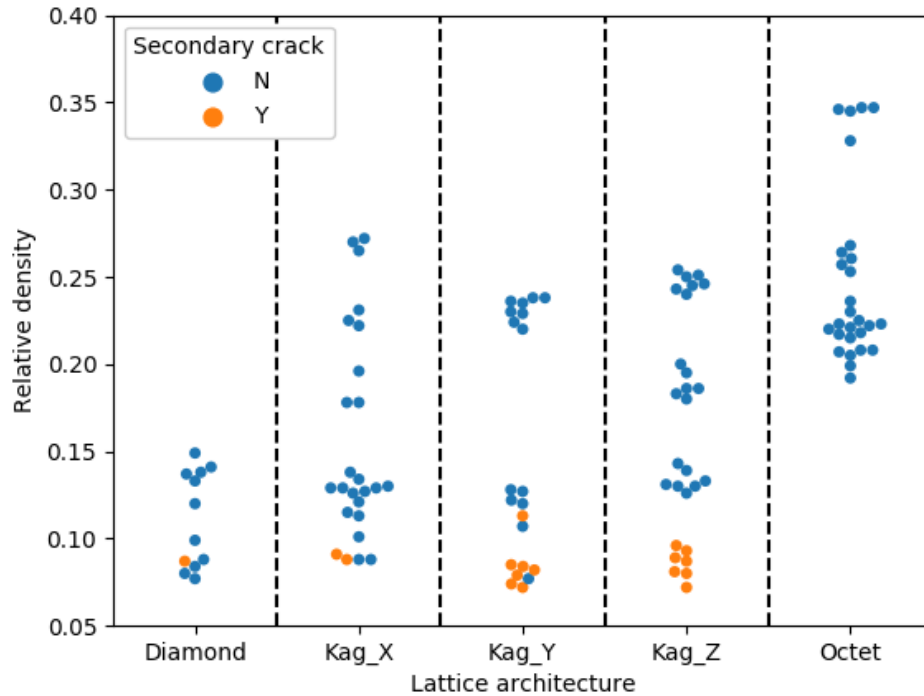


Figure 2.20: Swarmplot of relative density versus lattice architecture showing experiments that did and did not show the formation of a secondary crack.

samples had this issue. This issue seems to be strongly correlated with lower relative densities. This crack always initiated from the bottom of the lattice a few unit cells back of the lower loading pin and grew up toward the notch. The presented data has been trimmed when this behavior initiated. This sort of a crack was seen much more frequently when loading the earlier iterations of the sample geometry (see Figure 2.5), which suggests that there is still some residual torsion coming from the lower loading pin that is large enough to manifest as a crack only for these lower relative density samples. This torsion might explain some of the crack trajectory trends noted above.

2.7 Crack tip tracking algorithm¹

The goal in making these samples is to calculate a resistance curve, so there needs to be some measure of either crack extension or crack tip opening displacement (CTOD). These measurements must be done digitally given the current setup, so

¹The video analysis procedure was refined with the help of Ivan Grega, a S.U.R.F. student from the University of Cambridge.

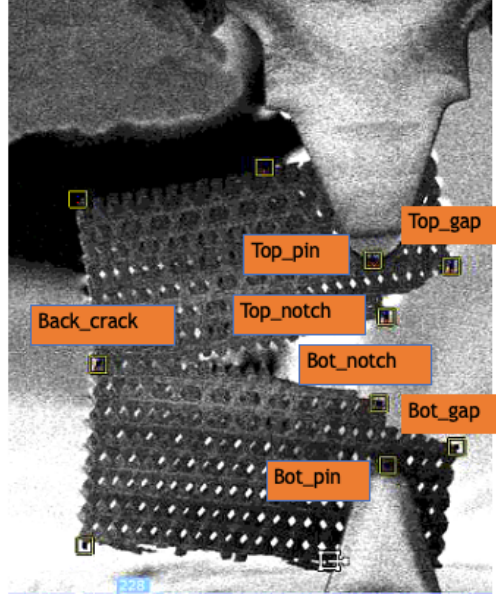


Figure 2.21: A representative frame of an in-situ test showing the points of the lattice to be tracked.

much effort was put toward forming tracking methodologies.

From the SEM videos taken during testing, we extract the crack length, crack tip opening displacement (CTOD), and pin loading angle. Features in the video that stay in-tact throughout the test are tracked using Blender, and the moving crack tip is tracked through a Python script. In 2.21 below, the square points are tracked with the "Loc" motion model via the motion tracking package in Blender, and labeled points are used for analysis. The locations are returned as pixel values, and we convert these to distance values using the scalebar shown on the videos.

Loading angle

The loading angle for each frame (θ_i) is calculated from "Top_pin" and "Bot_pin." These channels are split into their respective x and y coordinates and filtered using a low-pass Butterworth filter to reduce noise. The loading angle for the i^{th} frame is defined as shown below in 2.7.

$$\theta_i = \arctan \left(\frac{(Top_pin_y(i+1) - Top_pin_y(i)) - (Bot_pin_y(i+1) - Bot_pin_y(i))}{(Top_pin_x(i+1) - Top_pin_x(i)) - (Bot_pin_x(i+1) - Bot_pin_x(i))} \right) \quad (2.7)$$

Shown in Figure 2.22 are examples of typical loading angle behavior that was observed throughout these experiments. In Figure 2.22a there is an example of a test that is representative of most of the experiments. The loading angle starts

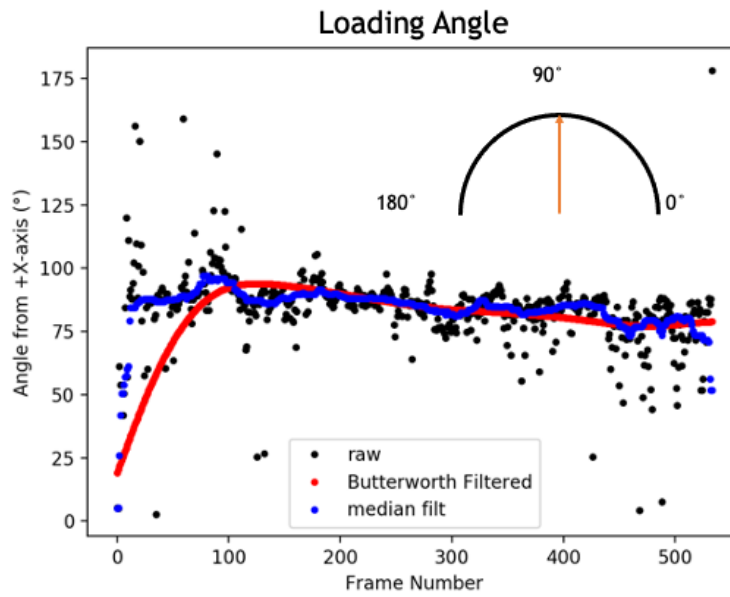
around zero as the top loading head is pulled into full contact with the indenter tip and starts to load the lattice. The loading angle is then maintained around 90° , which corresponds to ideal perpendicular to the substrate loading. The raw data is shown in black, which is a result of Equation 2.7, the blue data points are a median filter of those points, and the red data points are a low-pass Butterworth filter of this data. The blue datapoints are well behaved enough for continued calculations, and the red is probably a bit too smoothed to capture the transitions well, especially because it is prone to choosing the wrong limit for the early frame number values. The second part of this figure shows another category of experiments. This signature seems to occur more for the lower relative density lattices. The behavior is the same as previously described until a point at which the loading angle changes to more of a diagonal direction. My belief is that this is due to the supporting beams for the top loading pin not breaking completely, and the resultant torque becoming strong enough compared to the smaller and smaller unbroken portion of the sample to show up in the measured data.

Measures of crack extension

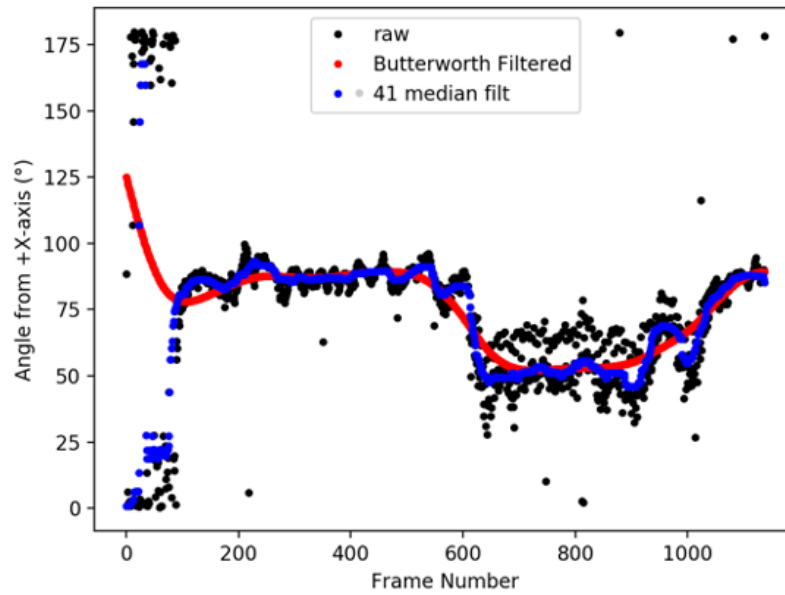
Using these tracked points we define CTOD as the difference in location between "Top_notch" and "Bot_notch."

"Back_crack" is used as part of the calculation for instantaneous crack length. The location of the crack tip is found by overlaying a Gaussian blurring over the the portion of the lattice that is not part of the crack path. This blurring helps the Python algorithm ignore the non-cracked portion of the sample. This new blurred video is then fed into Python, and we identify portions of the image that significantly change every frame. Then we filter out these changed regions based on minimum area that is changed, and location based on whether the sample is oriented such that the crack travels from left-to-right or right-to-left. Snapshots of the blurred and frame difference views of the test are shown below in 2.24. Once these points are identified, we save the "crack_tip" array and take the difference with the previously found "Back_crack" to extract the instantaneous crack length. A representative plot is shown in Figure 2.23.

Once the in-situ testing has been performed, there are several displacement measurements that we must make digitally. A representative frame of one of these videos is shown in Figure 2.24. Figure 2.24a shows one frame from the SEM video that has been cropped and blurred to help focus the attention of the algorithm to the crack tip.



(a) Flat loading angle



(b) Dip in loading angle

Figure 2.22: Plots showing progression of loading angle throughout two experiments plotted as a function of video frame number.

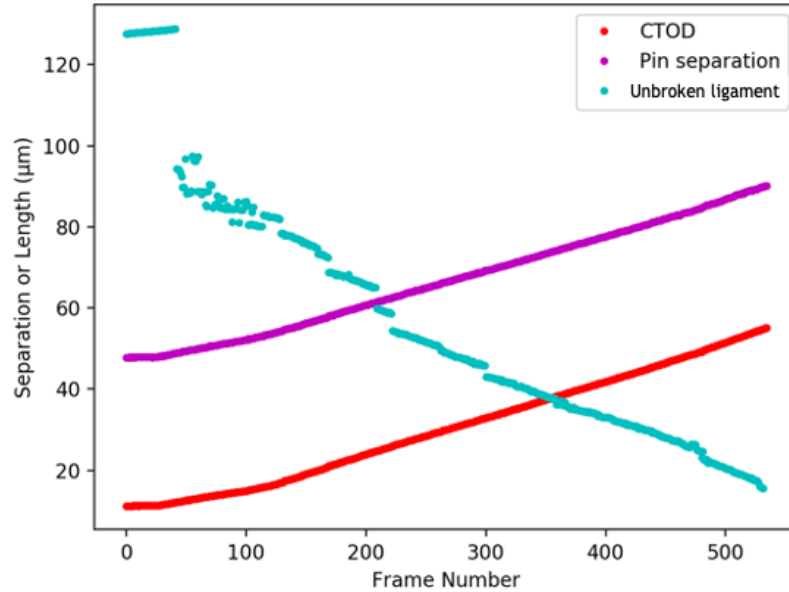
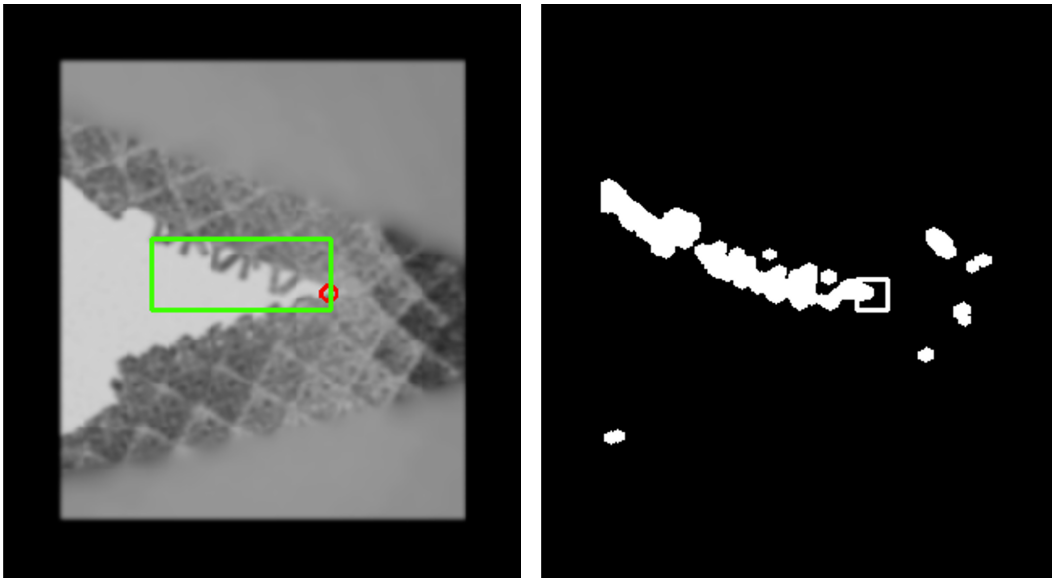


Figure 2.23: A representative trend of the unbroken ligament length, crack tip opening displacement, and loading pin separation. These data are from the same experiment as in Figure 2.22a.

Changes in grayscale pixel values from frame-to-frame are calculated, and if this difference exceeds a threshold value, then that region of the mask, as seen in Figure 2.24b, is shown in white, otherwise an area of less significant change is shown in black. Comparing these two looks of the same information shows us the upper-half of the crack nicely, but there are a few erroneous false-positives that must be dealt with. These mostly arise from areas of the lattice of large contrast changes such as holes in a low relative density lattice in which we can see all the way through to the background of the bright silicon chip and sample edges. The micrograph is cropped to remove most sample edge influences, but the beam-to-void contrast changes within the lattice are harder to avoid, and these are mostly dealt with by blurring. A 15-by-15 pixel Gaussian blur is applied to most of the lattice away from the actual crack tip, and so long as the gray value chosen for this blurring matches the lattice, then the edge of the mask is not mistaken for the the upper half of the sample being opened by the crack front. However, the other false positives that cannot be eliminated in these ways tend to be relatively small. Given the difference in size between the main feature we are using to detect the crack front, the moving halves of the opening sample, we are able to set a threshold value below which these positively identified areas are discounted. Once we have this large area of significant grayscale change, then we select either the rightmost or leftmost point of this region



(a) Cropped and blurred SEM micrograph from an in-situ testing video. (b) The same cropped region as viewed by the crack tip detection algorithm.

Figure 2.24: A representative frame of the in-situ tests being analyzed to locate the crack tip.

(depending on sample orientation) as the inferred crack tip.

In Figure 2.24a, the red circle surrounds this inferred crack tip, and the green box represents the outer borders of the continuous area of frame-by-frame change detected that is above the threshold value and at the rightmost (in this sample orientation) location in the frame. In Figure 2.24b, the white regions represent areas that the algorithm has detected a change from the previous frame. The white box highlights the inferred crack tip.

2.8 Toughness

Having the geometric parameters for each lattice, and now these instantaneous values for load, displacement angle, CTOD, and crack length, we are able to calculate the toughness throughout the test to make a resistance curve. As previously mentioned, some of the lattice geometries produced cracks paths that deviated from orthogonal to the loading direction by more than 15° , so we are discounting those here [7].

The CTOD measurements tend to be more stable than crack length measurements, so we will be continuing with the definition of toughness based on this CTOD as measured along the load-line. The Python script does not do a perfect job tracking, but there is the added difficulty in that the sample is imaged at a slight angle,

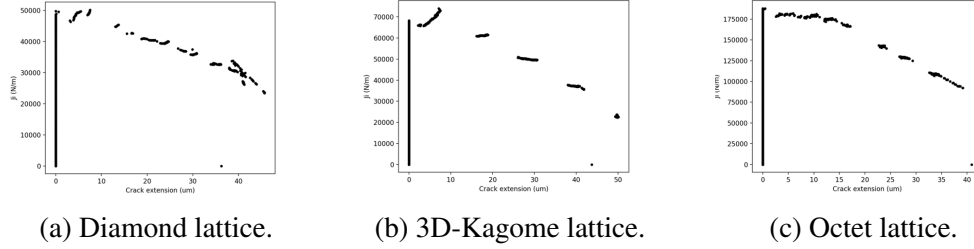


Figure 2.25: Representative J-curves for each lattice geometry as calculated by Equation 2.8.

meaning that a thin crack all the way through the sample will not show enough contrast since the imaging will be differentiating between the front and back of the sample rather than the front of the sample and the background, which tends to have a much higher contrast. For example, a sample of thickness $50 \mu\text{m}$ imaged at a 4° tilt would require a perfectly straight crack to be $3.5 \mu\text{m}$ thick before any background contrast began appearing within the crack. Moreover, cracks through these lattices are inherently step-wise, and any crack thickness will manifest as a multiple of the size of the unit cell, so the crack tends to be quite thick before revealing illumination from the background, so tracking the tip of the crack proves quite challenging.

J-integral

We have mentioned some of the disparities that the current CT system has compared to the widely accepted ASTM E1820 standard [8], but we can use the calculation of the J-integral from this standard to yield a ballpark estimate of the toughness in these CT samples. The J-integral is given as:

$$J_i = \left(1 + 0.261 \left(1 - \frac{a_i}{W}\right)\right) \left(\frac{2A_T}{Bb}\right). \quad (2.8)$$

Where A_T is the area under the load-extension curve, b is the uncracked ligament length, and the rest of the variables (a_i , W , and B) are given by the sample geometry. Shown in Figure 2.25 are representative J-curves generated from each of the tested lattice geometries. These show that the toughness increases up until the point of the crack extension, and then periodically bursts to new lower values as the crack extends further, which is a result of the periodic nature of the samples themselves.

Shown in Figure 2.26 is the combination of many of these tests into one plot with each of the datasets fit to a power-law. There have been efforts to define toughness relationships for other systems that break some of the requirements set by the standards, but these have been unsuccessfully adapted to the current work [9].

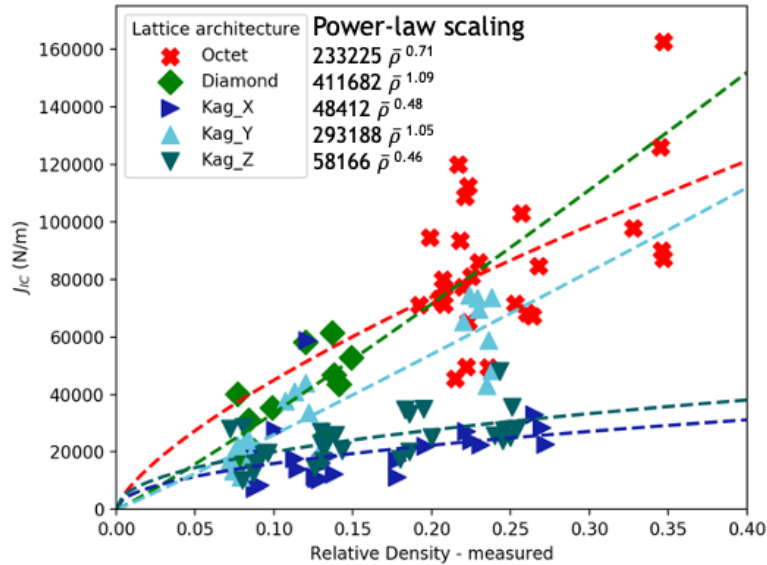


Figure 2.26: Octet sample with visible broken surface beams (circled in orange) after fracture testing.

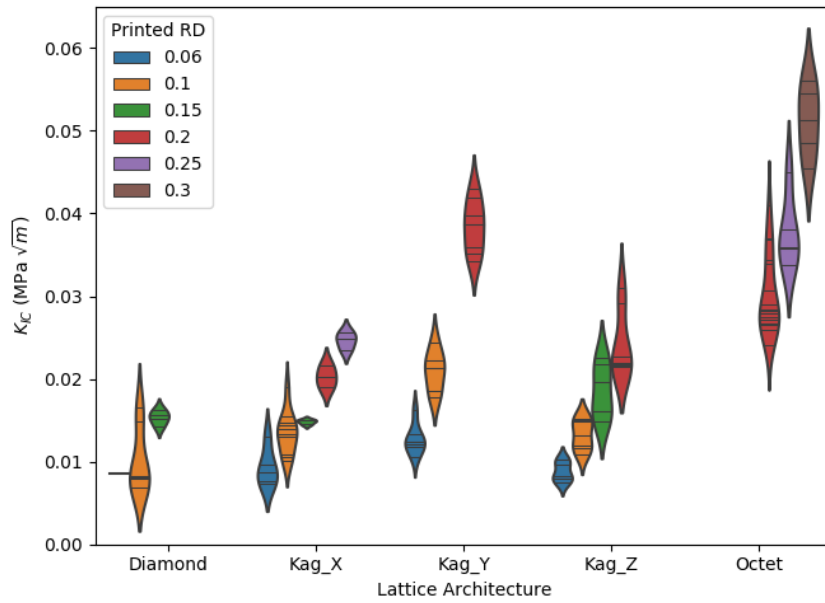
2.9 Unresolved observations

Broken surface beams

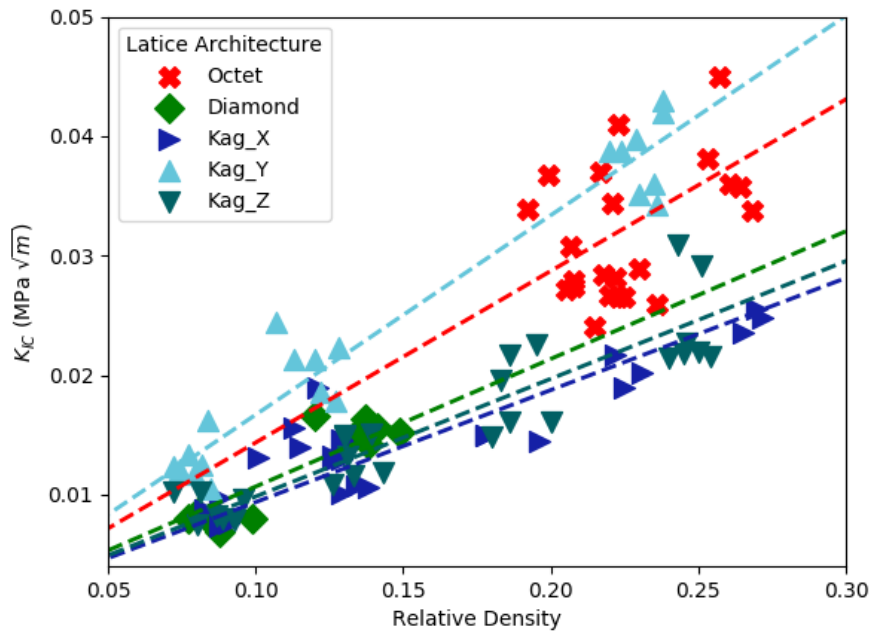
Upon more careful imaging of some of the samples after fracturing, it was observed that several beams away from the crack tip failed. we are limited in the number of beams that are observable from testing, so it is difficult to say how prevalent this behavior is throughout all of the tests, nor to what extent beams are broken in each sample as just the outermost layer of beams is observable with SEM. This observations suggests that there might be some load distribution during these experiments that is not well accounted for by our analysis methods.

Fractography

A trend for the different types of fracture surfaces observed across the broken nodes could not be resolved. The direction that the crack traveled through a node was discernible in some of the samples, but no other trend was observed, so further analysis was not done in this framework (e.g. seeing if some of the architectures or relative densities tended to look more brittle or smooth than others). Although, there should be some relationship drawn between the fractured area and the crack extension. Perhaps this would be more simply realized with more narrow samples so less nodes would be influential in the load-displacement profile.



(a) Violin plot showing the distribution of critical stress intensity factors measured for different lattice architectures and relative densities. The horizontal lines in each violin represent individual data points.



(b) Scatter plot showing the distribution of critical stress intensity factors measured for different lattice architectures and relative densities. The dashed lines are power-law fits for each of the lattice architectures.

Figure 2.27: Plots showing the measured critical stress intensity factor in response to changes in lattice architecture and relative density.

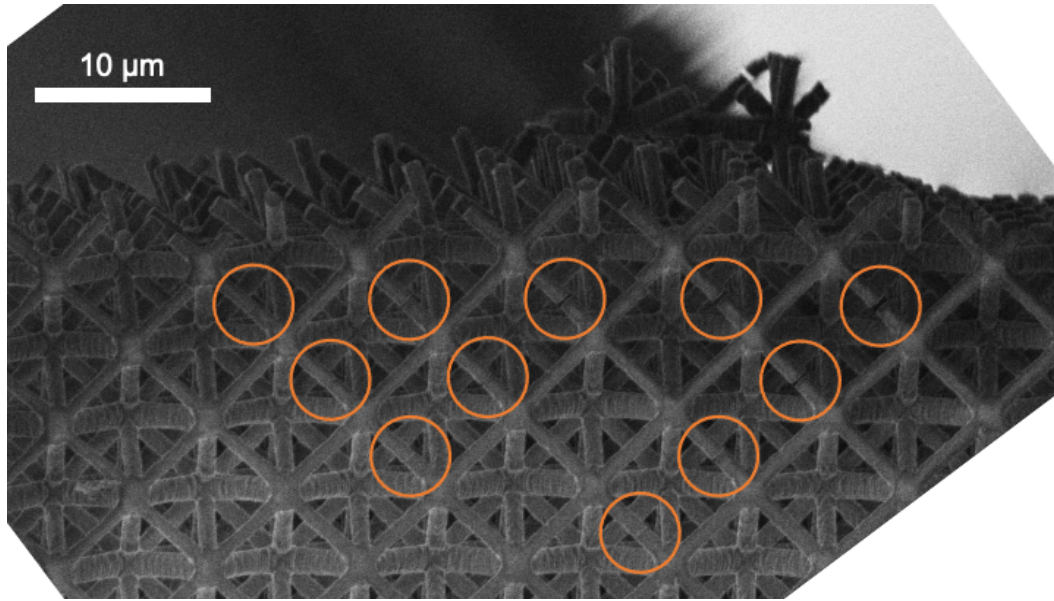
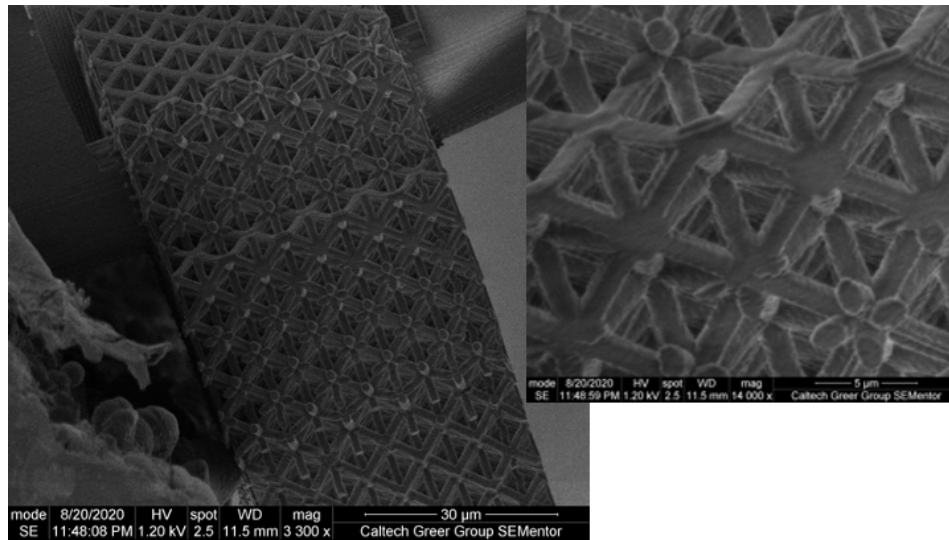


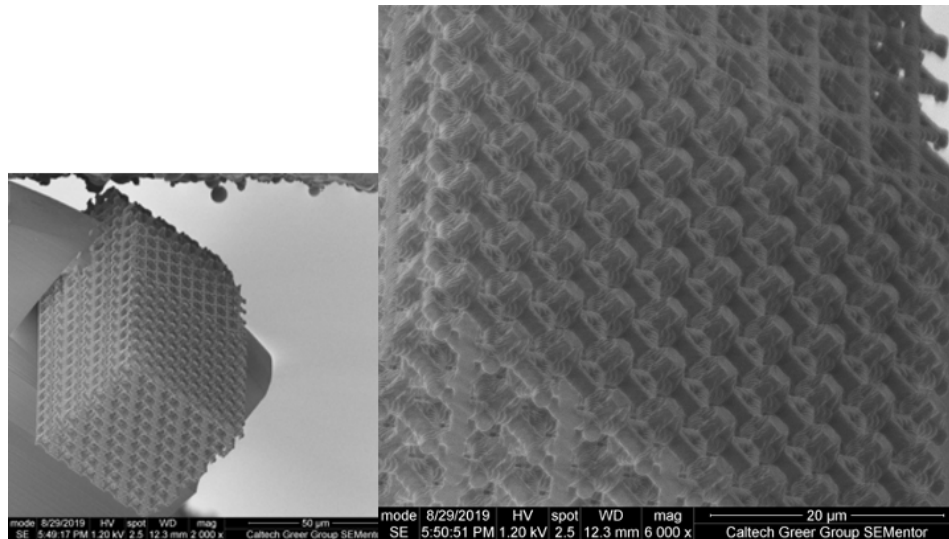
Figure 2.28: Octet sample with visible broken surface beams (circled in orange) after fracture testing.

2.10 Conclusion

A new testing methodology has been introduced to the world of microarchitected lattices for determining the toughness of such structures.



(a) Octet fracture surface.



(b) Kagome_x fracture surface.

Figure 2.29: SEM micrograph showing the top-half fracture surface of an octet and kagome lattice.

BIBLIOGRAPHY

- [1] A. J. Mateos, W. Huang, Y. W. Zhang, and J. R. Greer, “Discrete-Continuum Duality of Architected Materials: Failure, Flaws, and Fracture,” *Advanced Functional Materials*, vol. 29, no. 5, pp. 1–7, 2019, ISSN: 16163028. DOI: 10.1002/adfm.201806772.
- [2] H. Gu, S. Li, M. Pavier, M. M. Attallah, C. Paraskevoulakos, and A. Shterenlikht, “Fracture of three-dimensional lattices manufactured by selective laser melting,” *International Journal of Solids and Structures*, 2019, ISSN: 00207683. DOI: 10.1016/j.ijsolstr.2019.07.020.
- [3] C. M. Portela, J. R. Greer, and D. M. Kochmann, “Impact of node geometry on the effective stiffness of non-slender three-dimensional truss lattice architectures,” *Extreme Mechanics Letters*, vol. 22, pp. 138–148, 2018, ISSN: 23524316. DOI: 10.1016/j.eml.2018.06.004. [Online]. Available: <https://doi.org/10.1016/j.eml.2018.06.004>.
- [4] V. S. Deshpande, N. A. Fleck, and M. F. Ashby, “Effective properties of the octet-truss lattice material,” *Journal of the Mechanics and Physics of Solids*, vol. 49, no. 8, pp. 1747–1769, Aug. 2001, ISSN: 00225096. DOI: 10.1016/S0022-5096(01)00010-2. [Online]. Available: <https://linkinghub.elsevier.com/retrieve/pii/S0022509601000102>.
- [5] T. Tancogne-Dejean, A. B. Spierings, and D. Mohr, “Additively-manufactured metallic micro-lattice materials for high specific energy absorption under static and dynamic loading,” *Acta Materialia*, vol. 116, pp. 14–28, Sep. 2016, ISSN: 13596454. DOI: 10.1016/j.actamat.2016.05.054. [Online]. Available: <https://linkinghub.elsevier.com/retrieve/pii/S1359645416304153>.
- [6] N. A. Fleck and X. Qiu, “The damage tolerance of elastic-brittle, two-dimensional isotropic lattices,” *Journal of the Mechanics and Physics of Solids*, vol. 55, pp. 562–588, 2007. DOI: 10.1016/j.jmps.2006.08.004. [Online]. Available: www.elsevier.com/locate/jmps.
- [7] S. C. Forth, D. J. Herman, M. A. James, and W. M. Johnston, “Fatigue crack growth rate and stress-intensity factor corrections for out-of-plane crack growth,” *Journal of ASTM International*, vol. 2, no. 1, pp. 1–14, 2005, ISSN: 1546962X. DOI: 10.1520/JAI12026.
- [8] ASTM, “Standard Test Method for Measurement of Fracture Toughness E1820-15a,” *ASTM Book of Standards*, vol. N/A, no. 2000, pp. 1–56, 2015. DOI: 10.1520/E1820-15.
- [9] A. Ortega, P. Maimí, E. V. González, and L. Ripoll, “Compact tension specimen for orthotropic materials,” *Composites Part A: Applied Science and Manufacturing*, vol. 63, pp. 85–93, 2014, ISSN: 1359835X. DOI: 10.1016/j.

compositesa.2014.04.012. [Online]. Available: <http://dx.doi.org/10.1016/j.compositesa.2014.04.012>.

Part II

Compression of Solid Benzene

*Chapter 3***TITAN AND SMALL-MOLECULE ORGANICS**

In Part I, the material studied was an architected lattice, a composite of polymer and void space. It was suggested that a systems approach might be necessary to overcome the complexification of engineering problems that are no longer parsable into simpler one-variable problems. Sometimes the option to create a system within a material itself is available. In the case of those multifunctional materials, there is typically some sort of microstructure bringing about these unique properties. At its core, materials science focuses on the interplay between processing changes to the microstructure of a material and its resultant properties. In Part II, we approach the same question of how structure impacts material properties, but we leave behind the notion of attempting to set-up a methodology to study structural hierarchy to focus on the atomic microstructure of benzene.

3.1 Motivation to study mechanical properties of small-molecule organics

What if there were life off of Earth, and what would it look like? We do not know as there has as of yet not been any found, but we have identified several key features of an environment that might promote the proliferation of living organisms. It seems that temperature, some available light, perhaps to promote chemical reactions, and, for Earth, availability of liquid water [1] are some of these characteristics. Titan, a moon of Saturn, has a thick atmosphere in which many photochemical reactions take place, and draws heat both from the Sun and from other thermal processes under its surface. Although it is too cold for any sort of hydrological cycle, it is the only other celestial body in our solar system supporting liquid on its surface, and there is a precipitation and evaporation cycle of hydrocarbons [2]. These conditions make for an exciting landscape to explore. Perhaps there is some form of life living beneath the surface in the methane oceans, but before we are able to probe this question we must understand the mechanical properties of the surface in order to properly prepare for a successful landing mission.

The Cassini-Huygens mission has revealed a wide variety of Earth-like landforms on Titan's surface: plains, mountains, dunes, lakes, seas and rivers. The surface of Titan is covered in organic materials whose precise chemical composition is not well understood [3], [4]. Titan's surface appears to be constructed from organic

molecules, rather than the rocks and minerals that make up Earth's surface. At a surface temperature of 92 K, non-covalent interactions are sufficiently strong to enable stable interactions among these organic molecules, which form an entirely new class of cryogenic organic "minerals," or naturally occurring compounds with a specific composition [4]. The mechanical properties of these organic minerals have rarely, and in most cases never, been tested or explored. Photochemical models, partially validated by Huygens surface measurements, allow us to make a good guess on the composition of Titan's surface. While simple organic molecules like acetylene, HCN, acetonitrile, etc. in their solid form are expected to be important constituents of the surface, many of their physical properties in the solid state, at Titan-relevant temperature, are completely unknown.

Of particular interest are the widespread sand dunes that cover much of the Titan's equatorial regions, and the "Shangri-La" dune fields have been chosen as the landing site for the upcoming Dragonfly mission [5]. Multiple theories attempt to explain the origins and mechanism(s) of organic sand formation [6]; for example, Yu *et al.* reported an elastic modulus of 10.4 GPa, a hardness of 530 MPa, and a fracture toughness of $36 \text{ KPa}\sqrt{m}$ for tholins (a proxy for Titan aerosols) obtained via nanoindentation at room temperature [7]. This study extrapolated these mechanical properties to Titan-relevant temperatures of 95 K to obtain an approximate elastic modulus of 16 GPa and an approximate hardness of 800 MPa. They then concluded that these values are insufficient for these materials to have survived the transport from Titan seas or lakes around the poles to the dunes around the equator, separated by several thousand kilometers. Lorenz and Shandera [8] used spherical indentation created by an impact from a pendulum to estimate the Young's modulus of ammonia-rich ice at cryogenic temperatures. They show that around 150 K, the ammonia-rich ice is about 10-20 times softer than pure water ice, while around 100 K these ices have approximately equal elastic moduli, and extrapolating these results to 0 K shows ice to have an elastic modulus of around 10 GPa, which agrees well with previously reported values [9]. The elastic modulus of the ammonia-rich ice increases much more rapidly with decreased temperature than the water ice, which suggests that a melt isotherm could be positioned at a shallower depth under the surface than previous estimates of around 65 to 105 km below the surface [10], rendering cryovolcanism to be a more plausible contributor to the creation of Titan's thick nitrogen atmosphere [11].

Recently there was a study done to identify the upper limit of hardness of potential

surface materials on Europa to determine design parameters necessary for building sampling equipment to go on potential lander missions. This study used Leeb hardness rebound testing to show that ice-containing salts are harder than pure water ice, but are significantly softened by exposure to radiation [12]. Similarly, we aim to describe the deformation behavior of benzene to better our understanding of the surface on Titan.

The dearth of literature on the origins and the mechanical properties of organic solids that may be ubiquitously present on Titan's surface highlights the existing lack of knowledge and the speculative nature of the existing understanding of the origins of materials on Titan's surface and motivates the need for an in-depth study.

We use benzene as a model material to conduct a more comprehensive mechanical characterization of the organic minerals that may dominate Titan's surface geology [4]. Co-crystals of benzene with ethane [13], ammonia, and acetylene [8], [9] would be strong candidates for material on the outer-lying layers of the surface on Titan. We developed a methodology whereby 2 mL of liquid benzene is cryogenically frozen directly on a sample holder in an in-situ SEM and then mechanically compressed once solidified to reveal the relationship between contact pressure and displacement at 125 K. A better understanding of the mechanical properties of materials that make up the surface of Titan will enable more accurate geological modeling of surface features, and to better constrain requirements for surface sampling systems on future lander missions to Titan.

3.2 Determining a proxy material system to investigate

As the surface is not yet known, there are many potential materials to use as a proxy to understand this foreign landscape. Since it is solid at room temperature, paraffin wax was loaded into the SEMentor and indentation was attempted. Both at ambient and cryogenic temperatures this proved challenging as the wax adhered to the tip very readily, making it impossible to determine the contact area between the indenter and sample after contact is made. This is shown in Figure 3.1 on two different indenter tips.

A sample of pyrolyzed carbon from Kai Narita, a fellow group member, was used for test validation on the Oliver and Pharr indentation [14] technique to be used for these cryogenic experiments. Using regions of the sample that were affixed relatively well to the substrate, as seen in Figure 3.2, indents were done at a few different temperatures. Hardness values around 0.9 GPa are in agreement with

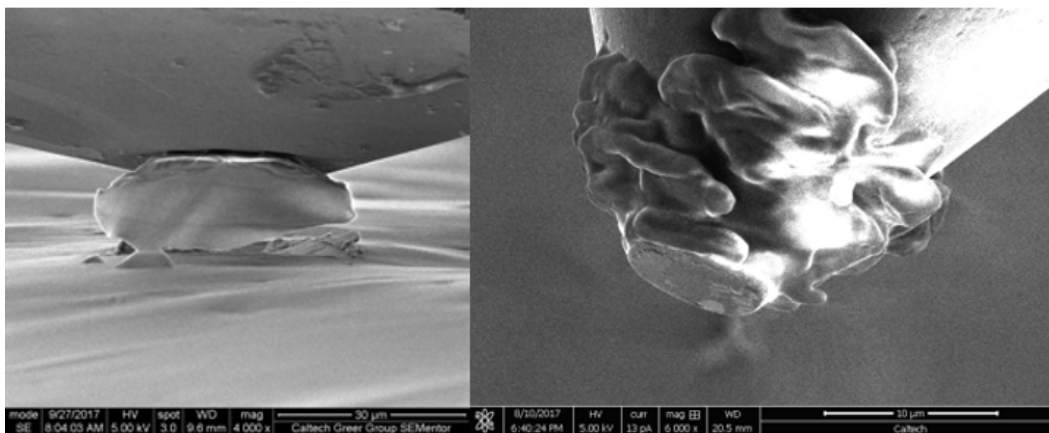


Figure 3.1: Paraffin wax stuck to two indenter tips.

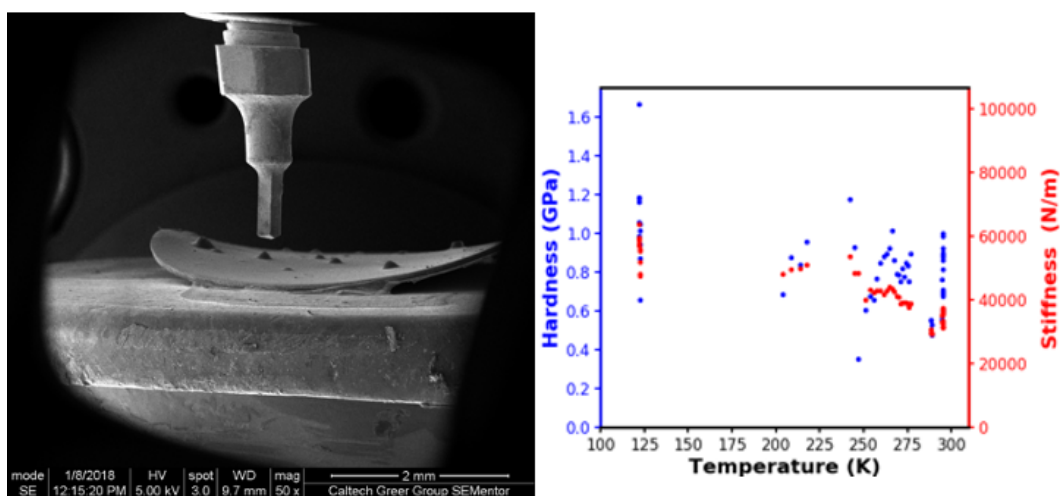
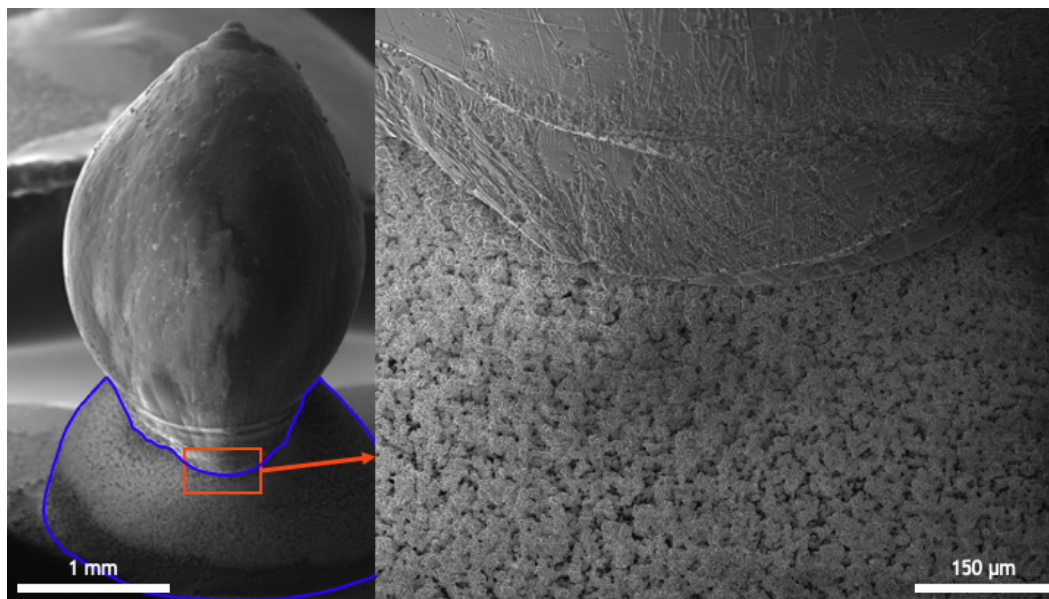


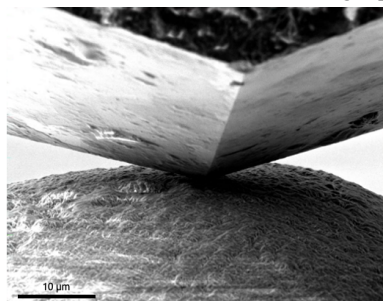
Figure 3.2: SEM micrograph of carbon sample loaded under the indenter tip, and the resulting data gathered.

values typically found in literature [15], [16], so this was seen as a successful demonstration of this widely accepted indentation technique.

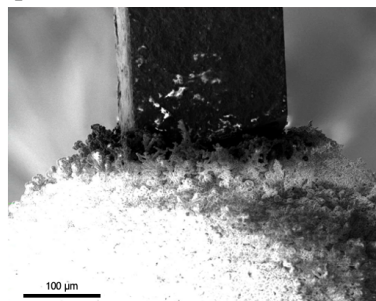
IPDIP was briefly attempted, but it was deemed that moving on to liquid at room temperature materials would be more interesting. For refinement of the indenting method, silicon chips and SEM stubs themselves were used. No new knowledge



(a) SEM micrographs of two droplets of water-ice.



(b) Indentation of slow-cooled water-ice.



(c) Indentation of fast-cooled water-ice.

Figure 3.3: Indentation into water-ice cooled either slowly or quickly.

was gained by these exercises.

Water was used frequently to test changes to the experimental setup, and for practice of rapid sample transfer. Observing these two different characteristic water droplets was very helpful when it came time to test the other materials. The hypothesis is that a sample thermal mass of a material deposited onto the cold sample stage would cool very quickly into some sort of dendritic structure opposed to a bulk piece of material. Perhaps this is in part due to all the movement between dropping the droplet¹, moving the stage to close the chamber, and running the rough pump to evacuate the chamber before condensation of water from the atmosphere. Dropping a second or third droplet onto the first one that cools very quickly tended to create

¹Interestingly, when using a pipette, one must keep the tip a few inches away from the cold sample stage to avoid freezing of the material before deposition. Aiming through the glove bag took some practice.

frozen droplets more closely resembling ice in the typical way it is observed.

Cooling the stage to a warmer temperature did not prove to be a useful solution to this problem, as upon closing of the chamber for evacuation, there is a large increase in measured temperature due to the interaction of everything being cooled with the warm air in the room (or nitrogen in the nitrogen bag). When the stage was cooled to around 120 K, it could be expected to have a temperature increase up to around 180 K given a quick sample deposition, and the less the stage was cooled before deposition, the warmer it got during deposition and reevacuation. It is worth noting that the temperature is measured by a thermocouple soldered to thin copper wires wrapped around the metallic sample stage, so the measurement is not coming directly from the sample. Instead of changing the cooling of the stage, it was found that the rapid addition of a larger thermal mass of the sample to be cooled yielded similar results to the more slowly cooled water droplets. The preferred method ended up being to pour the liquid from a small glass vial over the entire SEM stub, which is admittedly not precise, but seemed to be repeatable enough as measured mechanical properties and observed grain morphology were consistent for different depositions.

Given this rudimentary deposition technique, more exotic materials with higher numbers on the materials safety diamond were avoided. Isopropyl alcohol (IPA) produces a relatively smooth film with clumps of nodules when cooled on the SEM stub. The surface morphology is shown in Figure 3.4. The darker gray region in the main image is the region of the SEM stub that was covered with IPA, and believed to be primarily composed of IPA, but perhaps there was some mixing with water as the humidity was condensed out of the atmosphere. On the right-hand side of this figure is, what is believed to be, water-ice. The morphology looks identical to that in the water droplet samples. Observing repeated condensation onto samples prompted the use of a glove bag purged with nitrogen, and an oxygen monitor to determine when the bag was sufficiently void of potentially humid air.

These samples did not behave as expected. It seems as if there was some sort of core-shell structure formed during this cooling process. Even after waiting up to one day for the temperature to equilibrate, the film still formed what seemed to be a solid shell with a highly viscoelastic layer underneath. Shown in Figure 3.5 is a time-lapse of this core material relaxing after unloading the indenter. Unable to characterize this material, another proxy material was sought out.

Some materials with high vapor pressures were found to be unstable in the vacuum

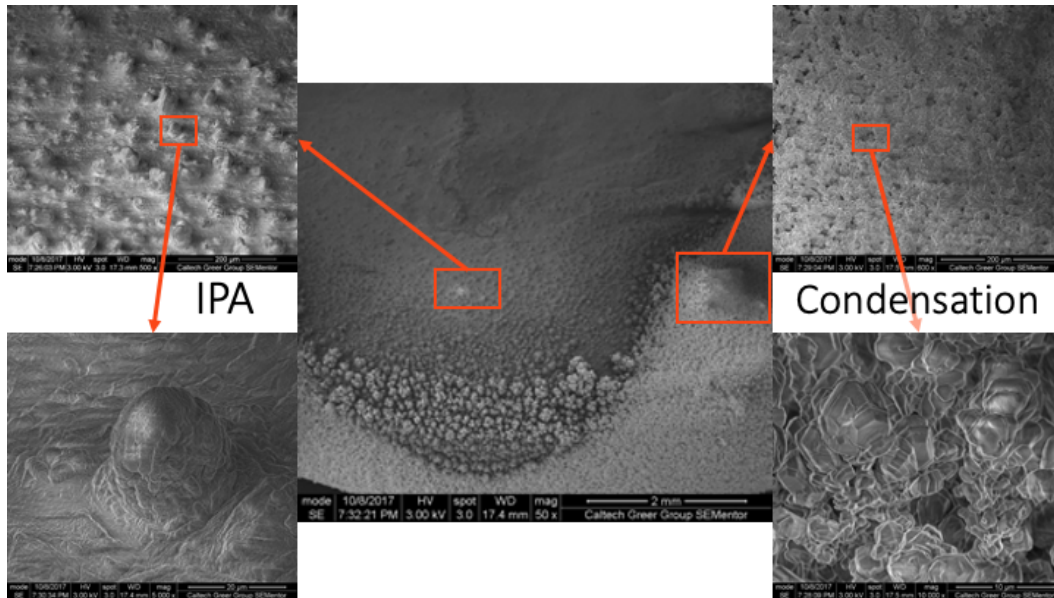


Figure 3.4: SEM micrographs showing the surface morphology of IPA, and the issue of dealing with water condensing on these samples.

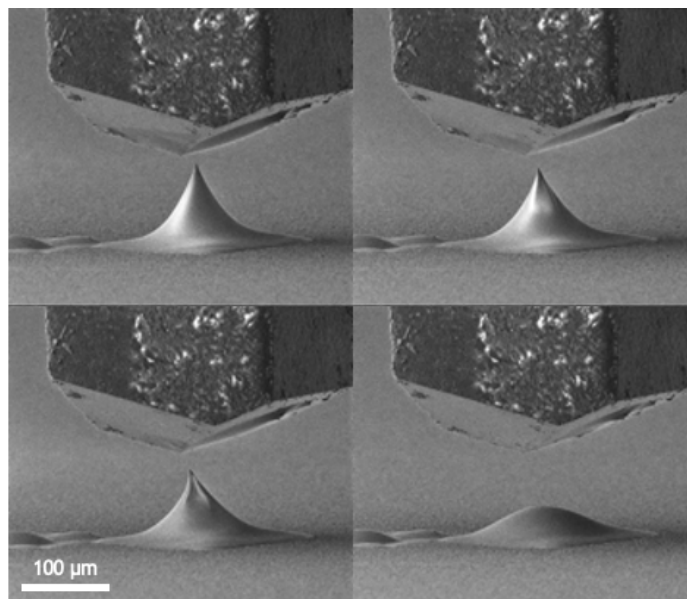


Figure 3.5: SEM micrographs showing the relaxation of IPA 0, 1, 2, 6 minutes after pulling the indenter out of contact.

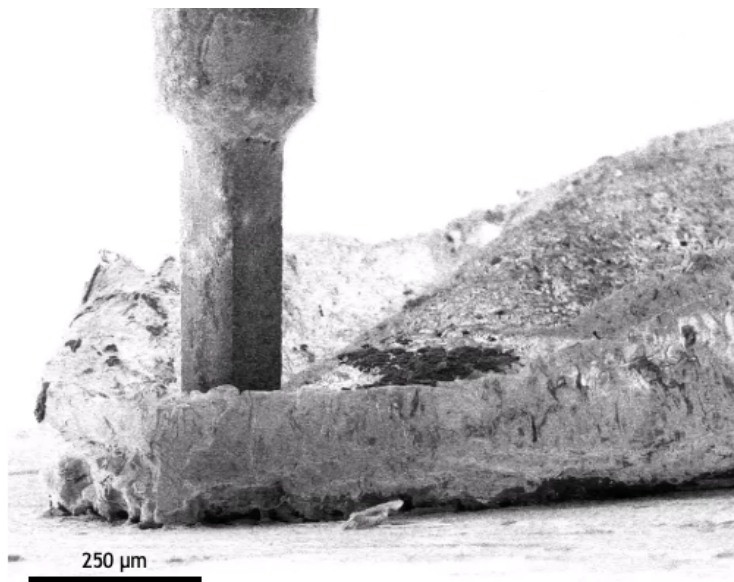
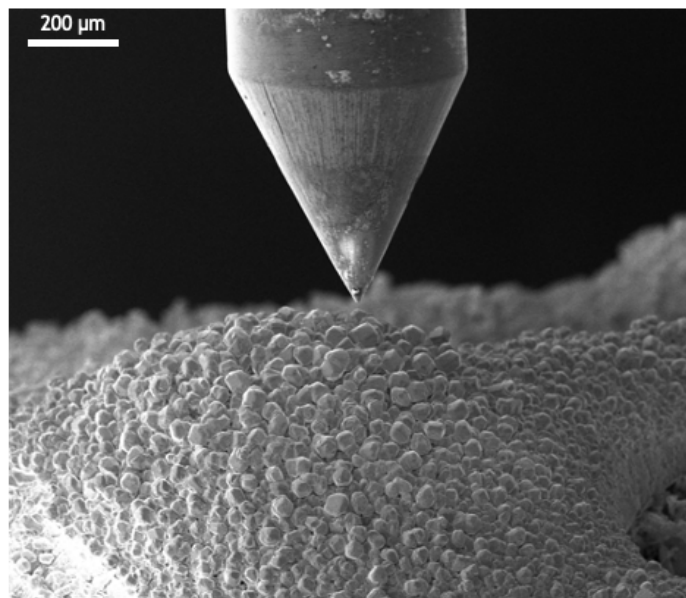


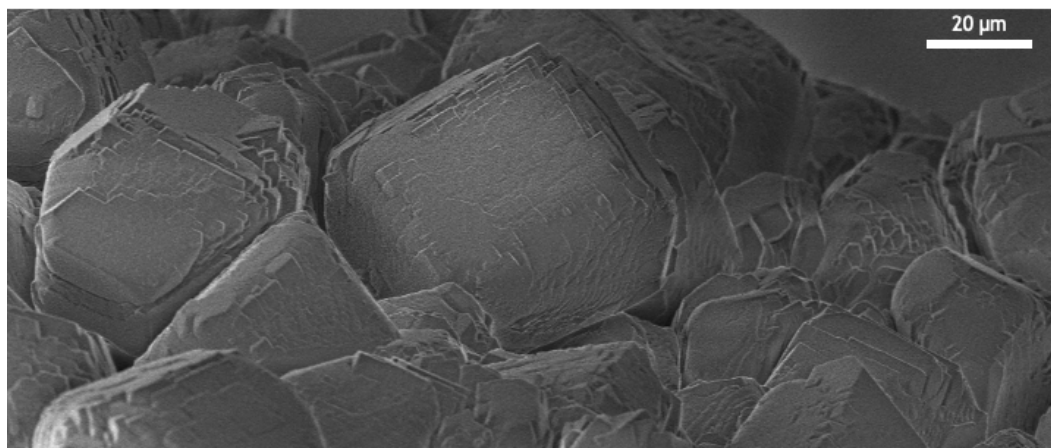
Figure 3.6: SEM micrograph with an indenter tip compressing the shell of a sublimated piece of naphthalene.

system. It seems that the sublimation due to the high vapor pressure occurred much more quickly than the rate at which the material cooled to lower this vapor pressure. Shown in Figure 3.6 is a sample of naphthalene that was put in the SEMentor to cool, but turned in to nothing more than a very weak webbing of a shell. The indenter is shown in contact, and the top of the sample deforms much like a sheet when depressed by a point-load. Biphenyl was tried as well, but there was nothing left of the sample by the time the chamber pressure was low enough for imaging.

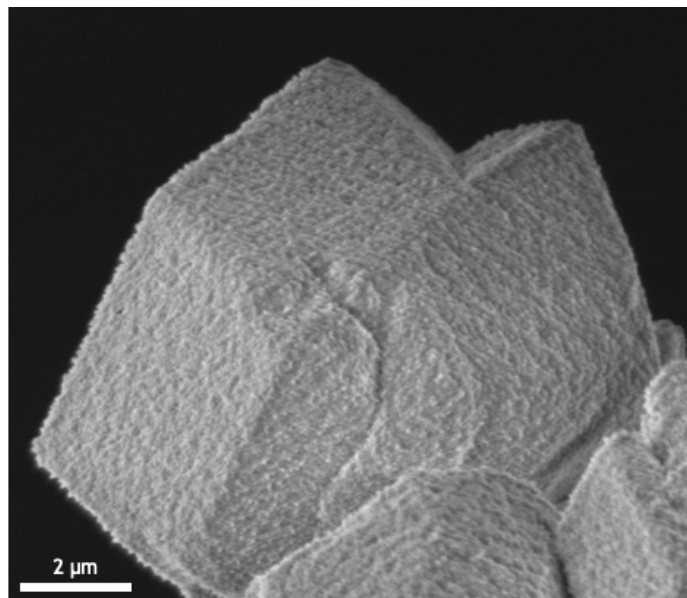
Eventually it was found that benzene readily formed crystals when cooled in this manner, and we were able to compress them individually. There are some depressions that appear to be from sublimation, but high crystal quality and relatively small/uniform crystal size suggests a relative rapid cooling rate. Since the sample stage is cold in a chamber that is not a perfect vacuum, over time there will be a build-up of material onto these cold surfaces, see Figure 4.4c compared to Figure 4.4b. So, it proved important to keep track of the surface morphology and not take too long with one cold sample. The morphology of typical benzene samples is shown in Figure 3.8, and the next chapter will detail the efforts to characterize this solid.



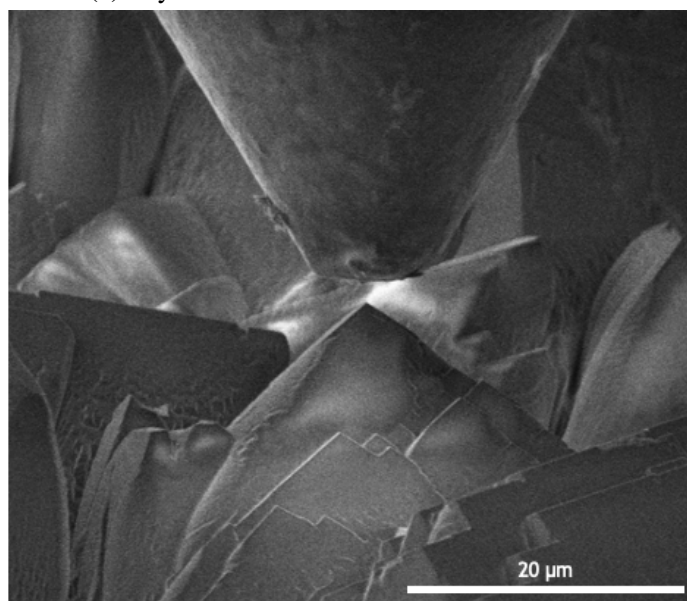
(a) Indenter over a surface of benzene crystals.



(b) Multi-faceted crystals.



(a) Crystal after several hours in the chamber.



(b) Freshly prepared crystal.

Figure 3.8: SEM micrographs showing the morphology of frozen benzene.

BIBLIOGRAPHY

- [1] C. P. McKay, “Requirements and limits for life in the context of exoplanets,” *Proceedings of the National Academy of Sciences of the United States of America*, vol. 111, no. 35, pp. 12 628–12 633, 2014, ISSN: 10916490. DOI: 10.1073/pnas.1304212111.
- [2] C. Sotin, K. J. Lawrence, B. Reinhardt, J. W. Barnes, R. H. Brown, A. G. Hayes, S. Le Mouélic, S. Rodriguez, J. M. Soderblom, L. A. Soderblom, K. H. Baines, B. J. Buratti, R. N. Clark, R. Jaumann, P. D. Nicholson, and K. Stephan, “Observations of Titan’s Northern lakes at 5 μ m: Implications for the organic cycle and geology,” *Icarus*, vol. 221, no. 2, pp. 768–786, 2012, ISSN: 00191035. DOI: 10.1016/j.icarus.2012.08.017. [Online]. Available: <http://dx.doi.org/10.1016/j.icarus.2012.08.017>.
- [3] D. Cordier, T. Cornet, J. Barnes, S. MacKenzie, T. Le Bahers, D. Nnamvondo, P. Rannou, and A. Ferreira, “Structure of Titan’s evaporites,” *Icarus*, vol. 270, pp. 41–56, May 2016, ISSN: 00191035. DOI: 10.1016/j.icarus.2015.12.034. [Online]. Available: <https://linkinghub.elsevier.com/retrieve/pii/S0019103515006004>.
- [4] H. E. Maynard-Casely, M. L. Cable, M. J. Malaska, T. H. Vu, M. Choukroun, and R. Hodyss, “Prospects for mineralogy on Titan,” *American Mineralogist*, vol. 103, no. 3, pp. 343–349, 2018, ISSN: 19453027. DOI: 10.2138/am-2018-6259.
- [5] R. D. Lorenz, E. P. Turtle, J. W. Barnes, M. G. Trainer, D. S. Adams, K. E. Hibbard, C. Z. Sheldon, K. Zacny, P. N. Peplowski, D. J. Lawrence, M. A. Ravine, T. G. McGee, K. S. Sotzen, S. M. MacKenzie, J. W. Langelaan, S. Schmitz, L. S. Wolfarth, and P. D. Bedini, “Dragonfly: A rotorcraft lander concept for scientific exploration at titan,” *Johns Hopkins APL Technical Digest (Applied Physics Laboratory)*, vol. 34, no. 3, pp. 374–387, 2018, ISSN: 19300530.
- [6] J. W. Barnes, R. D. Lorenz, J. Radebaugh, A. G. Hayes, K. Arnold, and C. Chandler, “Production and global transport of Titan’s sand particles,” *Planetary Science*, vol. 4, p. 1, 2015. DOI: 10.1186/s13535-015-0004-y. [Online]. Available: <https://planetary-science.springeropen.com/track/pdf/10.1186/s13535-015-0004-y>.
- [7] X. Yu, S. M. Hörst, C. He, P. McGuiggan, and B. Crawford, “Where does Titan Sand Come From: Insight from Mechanical Properties of Titan Sand Candidates,” *Journal of Geophysical Research: Planets*, 2018. [Online]. Available: <https://arxiv.org/pdf/1806.08056.pdf>.

- [8] R. Lorenz and S. Shandera, “Physical Properties of Ammonia-Rich Ice: Application to Titan,” *Geophysical Research Letters*, vol. 28, no. 2, p. 215, 2001, ISSN: 0094-8276. DOI: 10.1029/2000GL012199.
- [9] T. M. Proctor, “Low-Temperature Speed of Sound in Single-Crystal Ice,” *Journal of the Acoustical Society of America*, vol. 39, no. 5A, pp. 972–977, May 1966, ISSN: NA. DOI: 10.1121/1.1909980. [Online]. Available: <http://asa.scitation.org/doi/10.1121/1.1909980>.
- [10] F. Sohl, H. Hussmann, B. Schwentker, T. Spohn, and R. D. Lorenz, “Interior structure models and tidal Love numbers of Titan,” *Journal of Geophysical Research: Planets*, vol. 108, no. E12, pp. 1–13, 2003. DOI: 10.1029/2003je002044.
- [11] A. D. Fortes, P. M. Grindrod, S. K. Trickett, and L. Vočadlo, “Ammonium sulfate on Titan: Possible origin and role in cryovolcanism,” *Icarus*, vol. 188, no. 1, pp. 139–153, 2007, ISSN: 00191035. DOI: 10.1016/j.icarus.2006.11.002.
- [12] B. L. Henderson, M. S. Gudipati, and F. B. Bateman, “Leeb hardness of salty Europa ice analogs exposed to high-energy electrons,” *Icarus*, vol. 322, no. January, pp. 114–120, 2019, ISSN: 10902643. DOI: 10.1016/j.icarus.2019.01.006. [Online]. Available: <https://doi.org/10.1016/j.icarus.2019.01.006>.
- [13] T. H. Vu, M. L. Cable, M. Choukroun, R. Hodyss, and P. Beauchamp, “Formation of a New Benzene–Ethane Co-Crystalline Structure Under Cryogenic Conditions,” *The Journal of Physical Chemistry A*, vol. 118, no. 23, pp. 4087–4094, Jun. 2014, ISSN: 1089-5639. DOI: 10.1021/jp501698j. [Online]. Available: <http://pubs.acs.org/doi/10.1021/jp501698j>.
- [14] W. C. Oliver and P. G. M., “An improved technique for determining hardness and elastic modulus using load and displacement sensing indentation experiments,” *Journal of Materials Research*, vol. 7, no. 6, pp. 1564–1583, 1992. [Online]. Available: http://web.mit.edu/cortiz/www/3.052/3.052CourseReader/45_OliverPharr1992Nanoindentation.pdf.
- [15] K. Jurkiewicz, M. Pawlyta, D. Zygadło, D. Chrobak, S. Duber, R. Wrzalik, A. Ratuszna, and A. Burian, “Evolution of glassy carbon under heat treatment: Correlation structure–mechanical properties,” *Journal of Materials Science*, vol. 53, no. 5, pp. 3509–3523, 2018, ISSN: 15734803. DOI: 10.1007/s10853-017-1753-7.
- [16] A. Albiez and R. Schwaiger, “Size Effect on the Strength and Deformation Behavior of Glassy Carbon Nanopillars,” *MRS Advances*, vol. 4, no. 2, pp. 133–138, 2019, ISSN: 20598521. DOI: 10.1557/adv.2018.648.

Chapter 4

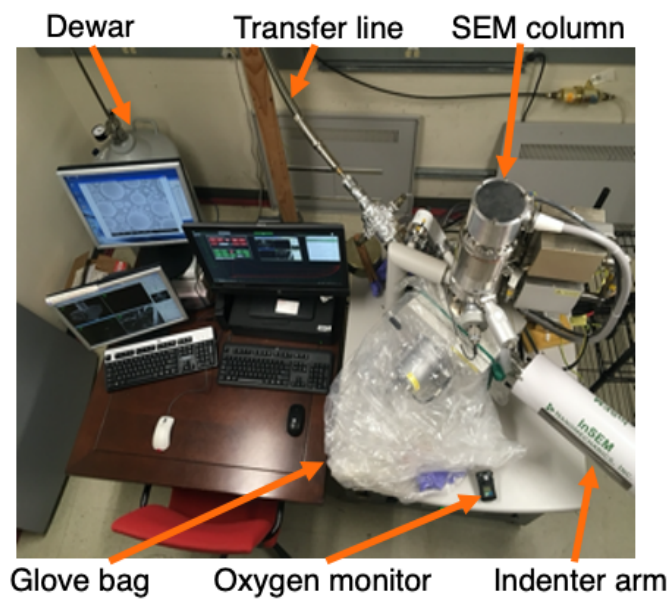
COMPRESSION OF SOLID BENZENE

4.1 Experimental methodology**Sample preparation for micromechanical experiments**

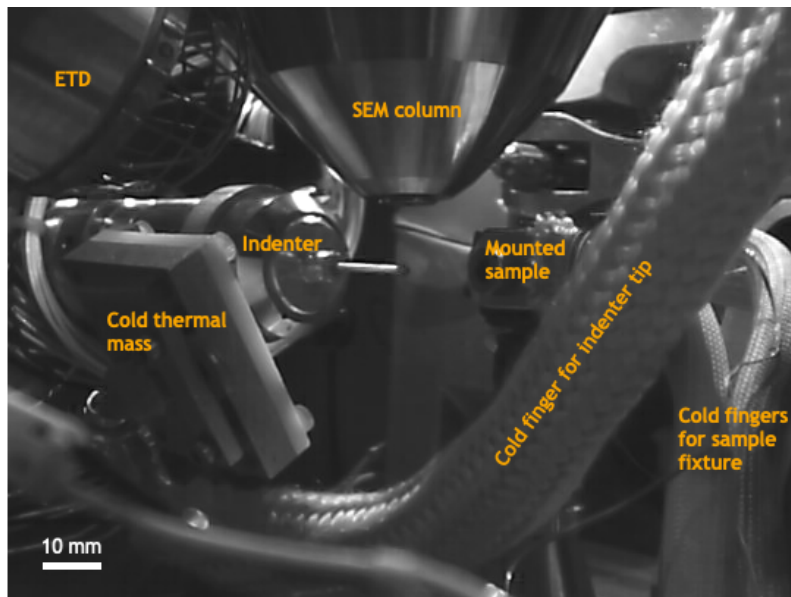
The micromechanical compression experiments were performed using a cryogenic in-situ mechanical testing set up, pictured and shown in Figure 4.1. This tool enables the recording of mechanical data while simultaneously monitoring, by a scanning electron microscope (SEM), the surface deformation occurring at a set temperature (configured by past group members [1]). This instrument will be referred to as the SEMentor. The sample holder (Ted Pella standard pin mount aluminum SEM stub) and indenter tip were cooled to ~ 125 K with copper cooling lines (40 K to 400 K capability from Janis Research Company) chilled by liquid nitrogen in an evacuated (~ 5 -10 mbar) SEM chamber (Quanta 200 from ThermoFischer Scientific, formerly FEI) equipped with a micromechanical testing module (InSEM™ from Nanomechanics Inc.). The chamber was then opened into a nitrogen atmosphere (oxygen levels below 2% measured by an MSA ALTAIR® O2 Pro) created by a N₂-purged glove bag to minimize water condensation onto the cold sample holder and sample itself. Several milliliters of anhydrous benzene (Sigma Aldrich 99.8%) were dropped onto the sample holder that was tilted to an angle $\sim 30^\circ$ off of horizontal. When a visibly sufficient amount of benzene was frozen on the sample holder, the chamber was rapidly closed and evacuated back to a pressure of $\sim 10^{-5}$ Torr. The stage temperature typically increased from ~ 125 K to ~ 180 K during the process of opening the SEM chamber to freeze the sample of benzene. This process is shown schematically in Figure 4.2. After waiting (~ 2 hours) for the temperature to equilibrate through-out the sample (SEM micrograph of typical sample morphology is shown in Figure 4.3), as seen in the last chapter, it was scanned to find crystals positioned such that a cuboid-corner of an individual benzene crystal could be positioned directly in the path of the flat punch (several crystals are shown in Figure 4.4).

In-situ compressions

Compressions of single-crystalline, cuboidal solid benzene crystals were performed by a $7 \mu\text{m}$ diamond flat-punch indenter tip at a constant loading rate of $41 \mu\text{N/s}$ to



(a) SEMentor instrument overview.



(b) Optical image inside the chamber before an experiment.

Figure 4.1: Images showing the outside and inside of the SEMentor used for these experiments.

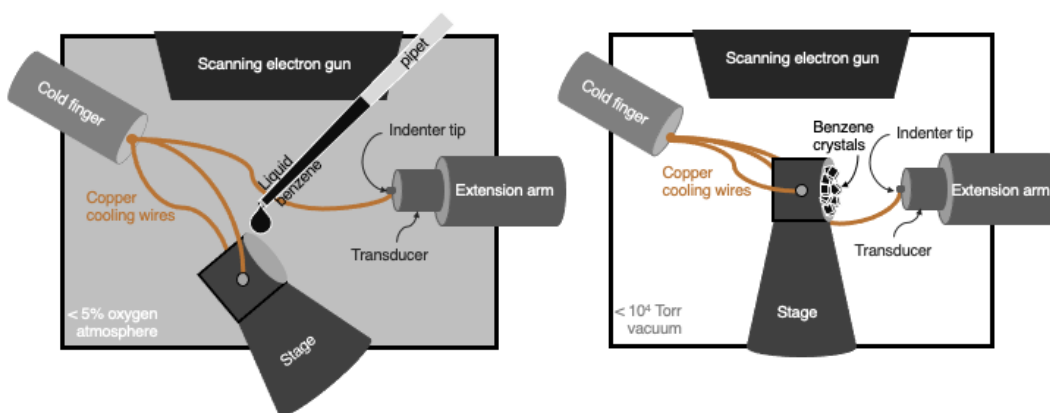


Figure 4.2: Schematic of the chamber during and after sample loading.

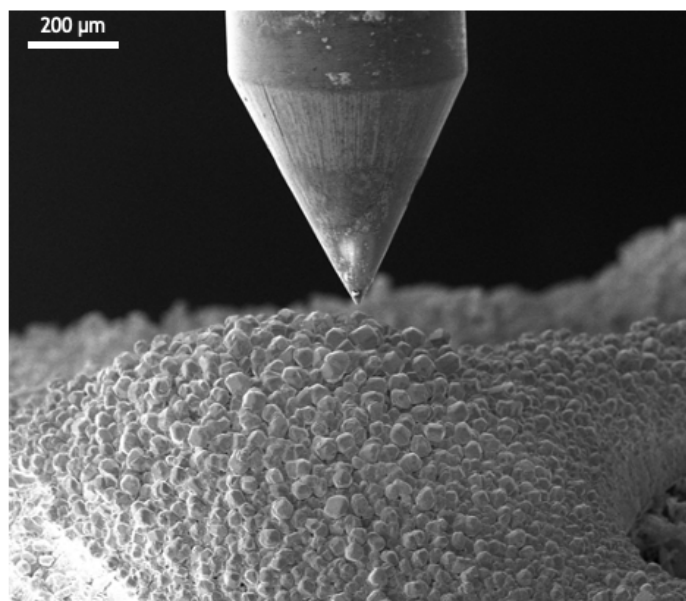
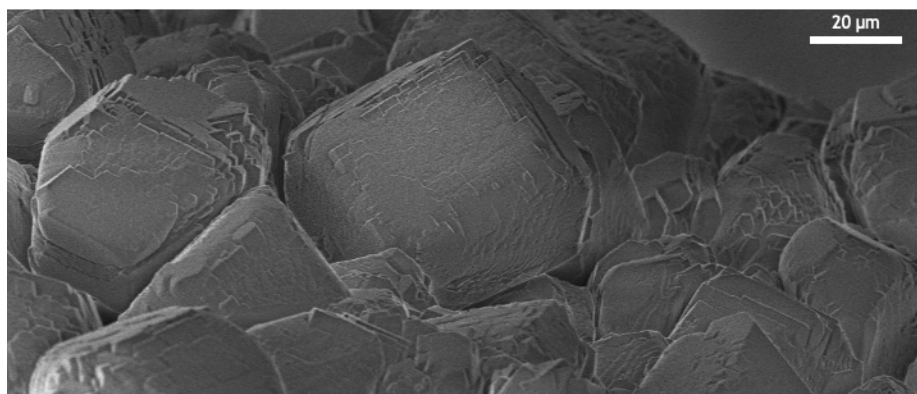
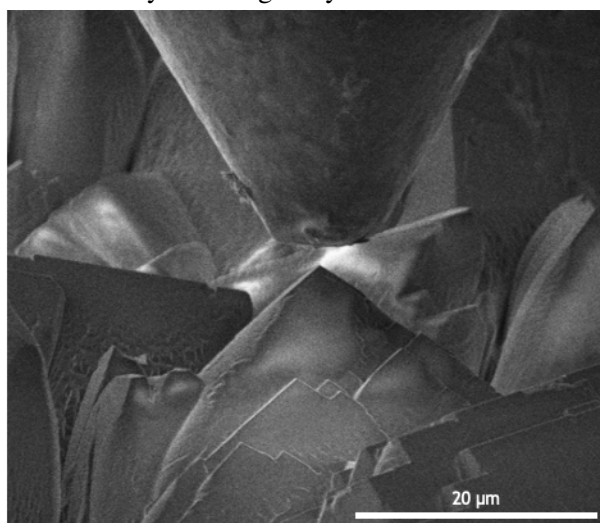


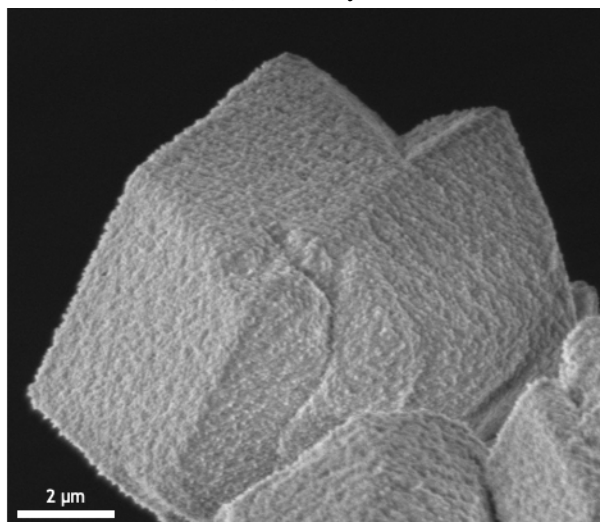
Figure 4.3: SEM micrograph of a typical benzene sample with the indenter tip above.



(a) Multifaceted crystal. Larger crystals tend to have more facets.



(b) Clean crystal.



(c) Dirty crystal. Deposition occurs over time in the chamber.

Figure 4.4: SEM micrographs of various benzene crystals.

maximal loads of up to 1.5 mN while the load and displacement were continuously measured at a rate of 100 Hz. A few compressions were also performed at 61 $\mu\text{N/s}$. The crystals were manually aligned to face the flat punch, and misalignments are assumed to be negligible.

Two loading profiles were employed for the compression experiments. One of these was to repeatedly compress the crystal to a particular load (referred to as “same reloads”), and the other was to successively compress to higher loads (referred to as “higher reloads”). The reported same reloads were done at 123.39 ± 0.99 K, and the reported higher reloads were done at 144.40 ± 0.35 K. Videos of typical compression experiments can be found in the supplementary files. Calculation of contact pressure is shown in the as-named section.

The measurement of displacement when using the cryogenic system tends to have a high level of background noise due to vibrations from the incoming liquid nitrogen, so some of the data channels (most necessarily displacement) were passed through filters as described in the next section. “Contact Pressure” is used as a proxy for stress in this study and is defined as the current “Load” divided by the instantaneous contact area between the indenter tip and sample. The contact area is calculated using a method similar to Wang *et al.* [2]. We assume compression along the n_{111} axis of a cube equivalently-sized to the unit cell proportions with side length the average of $a=7.384$ Å, $b=9.416$ Å, $c=6.757$ Å, as reported by Craven *et al.* [3], to a depth of the current “Displacement.”

Filtering the raw data

The displacement used throughout is a filtered version of the raw recorded data. Vibrations during these tests are unavoidable due to the constant evaporation of liquid nitrogen in the cold finger. Turning the flow of liquid nitrogen off helps alleviate the largest of vibrations, but those from evaporation are still present. Therefore, the raw data is passed through a median filter with a window spanning 10 data points for displacement and 160 data points for contact stiffness, but all processing of strain burst size is done through the raw data channels. The data is also processed through a low-pass Butterworth filter to provide more well-behaved functions. These are used only for calculation, and are not shown graphically. These filters were decided based on comparing plots of outputs from various parameters that were passed through the SciPy signal package (parameters shown in Table 4.1).

Low-pass Butterworth filter parameters		
Data Channel	Critical frequency	Filter order
Loading depth	0.18	3
Unloading depth	0.01	2
Loading contact pressure	0.06	8
Loading contact stiffness	0.35	1

Table 4.1: Parameters used for low-pass Butterworth filtering of noisy data channels.

4.2 Calculating contact pressure

The crystals compressed in the benzene experiments appear to be cube corners, but we cannot see the entire crystal, so it could be any prism with mutually orthogonal faces. From our TEM results, we expect these crystals to be orthorhombic, but we are unable to know along which diagonal we have compressed. So, we will take the average of the unit cell side lengths to make an effective cube yielding an equilateral triangle as the contact area used for calculating the contact pressure. This contact pressure will be used as our stress.

Compression onto a cube corner

Moving from the space of load-compression depth to contact pressure-compression depth allows comparison of a variety of sample sizes. Here we will define the contact pressure ($P_{contact}$) as the applied load (L) divided by the contact area (A):

$$P_{contact} = \frac{L}{A} \quad (4.1)$$

We are applying a known load, so that value is given at each point during the experiment, but the contact area is more difficult to deduce, so we will show our assumptions here as we modify the derivation from Wang *et al.* [2]. Our goal is to relate the contact area to a given compression displacement, which is measured. We assume that misalignments are negligible, and did not observe any “bulging” of the crystal during compression, so we are disregarding any contribution from a change in shape. The crystals that were compressed appear to be a corner of a cuboid, so we are assuming that these crystals are similar to the known orthorhombic unit cell of benzene that we confirmed with diffraction in the TEM. As it is difficult to say the exact compression direction ($[1\ 1\ 1]$, $[1\ 1\ \bar{1}]$, etc.) that we achieved in the experiment, we will make the approximation of this orthorhombic cuboid to be a

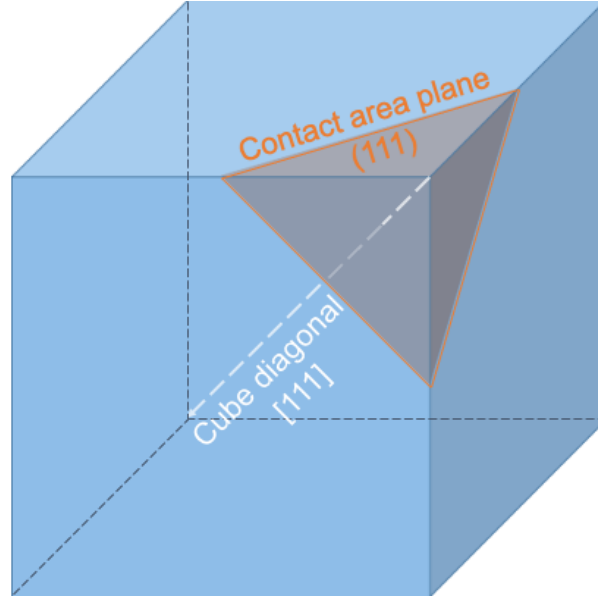


Figure 4.5: Highlighted (111) plane in a cube. This plane is assumed normal to the direction of indenter loading.

cube with dimensions of the average side lengths, of which we are compressing in the [111] direction. This also simplifies the calculation of the contact area as a cube is a special case such that the normal vector of the (111) plane is colinear with the cuboid diagonal.

We are now left with the situation of a cube being compressed along its diagonal. For the purposes of this explanation we will refer to the cube diagonal with its Miller indices of a generic unit cube to be [1 1 1] direction leaving a growing equilateral triangle in the (1 1 1) plane parallel to the flat punch as our contact area. Using equations for separation of planes with Miller indices, it can be seen that the compressive displacement (D) is proportional to the side length of a cube (a) by:

$$D = d_{hkl} = \frac{a}{\sqrt{h^2 + k^2 + l^2}}. \quad (4.2)$$

Solving for the (1 1 1) compression direction:

$$D = d_{111} = \frac{a}{\sqrt{3}}. \quad (4.3)$$

The side length that we will be using is the average of our unit cell dimensions (a , b , c). An equilateral triangle of side length (s) has an area ($A_{triangle}$):

$$A_{triangle} = \frac{\sqrt{3}}{4} s^2. \quad (4.4)$$

The equilateral triangle we are interested in here is the one that makes a diagonal on the face of a cube, thus having side length of $\sqrt{2}a$. So, solving Equation 4.3 for a , and plugging into Equation 4.4, we obtain:

$$A_{triangle} = \frac{\sqrt{3}}{4}(\sqrt{2}(\sqrt{3}D))^2, \quad (4.5)$$

which is then combined with Equation 4.1 to yield our final expression of:

$$P_{contact} = \frac{2\sqrt{3}}{9} \frac{L}{D^2}. \quad (4.6)$$

We do not define an expression for strain here, as the size of a particular cubic grain being compressed is not always obvious from the SEM images.

Maximum contact pressure

The maximum contact pressure was found by taking a low-pass Butterworth filter of the loading segments and finding the maximum value of that fit function. The same reloading experiments used just the first loading segment, and the higher reloading experiments used all regions of the loading segments that were deemed to have deformation dominated by the response of pristine benzene.

To find the cutoff, loads 2-4 were fit to a fourth-order polynomial function, and the point at which the slope of this function first falls below that of the unloading stiffness is marked as the point in which we deviate from an elastic reloading. When the slope of this fit returns to that of the load 1 value, then our measured response should again be from pristine benzene. The loading stiffness in load 1 is reported as the linear fit of this entire region. The loading stiffness in all subsequent loading regions for same reloading experiments is also taken as the slope of a linear fit, but the stiffness during subsequent loading regions for the higher reloading experiments is taken at the point in which the third derivative of the fourth order fit is zero and the second derivative is at its maximum.

4.3 Calculating yield stress

We ended up choosing a working definition of yield stress based on the first displacement burst as it was the point in which we felt that the crystal was first yielding. These initial displacement bursts were identified manually from load versus displacement plots. The average yield stress for the 14 compressions done by reloading to the same value four times is 1.83 ± 0.94 GPa, and for the 7 compressions done to subsequently higher reloads is 2.64 ± 0.94 GPa. Taken together, it is $2.05 \pm$

Yield stress results				
	Units	First Burst	Quadratic Fit	Peak Detection
Average yield stress	GPa	1.97	1.59	1.81
Standard deviation	GPa	1.04	0.66	1.03
Percent error	%	52.1	41.7	57.2
Tests included	Count	30	29	30

Table 4.2: Summary of results from the three yield stress definitions.

1.00 GPa, it should not matter from which type of compression this was identified, but there is a decently strong grouping based on the type of loading profile used. Attempts to show that the crystal was completely elastic up to this point proved to be too difficult to conduct as this point typically happens for very low loads and displacements.

Two alternative definitions to yield stress were considered. The first of these is done by fitting the filtered contact pressure versus filtered displacement data to a quadratic function, and the other is done by peak identification early in the loading profile.

The plots of contact pressure against depth show a decay in contact pressure with increased depth of compression. We thought that since the contact area of the indenter with the crystal should increase as the square of the displacement of the indenter from the tip of the crystal that the contact pressure should decrease with increased compression depth in a similar manner. To make this fit, data points were taken from between the first burst (some of the points before this were unphysically high and seemed to approach infinity, so we chose to ignore them for the fit) to the end of the first loading segment. This data was then fit to a quadratic function using the numpy polyfit fit function in Python version 2.6, and the intercept at zero depth was taken to be the yield stress (as it should occur when depth is minimal within this framework).

Many times there is an increase in contact pressure with depth for very low depths leading to a peak contact pressure during the initial stages of compression. We also tried to identify the peak contact pressure that is not obviously un-physically high. To do this, we found the median of the fifty points immediately preceding and fifty data points immediately following the absolute maximum contact pressure.

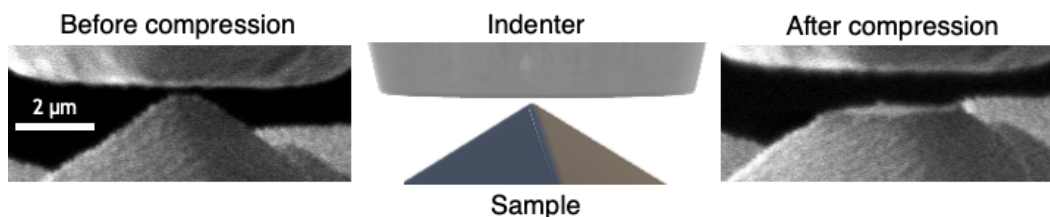


Figure 4.6: SEM micrographs showing before (left) and after (right) images as a result of the flat-punch compression shown schematically (middle).

4.4 Results of compression experiments

Before and after SEM images are shown in Figure 4.6, which indicate that the deformation is limited to the top portion of the sample, with the bottom section not visibly de-forming. We observe only local plastic deformation, so we assume the entire compression to occur over a self-similar area of contact.

Typical examples of the behavior of the load versus displacement data are shown in Figure 4.7. Upon increasing the applied load, the curve is characterized by a mostly linear increase in displacement with multiple stochastic bursts. Once reaching the maximum load, the load was removed at the same loading rate. After a brief rollover period, the curve shows a linear unloading at a higher stiffness.

At this point in the experiment the crystal was re-loaded three more times, either to about the same maximal load or to a progressively higher load 4.7b. In the first case, an individual crystal was repeatedly compressed to the same maximum load of ~ 1 mN, and most of the strain was accumulated during the first loading cycle. Subsequent load cycling results in a virtually identical elastic response, with no hysteresis or further plastic deformation. In the second case, the crystals were compressed to progressively higher loads, up to a maximum load of ~ 1.25 mN. The representative load-displacement response shows that the samples plastically deformed only after re-loading past the previously loaded sample region when the stiffness returns to the value which was observed during the first loading cycle on

pristine benzene.

The contact pressure versus displacement plot in Figure 4.7a shows that the contact pressure quickly increases with small displacements before reaching a maximum and falling off with an approximately quadratic dependence on displacement as the contact area increases, quadratically. The contact pressure appears to approach an asymptote, which we take as the flow stress, or the stress at which if continually applied would continuously deform the material. This would be a limiting factor for the formation of tall geological features in a landscape.

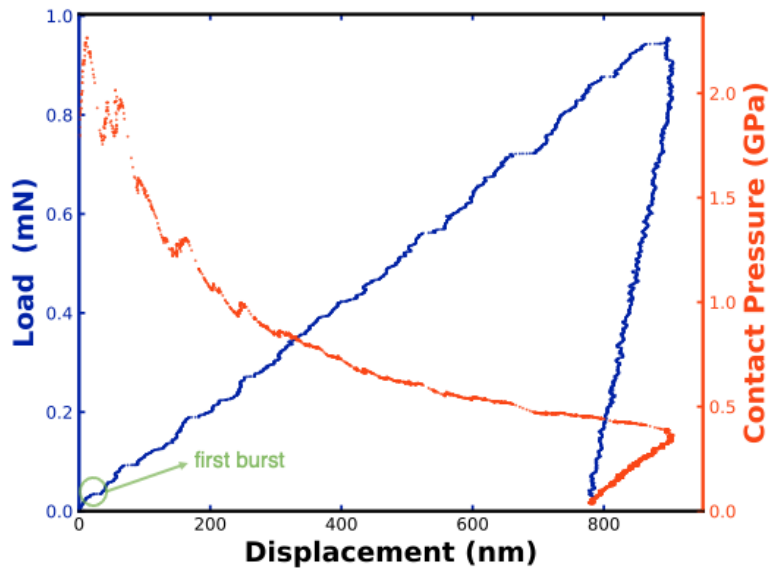
Determining stiffness

Stiffness for the relatively pristine loading regions with bursts included was calculated as the inflection point of a fourth-order polynomial fit for the higher reloads. For the same reloads, the loading other than the first cycle is linear, so the slope is calculated as normal.

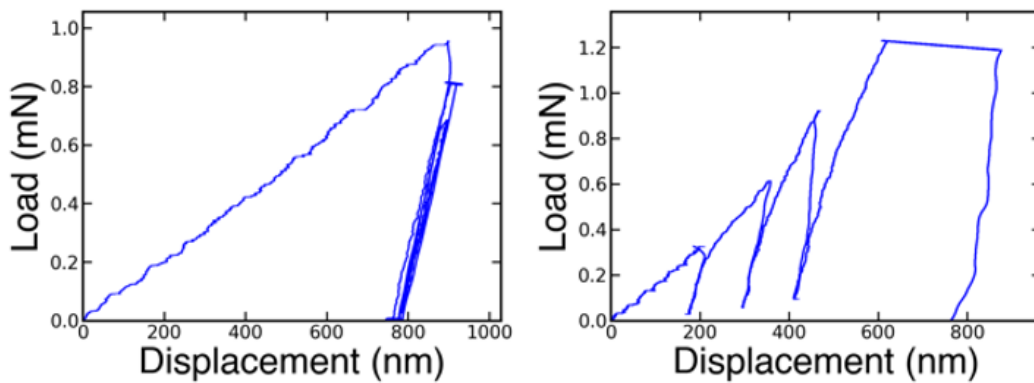
In the experiments, we see that the crystal becomes more compliant throughout a given loading cycle (other than the first cycle). We divide the loading into two segments at the point in which the current loading cycles surpasses the previous maximum compression depth achieved. In all cases, the stiffness of this first segment is greater than that of the second. We attribute this higher stiffness to come from the reloading of the elastically recovered portion of the deformed crystal. Upon passing this dividing point, the mechanism for deformation should return to that which is dominant for plastic compression of unperturbed benzene.

The beginning 20% of the data for the unloading segments is ignored for the linear fit of load versus filtered displacement to determine the stiffness, as there is typically a “roll-over” hysteresis as the indenter switches from applying an increasing to decreasing load. The last 5% of loading segments are also ignored as this is a part of the curve that tends to deviate from the trend of the rest of the loading segments. Figure 4.8 displays the results for the calculated stiffness values. Shown in this figure are violin plots of tests under the higher reloading and same reloading procedures are separated along the x-axis by loading segment, and separated by color into regions of pristine and reloaded benzene. The median values are shown by thick dashed lines, while the first and third quartiles are shown by the thinner dashed lines.

In contrast, the behavior of the stiffness in the simulations is reversed. For the initial loading period, there is a compliant region that suddenly becomes stiffer after a certain point. The transition seems to occur when there is a large scale propagation



(a) Typical plot of load and contact pressure versus displacement with the first displacement burst highlighted in green.



(b) Example plots of data from the same reloads (plotted on the left) and higher reloads (plotted on the right) experiments.

Figure 4.7: Example of typical mechanical signatures observed.

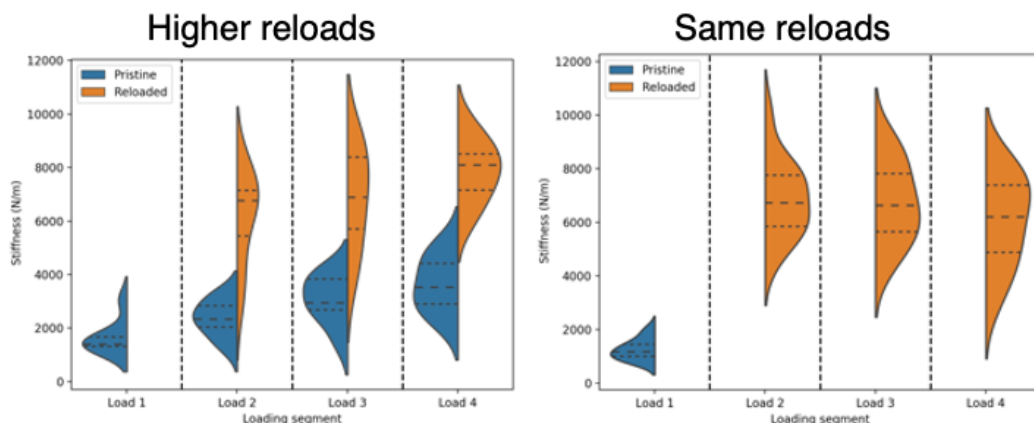


Figure 4.8: Violin plot showing a comparison of stiffness evolution throughout and between loading and unloading segments.

of a phase transition or amorphization region throughout the crystal. This point looked to stay in the same position for both 10 and 20 nm samples. It seems that this is a phenomenon that occurs at a displacement too small for us to observe in the experiments, so we should expect to have agreement between segment 1 stiffness in experiments and segment 2 stiffness in simulations.

We should expect the experiments and simulations to be off by a factor relating to the difference in the size of the sample measured. Experimentally, the crystals have edge lengths on the order of 10 microns, but this would be computationally intractable to reproduce, so the simulations were run on crystals of 10, 20, and 30 nm in height from the cube corner.

Experimentally, we see that unloading stiffness depends on a few factors. For one, if the sample is incrementally loaded to a higher maximal load, then each of the unloading steps shows an increasing unloading stiffness. Though perhaps this is due to the high number of outliers as we approach zero displacement.

Figure 4.8 shows that the distinction between deformation of pristine and deformed benzene is noticeable by the stiffness in the load-displacement response. The entirety of the response of the first loading cycle (load 1) is assumed to represent the response of the pristine benzene as it has yet to be loaded at this point. Comparison of the stiffness of each loading segment is shown in Figure 4.8. For the load 1 segment,

stiffness is found by taking the slope of a linear fit of the load-filtered displacement plot. The bursts are included in this loading slope, so these values should be a slight under-estimate of the actual stiffness of pristine benzene. The load 2-4 slopes are taken in the same manner for samples that are repeatedly loaded to the same load, but there are far fewer bursts during this cycle. Since we are reloading benzene that has already been compressed, much of the interacted volume will be that of a heavily plastically deformed material. Thus, the reloads represent the stiffness of the deformed benzene and not the pristine benzene. The stiffness for loads 2-4 of the experiments that are repeatedly loaded to a higher load undergoes a relatively sharp transition once the majority of the volume of material being deformed is again pristine benzene. The stiffness for these cycles is calculated as the slope of the linear fit of the load-displacement data after this transition occurs. For these segments, we observe a steadily increasing stiffness, suggesting that a larger and larger portion of the material responding to the applied load is deformed, rather than pristine, benzene. All unloading stiffness was calculated as the slope of the load-displacement plot for the unloading segments after the rollover coming from the instrument lag of switching from increasing to decreasing applied load.

Elastic recovery

The elastic recovery is defined here as the displacement change during an unloading cycle from the maximum displacement, usually during the rollover event, to the minimal displacement divided by the displacement change from the minimal displacement of the previous loading segment to the maximal displacement during that same loading segment. The elastic recovery for the first unloading segment is about the same for all methods of testing. This value stays relatively constant for all unloading segments of the higher reloading experiments as each segment is exposed to pristine benzene. The same reloading experiments show a sharp increase to nearly full recovery during unloading segments 2 and 3, with a decrease in recoverability on the fourth cycle.

The first elastic portion during load segment 1 is only present for very small compression depths, so we were unable to measure this stiffness. Compressions that were stopped before the first burst was observed were attempted, but without success.

Throughout the same reloading experiments, there is a decrease in the recoverability and both the loading and unloading stiffnesses, suggesting that there might be some damage accumulation leading to a deterioration in the mechanical properties of

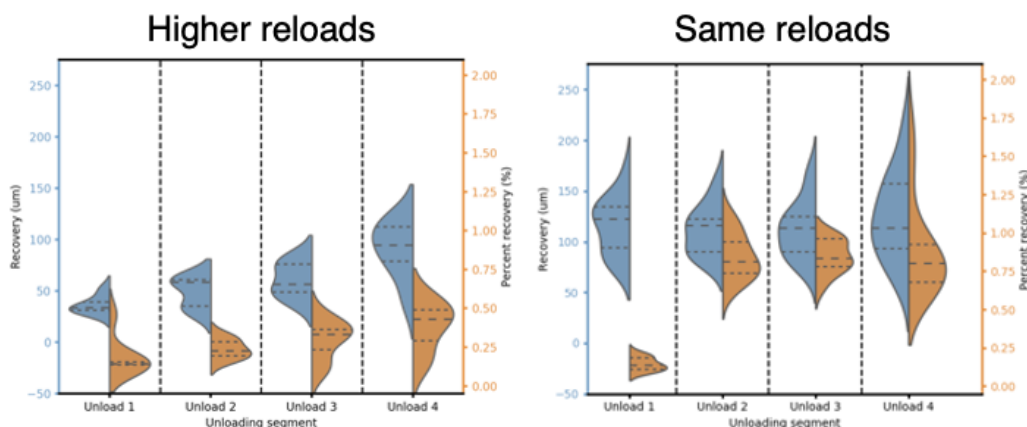


Figure 4.9: Violin plots showing the recovery per segment.

this repeatedly loaded deformed region. The larger drop in the fourth segment could also be accounted for due to the load hold segments. The same is not seen for the higher reloading experiments as the response of each segment incorporates previously pristine benzene, so less damage is accumulated.

Compression of the same reloads method show the same recovery of around 125 μm for each of the unloading segments, while the higher reloads show an increase in the recovery distance. The recovery percentage for the higher reloads gradually increases from about 15% to 40% from unload 1 to unload 4. The recovery percentage for the same reloads is only around 15% for the first cycle, and then jumps to around 80% for the remaining three cycles. This difference in behavior shows that the majority of the plastic deformation is contained to the first loading of the pristine benzene crystal. This is shown in violin plots in Figure 4.9.

Identifying and describing strain bursts

Loading into a previously undeformed region of benzene shows a high number of strain bursts, and identifying these is crucial for differentiating between the behavior of pristine versus compressed benzene. They were identified by three separate methods, each using an independent data channel. The depth maxima filter looks for areas of the data in which the difference in depth between data points is larger than typical, and the burst is defined around these local maxima, while the load and stiffness minima are similarly defined for local minima in each of their data

channels.

The data is first re-zeroed to the point in which contact was initiated, which is determined by manually identifying the first observed spike in load. The data are also passed through a median filter to remove some noise, which can mainly be attributed to vibrations present when using the cryogenic system. Load and displacement are put through a median filter with a moving window of 10 data points, while the stiffness data channel is put through a median filter of 160 data points in the moving window. This channel typically has a higher noise floor. At some points during the experiments due to poorly defined end conditions in the testing method (resolved for some, but not all experiments) the continuous stiffness measurement was not on, and these regions of data resulted in more noisy measurements.

These window sizes were chosen manually with the criteria of visually preserving the strain bursts when plotting the data, while eliminating obvious outliers with the minimal number of data points. Here we also calculate the contact area that we would expect the indenter to be in contact with at a given compression displacement, which we assume to be the area of a (1 1 1) plane within a cube, as previously explained. Contact pressure is calculated by dividing the measured load by this contact area. The normalized strain is calculated by normalizing the displacement channel to its maximum value. During measurement, the timestamps in which the indenter changes loading direction are recorded, and these are used to split the data into different loading and unloading sections.

In attempting to identify the beginning and end of bursts computationally, it became clear that these median filters were insufficient in making the data “well-behaved” enough for identification. Therefore, low-pass Butterworth filters were used to further smooth the data. Low-pass filters are desirable as the signals we are interested in using for these bursts occur at lower frequency than the noise generated by the testing setup. The filters are described by two parameters: the order of the filter, higher order means more aggressive signal dampening, and the critical frequency at which the gain drops to $\frac{1}{\sqrt{2}}$ of the passband.

Data was acquired at 100 Hz for all experiments. The displacement during the loading segments was passed through a third-degree Butterworth filter with a critical frequency of 0.18 Hz. The displacement during unloading segments was passed through a second-degree Butterworth filter with a critical frequency of 0.01 Hz. The load channel for all segments was passed through a fourth-degree Butterworth filter of critical frequency 0.5 Hz. Contact pressure for all segments was passed through a

eighth-degree low-pass Butterworth filter of critical frequency 0.06 Hz. Stiffness for all loading segments was passed through a first-degree low-pass Butterworth filter of critical frequency 0.35 Hz. There are also extreme outliers for the stiffness channels, so data points deviating more than 50 times the median absolute deviation were set to a maximum allowable stiffness at the cutoff value. The median and median absolute deviation are similar to the average and standard deviation typically used in our field, but these data are filled with outliers, so using these similar metrics seems to produce better behavior as they are not as influenced by such outliers.

As the contact area continues to increase the further the indenter is displaced into a crystal of benzene, we should expect the stiffness to increase, so we fit this to a quadratic function (have assumed that the area increases with the square of an increase in displacement). We check to make sure that at least 75% of the data shows an increase in stiffness somewhat close to this behavior, and then subtract this quadratic fit from the filtered stiffness data. Once this subtraction has occurred we linearly fit the data to see if there is still some non-zero change in stiffness throughout this data segment and subtract out a linear fit if we find that to be the case. If however, we find that less than 75% of the data follows this sort of increase, then we just go ahead and immediately take a linear fit of the stiffness data and subtract this away. In either case, what we are left with we will refer to as a “zeroed” stiffness channel. This will make identifying minima and maxima much easier.

It stands to reason that the measurement of a strain burst should coincide with an increase in the displacement per data point, a lessened increase in load per data point, and a locally small stiffness value. So, if we can identify these points, then we have identified the strain bursts by this definition. The increase in displacement per data point is found by taking a pointwise derivative of the displacement data channel and then looking for points falling at least 20 data points apart (such that they are separate burst events) and more than 3 times the median absolute deviation about the median value for a given loading segment. Similarly, the minima in load change per data point were identified as points more than 20 data points separated and at least 3 times the median absolute deviation below the median change in load per data point on a given loading segment. Now that we have found this “zeroed” stiffness channel, we can use it to identify points of minimal change in stiffness per data point in the same manner: more than 20 data points separated and at least 0.75 times the median absolute deviation below the median change in stiffness per data point for the given loading segment. This task would have been much harder

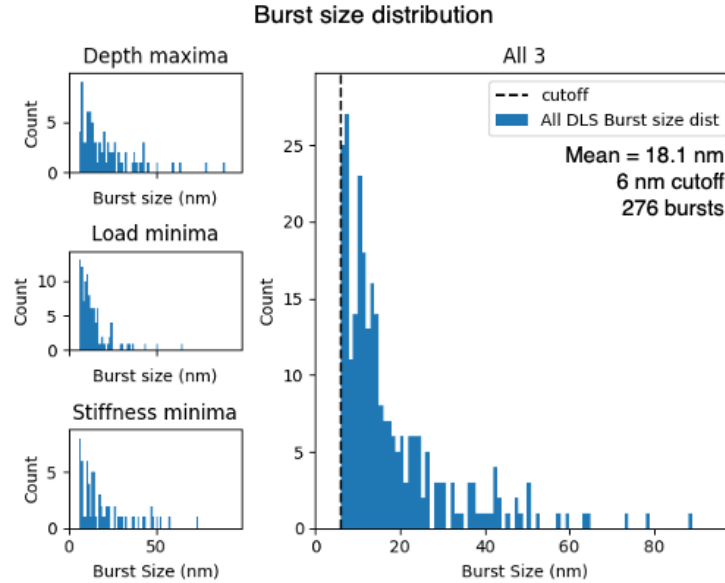


Figure 4.10: Histogram showing distribution of burst sizes.

without a linearly dependence of stiffness on data point number.

At this point, potential places in the data showing a strain burst are identified, but further measures need to be taken to ensure these are neither false positives nor double-counting, and to identify the size of the burst event. We have constrained the bursts to have occurred completely within 0.1 mN of the load corresponding to the identified critical point. These three data channels are used as three separate identifiers of strain bursts, as I cannot think of an unbiased way to combine these and determine which should have priority for determining beginning and end points of these bursts, much less which of the three methods identifies more false negatives or positives.

The distribution in size of the bursts identified is shown in Figure 4.10. Plotted in Figure 4.11 are the stiffness values calculated between all bursts found. The plotted point represents the average displacement between the found bursts during a given loading segment and its associated stiffness, and the horizontal line represents the whole displacement between these bursts.

The small insets on the left of Figure 4.10 show bursts found from the depth maxima method, the load minima, and the stiffness minima method separately. The large histogram is the combination of the three, which gives us a total of 273 bursts found throughout all experiments. The vertical dashed line at 6 nm represents the minimum burst size cutoff.

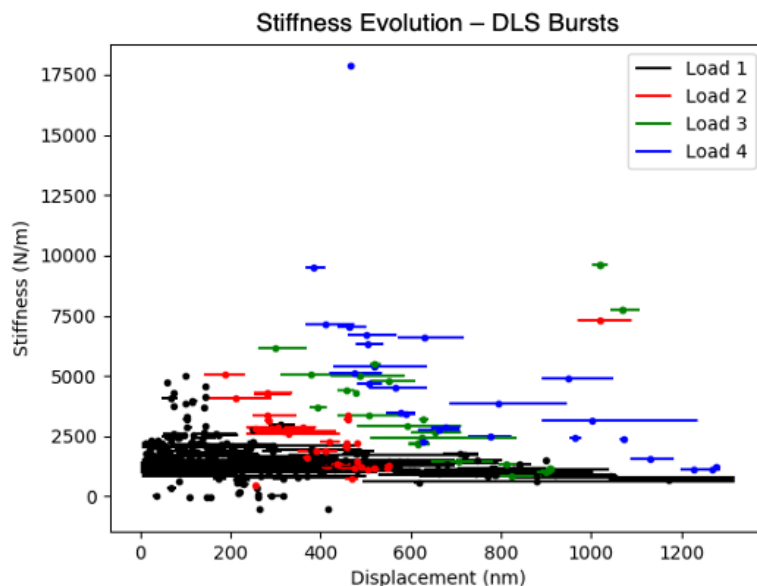


Figure 4.11: Scatterplot showing the evolution of stiffness of unburst benzene.

4.5 Deformation mechanism

The load-displacement behavior suggests a deformation mechanism similar to that of an open porous structure. We believe that the largely open structure of the benzene crystals allows for the proposed deformation mechanism of densification to dominate the observed mechanical response, especially at relatively small strains. Ashby described such a deformation as a series of an initial elastic compression followed by a plastic collapse of a cell structure, which produces a densified top layer that then transfers the load from the indenter tip to the next cell structure and the process is repeated [4].

If the crystals deform as openly porous structures, then we should expect the stiffness for the elastic part of the loading to match that of the unloading segments, and the plastic part of the loading to have a stiffness independent of the loading segment, which is shown in Figure 4.8.

4.6 Molecular Dynamic (MD) simulations¹

Benzene was modeled as a unit cell in the orthorhombic phase *Pbca* with lattice parameters of 7.644 Å, 9.514 Å, and 6.720 Å using an adaptive intermolecular reactive empirical bond order force field [5]. The compression experiments were simulated with a strain rate of $5 \times 10^8 \text{ s}^{-1}$, and the contact area was determined by

¹The MD simulations were designed and performed by my collaborator Lei Zhong, a former student working under Prof. Huajian Gao at Brown University.

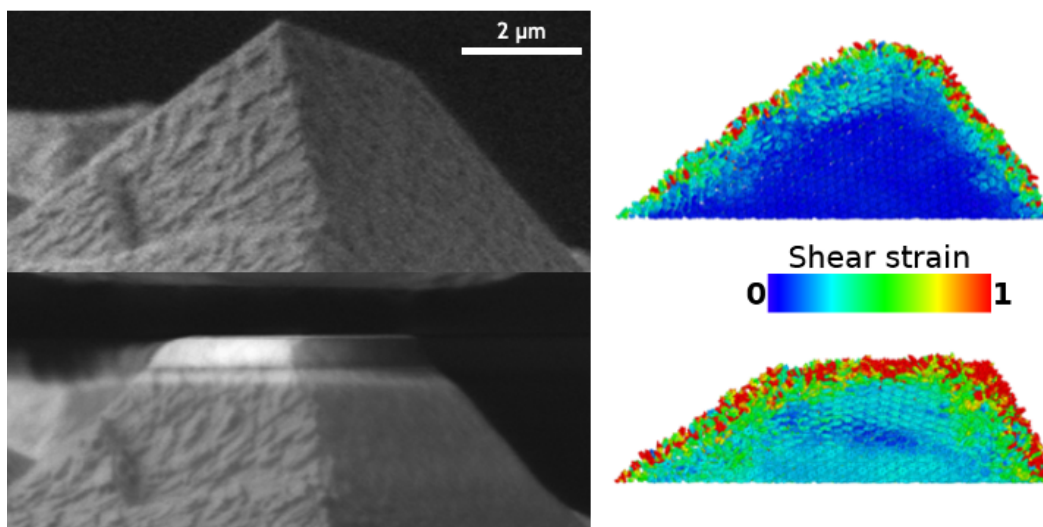


Figure 4.12: Comparison between experimental and MD simulated compressions of benzene crystals before and after compression.

making a surface mesh from the full atomic models with the Ovito software package.

Yield stress was defined as the maximum contact pressure, and flow stress was defined as the average contact pressure between the onset of large-scale propagation of phase transition and 40% strain. Yield stress was defined as such because this appears to be the first point in which the simulated crystals showed any plastic deformation. Shear strain was found by calculating the local transformation matrix between the current and reference atomic configurations [6].

Figure 4.12 shows that there is good qualitative agreement between the experiments and simulations. The shape of the crystal after agrees quite well between experiments and simulations. The mechanical signatures varied between these two methodologies, but the densified top layer appears to be consistent between the two. Atoms of an amorphous phase are present in this layer in the simulations, and we observe a change in secondary electron contrast in this layer in the SEM.

Computed compressions of a nanometer-sized orthorhombic benzene single crystal reveal that the deformation is confined near the indenter tip up until a point in which there is a large-scale propagation of a phase transition or amorphization region throughout much of the crystal. The simulations were done to measure the impact of temperature, crystal size, and compression direction on the mechanical properties of single-crystalline benzene.

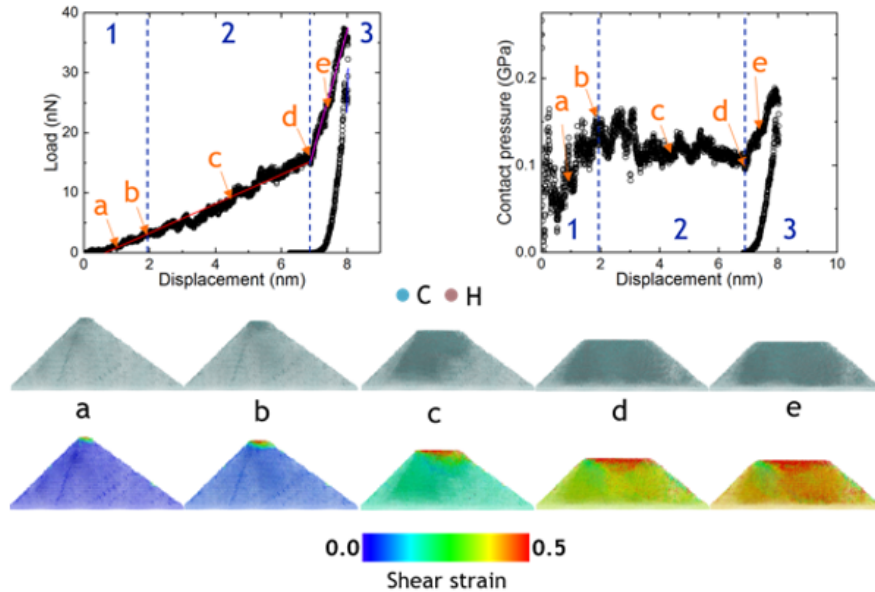


Figure 4.13: Relationships between stress and stiffness with loading direction colored by temperature and particle size represented by data point size.

A typical simulation is shown in Figure 4.13. From these plots we can see that three different regimes have emerged for this compression of a 20 nm crystal at 10 K along the $[0\ 1\ 0]$ direction.

The deformation during compression may be broken up into phases based on the behavior of the contact pressure versus displacement plots. For the $[0\ 1\ 0]$ and $[0\ 1\ 1]$ loading directions, there is initially a directional relationship as the contact region is becoming amorphous and small deformation is observed throughout the rest of the crystal. After yielding occurs, there is a slightly inverse relationship between contact pressure and displacement as there is a large-scale phase propagation throughout the crystal. Especially evident in the simulations of larger crystals loaded in the $[0\ 1\ 0]$ direction, and possibly also for the smaller crystals, is the appearance of a third region in which the contact pressure increases with increased strain and the loading stiffness becomes much higher.

During the loading process, the shear strain of atoms in the amorphization and phase transition regions remain relatively constant, which suggests that they are no longer load bearing, and serve only to transfer the applied load further down into the crystal. The regions of the crystal below this layer are characterized by small deformations having shear strain that varies from 0 to 0.5, suggesting that this part of the crystal is actually load bearing.

We do not see a strong dependence of mechanical properties over the range of temperatures studied. Yield stress decreases with increased crystal size, while unloading stiffness increases with increased crystal size. There is only slight dependence on deformation direction, which suggests low anisotropy and lends itself to be a fair comparison to the experiments of compressions in unknown crystal directions. The results from the MD simulations are summarized in Figure 4.14.

No significant bulging of the cuboids was observed during any of the tests, so it was assumed that all of the densifying was done in the same direction as the uniaxial compressive load. However, the simulations showed that the crystal's volume remained approximately constant, but the amount of material that would go in to bulging would be so low that it would be very difficult to observe in the SEM.

The relatively constant stiffness throughout the loading suggests that the deformation mechanism is largely localized, so it is always acting on relatively pristine benzene, thus the behavior remains constant throughout the whole test. The only difference is that there is a continually growing "crust" of densified, non-load bearing, material directly underneath the indenter that artificially increases the contact area by an amount that is difficult to quantify.

Loading and unloading stiffness from the simulations are about three orders of magnitude lower than experiments, which, given that the size of the samples measured were almost around three orders of magnitude smaller, is expected. The simulation stress values are one order of magnitude lower than experiments, which is harder to reconcile. One might consider this difference to be attributed to the larger proportion of amorphous to crystalline regions of the entire sample given that the simulated samples are much smaller. However, the simulated yield stress decreases as sample size increases from 10 to 30 nm height of the crystal. It is possible that the combination of the bulging and slight increase of contact area from the densified top layer lead to an overestimation of contact pressure in the experimental results.

4.7 Extrapolating to other temperatures

Other works have presented results from experiments of other proxy materials at much higher temperature, and then done an extrapolation to show the expected properties at other temperatures [7]. The same methodology was adopted here since the SEMentor is only able to get down to ~ 125 K without the usage of liquid helium. Only a small correction is expected as the temperature difference is not high, and there are no known phase transitions around these temperatures. Elastic modulus

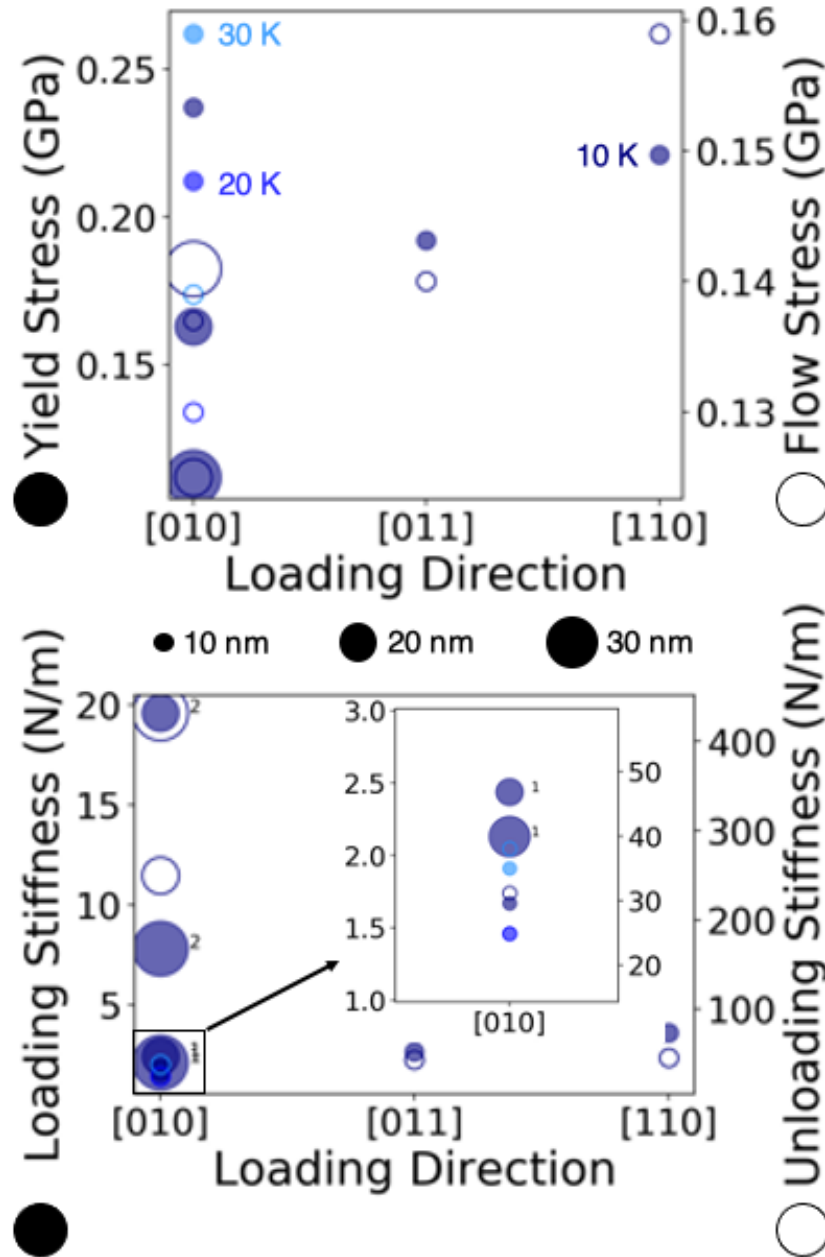


Figure 4.14: Relationships between stress and stiffness with loading direction colored by temperature and particle size represented by data point size.

(E) as a function of temperature (T), the elastic modulus at 0 K (E_0), and the melting temperature (T_m) of a material is given as:

$$E(T) \approx E_0 \left(1 - 0.5 \frac{T}{T_m}\right). \quad (4.7)$$

The work of Yu *et al.* was based on nanoindentation and used a relationship between their measured hardness and the elastic modulus at 0 K to get to modulus as a function of temperature [7]. Given that our experiments give a stiffness, but not modulus, we instead use a relational expression to give a temperature correction to the reported stiffness values.

Solving for E_0 allows for the comparison of values of modulus found at different temperatures (h and l) as shown in Equation 4.9.

$$\frac{E_h}{\left(1 - 0.5 \frac{T_h}{T_m}\right)} = \frac{E_l}{\left(1 - 0.5 \frac{T_l}{T_m}\right)} \quad (4.8)$$

The melting temperature of benzene is ~ 5.5 °C, and the temperature during testing is recorded. The results shown were performed at an average temperature of 123 K, which should, by this relationship, be an underestimate of the properties at 94 K by about 7%.

$$E_{94K} \approx 1.07 E_{123K} \quad (4.9)$$

Since modulus is proportional to stiffness, and we do not know the geometry of the samples here well enough to confidently determine modulus, we can use this same relational factor with the stiffness determined by the experiments done on benzene.

4.8 Theoretical mountain height

With the acquisition of improved satellite images coming from Titan, the mapping of geological features on the surface should be determined more accurately, which allows for the use of known geological relationships to further narrow down the possibility of materials accounting for the majority of the surface.

$$h_{max} \approx \frac{\sigma_c}{\rho g} \quad (4.10)$$

Taking the flow contact pressure of around 150 MPa to be the critical stress, the density of benzene to be ~ 1.012 gcm⁻³, and the gravitational constant of Titan to be about 1.352 ms⁻² ($\sim 14\%$ of the value on Earth) yields an answer of around 100 km. Given that the highest features observed on the surface are around 500 m, we can see that there are probably some other features of the surface more strongly influencing the local geography.

4.9 Transmission Electron Microscopy (TEM)

The benzene crystals used for TEM were grown in a different method than those used for the compressions, but we believe these two methods to yield similar quenching rates and therefore assume crystals made from either method to have the same crystal structure. From previous works investigating benzene in diamond-anvil pressure cells monitored by X-ray and RAMAN spectroscopy by Thiéry and Léger [8], and Ciabini [9], it does not appear that there are other phases available for benzene to transform into at our operating conditions. Even if we were to locally produce sufficient pressure for another phase to be thermodynamically favorable, it is stated that the phase transitions of solid benzene are slow, so the timescale of these transitions at our operating conditions would surely be larger than the timescale of compression.

The samples used for transmission electron microscopy (TEM) were prepared with a FEI Vitrobot Mark IV. The sample was made by blotting 3 μL of liquid benzene on a lacey carbon TEM grid with only one blotting pad using a blot force setting of -15 at 10°C for 0.5 s, and then plunging into liquid nitrogen. The sample was kept under liquid nitrogen during transfer to the TEM for imaging at 77 K. TEM micrographs and diffraction were obtained using a Talos Arctica (ThermoFischer Scientific, formerly FEI) with a FEG operating at 200 kV equipped with the 4k x 4k FEI Falcon II direct electron detector. A 10 μm selected-area diffraction (SAD) aperture was used to isolate information from one crystal during acquisition of the diffraction pattern.

Figure 4.15 created in Vesta with lattice parameters from the neutron diffraction study by G. E. Bacon *et al.* [10] shows the structure of a benzene crystal.

Benzene proved to have poor beam stability, but we were able to navigate the Kikuchi lines to find a zone axis and obtain a diffraction pattern from this orientation. Shown in Figure 4.16 is a TEM micrograph at a relatively low magnification showing the morphology of the benzene crystals that formed on the lacey carbon grid. Figure 4.16 shows a higher magnification TEM micrograph of the crystal we found oriented close to a zone axis, and we can see from this image that there do not seem to be many obvious large defects in this crystal.

The diffraction pattern shown in Figure 4.16 was acquired from the outlined section of the crystal shown in the upper-right panel of the figure. This pattern indicates that the sample is single crystalline, and we assumed it to be a benzene crystal in the orthorhombic $Pbca$ phase with offset benzene rings occupying the face-centers and

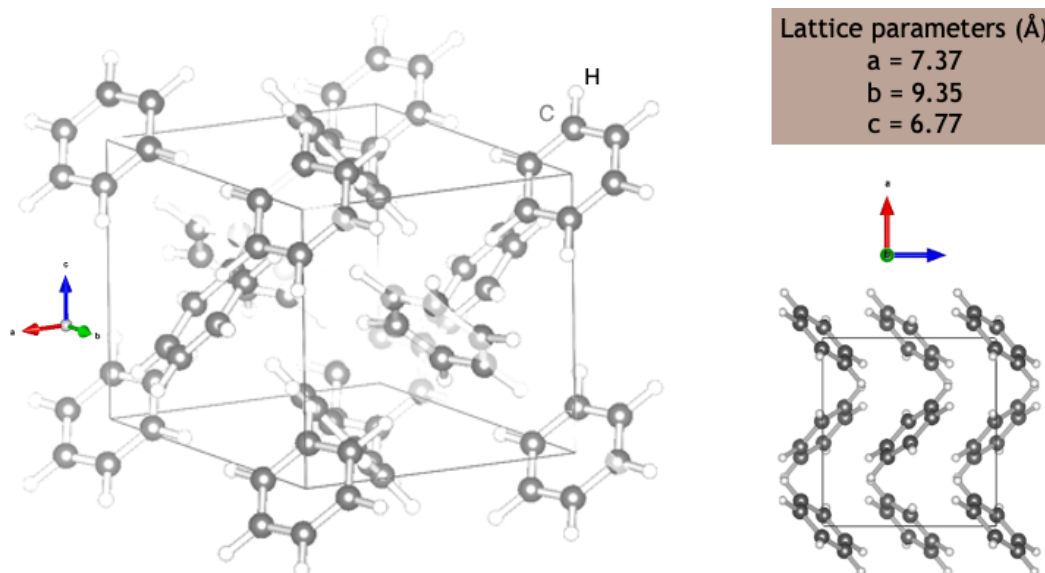


Figure 4.15: Visualization of the structure of benzene created with Vesta.

vertices of the unit cell identified by Cox *et al.* [11]. With the lattice parameters of 7.384 Å, 9.416 Å, and 6.757 Å, as reported by Craven *et al.* [3] using rotating neutron powder diffraction for deuterated benzene at 105 K, we indexed the labelled points to be 100, 021, and 121 as they are a 99.1%, 97.6%, and 97.6% match, respectively, to the values reported by Craven, which are consistent with other values reported around this temperature in literature. Knowing these points on the diffraction pattern, we may identify the zone axis we found to be the $[01\bar{2}]$. Higher magnification TEM micrographs proved difficult to achieve due the poor beam stability of benzene, so more detailed observation of atomic defects was not feasible.

4.10 Conclusions

Presented are in-situ experiments and molecular dynamic simulations on the compression of an orthorhombic single crystal of benzene at cryogenic temperatures. Compressions on a corner of benzene single crystals identify the maximum stress to be around 1.1 GPa, while the simulations put the yield stress closer to around 0.2 GPa. The experiments suggest a highly localized densification type of deformation, and the simulations identify three separate deformation regions. The first is amorphization near the surface, followed by intermolecular slip below that “crust,” and then small deformations bearing the load throughout the rest of the crystal. Solid organic materials are increasingly recognized as important to the geology and evo-

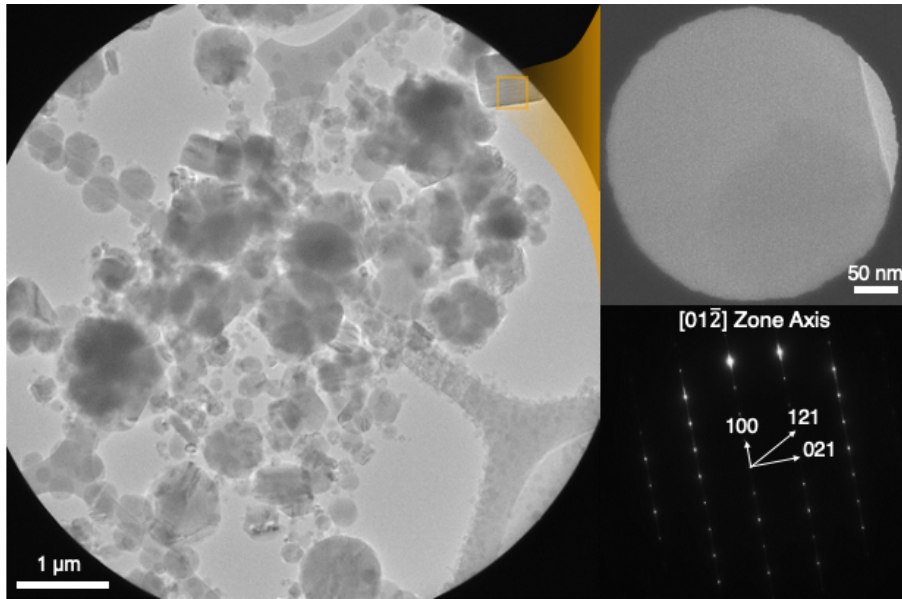


Figure 4.16: TEM micrographs and a diffraction pattern showing the structure of benzene crystals.

lution of icy worlds in the outer Solar System, especially Titan. Yet, there are few published measurements of the mechanical properties of solid organics at cryogenic temperatures. These physical parameters can be used to make specific predictions of geological processes that could occur on Titan's surface and subsurface, and estimates of the extent and surface expression of these processes. As well, the design of solid sampling systems for in-situ missions requires information about material strength, deformability, resistance to fracture, and stiffness. This work shows how mechanical characterization methods used on materials at non-Earthlike conditions can expand our understanding of the processes and evolution of other worlds.

BIBLIOGRAPHY

- [1] S. W. Lee, L. Meza, and J. R. Greer, “Cryogenic nanoindentation size effect in [001]-oriented face-centered cubic and body-centered cubic single crystals,” *Applied Physics Letters*, vol. 103, no. 10, pp. 1–6, 2013, ISSN: 00036951. DOI: 10.1063/1.4820585.
- [2] J. Wang, J. Lian, J. R. Greer, W. D. Nix, and K.-S. Kim, “Size effect in contact compression of nano- and microscale pyramid structures,” *Acta Materialia*, vol. 54, no. 15, pp. 3973–3982, 2006. DOI: 10.1016/j.actamat.2006.04.030. [Online]. Available: https://ac.els-cdn.com/S135964540600317X/1-s2.0-S135964540600317X-main.pdf?_tid=2b89d740-0c47-11e8-8848-00000aab0f01&acdnat=1518036225_4256c024e92e950b9af9397a6cd9639a.
- [3] C. J. Craven, P. D. Hatton, C. J. Howard, and G. S. Pawley, “The structure and dynamics of solid benzene. I. A neutron powder diffraction study of deuterated benzene from 4 K to the melting point,” *Citation: The Journal of Chemical Physics*, vol. 98, pp. 8236–8243, 1993. DOI: 10.1063/1.464528. [Online]. Available: <https://aip.scitation.org/doi/pdf/10.1063/1.464528>.
- [4] M. F. Ashby, “The mechanical properties of cellular solids,” *Metallurgical Transactions A*, vol. 14, no. 9, pp. 1755–1769, 1983, ISSN: 0360-2133, 1543-1940. DOI: 10.1007/BF02645546. [Online]. Available: <http://link.springer.com/article/10.1007/BF02645546>.
- [5] S. J. Stuart, A. B. Tutein, J. A. Harrison, and I. Introduction, “A reactive potential for hydrocarbons with intermolecular interactions,” *Journal of Chemical Physics*, vol. 112, no. 14, pp. 6472–6486, 2000, ISSN: 0021-8979. DOI: 10.1063/1.3488620.
- [6] F. Shimizu, S. Ogata, and J. Li, “Theory of Shear Banding in Metallic Glasses and Molecular Dynamics Calculations,” *Materials Transactions*, vol. 48, no. 11, pp. 2923–2927, 2007, ISSN: 1345-9678. DOI: 10.2320/matertrans.MJ200769. [Online]. Available: https://www.jstage.jst.go.jp/article/matertrans/48/11/48_MJ200769/_article.
- [7] X. Yu, S. M. Hörst, C. He, P. McGuiggan, and B. Crawford, “Where does Titan Sand Come From: Insight from Mechanical Properties of Titan Sand Candidates,” *Journal of Geophysical Research: Planets*, 2018. [Online]. Available: <https://arxiv.org/pdf/1806.08056.pdf>.
- [8] M. M. Thiéry and J. M. Léger, “High pressure solid phases of benzene. I. Raman and x-ray studies of C₆H₆ at 294 K up to 25 GPa,” *The Journal of Chemical Physics*, vol. 89, no. 7, pp. 4255–4271, 1988, ISSN: 00219606. DOI: 10.1063/1.454809.

-
- [9] L. Ciabini, M. Santoro, F. A. Gorelli, R. Bini, V. Schettino, and S. Rauegi, “Triggering dynamics of the high-pressure benzene amorphization,” *Nature Materials*, vol. 6, no. 1, pp. 39–43, 2007, ISSN: 14764660. DOI: 10.1038/nmat1803.
- [10] G. E. Bacon, N. A. Curry, and S. A. Wilson, “A crystallographic study of solid benzene by neutron diffraction,” *Proceedings of the Royal Society of London. Series A. Mathematical and Physical Sciences*, vol. 279, no. 1376, pp. 98–110, 1964, ISSN: 0080-4630. DOI: 10.1098/rspa.1964.0092.
- [11] E. Cox, F. R. S, D. W. J. Cruickshank, and J. A. S. Smith, “The crystal structure of benzene at -3 C,” vol. 247, 1958.

Part III

Concluding Remarks

SUMMARY AND OUTLOOK

5.1 Standardize fracture testing for lattices

There is much work left to be done as lattices are becoming more prevalent materials of choice as engineering design continues to require more sophisticated combinations of desirable material properties. I imagine that in a few years, the experimental side of this field will look much like the present small-scale fracture community. A multitude of new methodologies will arise based on equipment availability in each of the groups attempting to capture the same properties. Comparison between these techniques will be difficult, but necessary in order to properly understand the parameter space obtainable via architected hierarchy within a material. Identifying a technique that is technically sound and easy to replicate will be necessary for these materials to ever be used in structural applications at industrial scales. Essentially, I think that the field should put together some sort of ASTM standard to explore these behaviors.

Alternative testing geometries

There are also alternative geometries such as the compact tension shear specimen that would allow for the probing of K_i and K_{ii} as well as the loading of these architectures in more directions more simply from an experimental standpoint than having to redraw the entire structure each time a different loading orientation was desired [1].

This would be interesting, and feasible with our current laboratory techniques, as it would allow us to experimentally determine the point at which the loading angle would be able to overcome the anisotropy of a given lattice geometry. This loading frame would be simple to make for macro-lattices to be tested on an Instron, and should be printable directly on to Nanoscribe scale samples. This and other one-piece printable testing geometries would benefit from the use of variable mechanical properties (i.e. making the frame stiffer than the sample by both material parameters and geometry), which is achievable with custom resin design.

One low-hanging fruit is the impact properties of the lattices at a moderate loading rate. The samples prepared for the macrolattice portion of this dissertation are suffi-

ciently large for Charpy impact testing. This would be interesting both for studying the impact properties at these loading rates, but also to get another comparison for the behavior of lattices tested under the correct geometries of a ASTM standard testing method.

5.2 Grayscale polymers for rapid prototyping of composites

Additive manufacturing techniques are widely used for prototyping parts, and I think utilizing grayscale polymers would allow for this prototyping to move over into the composite space. It would also be very helpful for making the gripping portion of any future alternative testing geometries stiffer than the sample to be tested so that these two pieces might be printed together. These resins would also allow for the another variable by which the local mechanical properties of a portion of a lattice could be tunable without having to introduce any geometric stress concentrators by having variable node geometries or the like.

5.3 Cryogenic properties of IPDIP

IPDIP films were written and tried in the cryogenic system only once. There were more charging issues than I had dealt with previously, but looking back at the images, I have since discovered a way to image at lower acceleration voltage, so this might be worth revisiting in the future. Other works of the group have shown that the glass transition temperature of IPDIP is something above 90°C, so a drastic change in properties such as a ductile-to-brittle transition should not be expected, but it would be worth investigating to see if it would be enough stiffening to alleviate some of the problems noted in figuring out testing methodologies in Part I.

In general, the cryogenic setup is highly underutilized in the group and could lead to very interesting studies once the printing of metallic resins is more robust. Studying fracture properties through the ductile-to-brittle-transition temperature with homogeneous samples at these length scales would be interesting. Combining this capability with the ability to print a composite with some sort of grayscale polymer technique would allow for many tuneable parameters at various points within a lattice, and the temperature aspect of things could make for some very interesting lightweight sensing applications.

5.4 Mechanical properties of small molecule organics

Although computational numbers exist for basic mechanical properties of some of these materials, it will be necessary to experimentally validate these values before

hoping to interact with these materials on any sort of flyer mission to places in which their ambient conditions produce these materials.

BIBLIOGRAPHY

- [1] H. A. Richard and K. Benitz, "A loading device for the creation of mixed mode in fracture mechanics," *International Journal of Fracture*, vol. 22, no. 2, pp. 55–58, 1983, ISSN: 03769429. DOI: 10.1007/BF00942726.